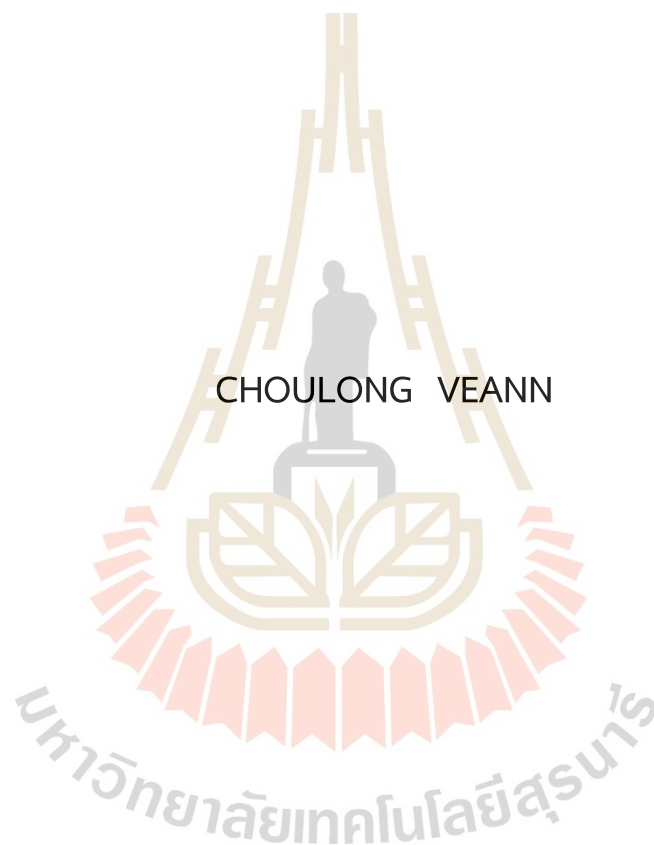


STRUCTURE AND ELECTROCHEMICAL PROPERTIES OF
AgFeO₂-BASED NANOPARTICLES PREPARED BY CO-PRECIPIATION
METHOD



A Thesis Submitted in Partial Fulfillment of the Requirements for the

Degree of Master of Science in Physics

Suranaree University of Technology

Academic Year 2023

โครงสร้าง และสมบัติทางเคมีไฟฟ้าของอนุภาคนาโนกลุ่มซิลเวอร์เฟอร์ไรต์
เตรียมโดยวิธีการตกตะกอนร่วม



วิทยานิพนธ์นี้เป็นส่วนหนึ่งของการศึกษาตามหลักสูตรปริญญาวิทยาศาสตรมหาบัณฑิต

สาขาวิชาฟิสิกส์

มหาวิทยาลัยเทคโนโลยีสุรนารี

ปีการศึกษา 2566

STRUCTURE AND ELECTROCHEMICAL PROPERTIES OF AgFeO₂-BASED
NANOPARTICLES PREPARED BY CO-PRECIPITATION METHOD

Suranaree University of Technology has approved this thesis submitted in partial fulfillment of the requirements for a Master's Degree.

Thesis Examining Committee



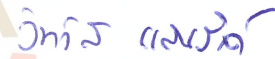
(Assoc. Prof. Dr. Worawat Meevasna)

Chairperson



(Prof. Dr. Santi Maensiri)

Member (Thesis Advisor)



(Asst. Prof. Dr. Wittawat Saengrang)

Member



(Dr. Narong Chanlek)

Member



(Assoc. Prof. Dr. Yupaporn Raksakunpiwat)

Vice Rector for Academic Affairs

and Quality Assurance



(Prof. Dr. Santi Maensiri)

Dean of Institute of Science

จุล่ง เวียน : โครงสร้าง และสมบัติทางเคมีไฟฟ้าของอนุภาคนาโนกลุ่มซิลเวอร์เฟอร์ไรต์
เตรียมโดยวิธีการตกตะกอนร่วม (STRUCTURE AND ELECTROCHEMICAL PROPERTIES
OF AgFeO₂-BASED NANOPARTICLES PREPARED BY CO-PRECIPIATION METHOD)
อาจารย์ที่ปรึกษา : ศาสตราจารย์ ดร.สันติ แม่นศิริ, 142 หน้า.

คำสำคัญ : สมบัติทางเคมีไฟฟ้า/อนุภาคนาโนกลุ่มซิลเวอร์เฟอร์ไรต์/วิธีการตกตะกอนร่วม/เทคนิค
การดูดกลืนรังสีเอ็กซ์/เทคนิคการดูดซับแก๊ส

ในงานวิจัยนี้ได้ทำการเตรียมอนุภาคนาโนกลุ่มซิลเวอร์เฟอร์ไรต์ AgFeO₂ และ AgFe_{1-x}M_xO₂ (M = Co และ Ni) ที่ x = 0.00 0.05 0.10 0.15 และ 0.20 โดยใช้วิธีการตกตะกอนร่วมเทคนิคการ
เลี้ยวเบนของรังสีเอกซ์ (XRD) เทคนิคกล้องจุลทรรศน์อิเล็กตรอนแบบส่องกราด (SEM) และเทคนิค
กล้องจุลทรรศน์แบบส่องผ่าน (TEM) ถูกนำไปใช้ศึกษาโครงสร้างผลึก และลักษณะสัณฐานวิทยาของ
อนุภาคนาโนกลุ่มซิลเวอร์เฟอร์ไรต์ ที่เตรียมได้ สถานะทางประจุและองค์ประกอบทางเคมีของสาร
ตัวอย่างถูกวัดโดยเทคนิคการดูดกลืนรังสีเอ็กซ์ (XANES) และเทคนิคสเปกโทรสโกปีโฟโตอิเล็กตรอน
ด้วยรังสีเอกซ์ (XPS) เทคนิคการดูดซับแก๊สถูกนำไปตรวจสอบพื้นผิวจำเพาะ การแจกแจงทาง
ปริมาตรของรูพรุน และการแจกแจงทางขนาดของรูพรุนโดยวิธีการ BET และ BJH ผลของอุณหภูมิ
ต่าง ๆ ในการเผา และปริมาณของการแทนที่ของ Co และ Ni ไอออนในโครงสร้างนาโนซิลเวอร์เฟอร์
ไรต์ต่อสมบัติทางเคมีไฟฟ้าถูกทำการศึกษา นอกจากนี้เทคนิค CV เทคนิคการชาร์จและดิสชาร์จแบบ
ใช้กระแสคงที่ (Galvanostatic charge-discharge) และเทคนิคสเปกโทรสโกปีอิมแพดแดนซ์อิเล็กโทร
เคมีคัล (EIS) ถูกนำไปใช้ในการทดสอบสมบัติทางเคมีไฟฟ้าของสารตัวอย่างด้วยการทดลองโดยใช้
ระบบสามขั้วและสารละลาย KOH ความเข้มข้น 3M เป็นตัวอิเล็กโทรไลต์

จากผลของ XRD และ TEM พบว่าสารตัวอย่างที่เตรียมได้ทั้งหมดมีโครงสร้างผลึกแบบผสม
ระหว่าง rhombohedral 3R-AgFeO₂ และ hexagonal polytype 2H-AgFeO₂ สำหรับการศึกษา
โครงสร้างนาโน AgFeO₂ ที่เจือด้วย Co และ Ni ไม่มีการบ่งชี้ถึงเฟสเจือปน เช่น NiO, CoO, Fe₂O₃
หรือสปีเนล CoFe₂O₄ เฟสสารเจือปนเหล่านี้โดยทั่วไปก่อตัวภายใต้สภาวะที่คล้ายคลึงกับการ
สังเคราะห์ AgFeO₂ การไม่มีเฟสที่เกี่ยวข้องกับ Co และ Ni แสดงให้เห็นว่าไอ Co ไอออนและ Ni
ไอออนอาจแทนที่ Fe ไอออนภายในโครงสร้างผลึกเตลาฟอสไซด์ AgFeO₂ ได้ และจากผลของ SEM
แสดงให้เห็นว่าโครงสร้างนาโนกลุ่มซิลเวอร์เฟอร์ไรต์มีขนาดอนุภาคอยู่ระหว่าง 12 ถึง 102 นาโน
เมตร จากการวิเคราะห์ด้วยเทคนิค XAS และ XPS บ่งบอกสถานะออกซิเดชันในโครงสร้างนาโนกลุ่ม

CHOU LONG VEANN : STRUCTURE AND ELECTROCHEMICAL PROPERTIES OF
AgFeO₂-BASED NANOPARTICLES PREPARED BY CO-PRECIPITATION METHOD.
THESIS ADVISOR : PROF. SANTI MAENSIRI, D.Phil. 142 PP.

Keywords : ELECTROCHEMICAL PROPERTIES/AgFeO₂-BASED NANOPARTICLES/CO-
PRECIPITATION METHOD/X-RAY ABSORPTION SPECTROSCOPY/GAS ADSORPTION
TECHNIQUE

In this research, co-precipitation method was used to prepare pure AgFeO₂ and AgFe_{1-x}M_xO₂ (M = Co and Ni) nanoparticles where x = 0.00, 0.05, 0.10, 0.15, and 0.20. To investigate the crystal structure and morphology of the produced AgFe_{1-x}M_xO₂ nanoparticle, the techniques of X-ray diffraction (XRD), scanning electron microscopy (SEM) and transmission electron microscopy (TEM) were employed. By utilizing X-ray absorption spectroscopy and X-ray photoelectron spectroscopy (XAS and XPS) techniques, the valence state and elemental composition were calculated. Through the BJH and BET methods, the technique of gas adsorption was utilized to examine pore volume, pore size distribution and specific surface area of the obtained samples. The impact of varying calcination temperatures and the substitution of Co and Ni ions in AgFeO₂ nanostructures was examined to assess their influence on the electrochemical performance of AgFeO₂ nanostructures. For all the samples, the electrochemical performance was conducted on a three-electrode system through CV, EIS and GCD methods in a 3M electrolyte.

The results of XRD and TEM show that all the prepared AgFe_{1-x}M_xO₂ nanoparticles contained the mixing phases of the rhombohedral 3R-AgFeO₂ and hexagonal polytype 2H-AgFeO₂. For the study of Co and Ni-doped AgFeO₂ nanostructures, there are no indications of impurity phases like metallic nickel, NiO, metallic cobalt, CoO, Fe₂O₃, or CoFe₂O₄ spinel. These impurity phases typically form under condition similar to the synthesis of AgFeO₂. The absence of cobalt and nickel-related phases suggests that cobalt and nickel ions might substitute iron ions within

the delafossite structure. Moreover, the particle size of $\text{AgFe}_{1-x}\text{M}_x\text{O}_2$ ranges from 12 nm to 102 nm which is confirmed by SEM results. The XANES and XPS analyses present the oxidation states in all the AgFeO_2 -based nanostructures, consisting of a Ag/Ag^+ mixing oxidation state and Fe^{3+} . In addition, in the Co and Ni-doped AgFeO_2 nanostructures, we observed the presence of Co^{3+} and Ni^{3+} . According to gas adsorption technique study, it found that all the prepared $\text{AgFe}_{1-x}\text{M}_x\text{O}_2$ nanoparticles display the typical characteristic of mesoporous materials. Furthermore, the results of electrochemical performance demonstrated that each of the electrodes has the mechanism for charge storage through a pseudocapacitive process involving the incorporation of metal and/or metal oxides. The $\text{AgFe}_{0.85}\text{Ni}_{0.15}\text{O}_2$ nanoparticles show the highest specific capacitance value of 339.08 F/g among all the samples, with corresponding specific energies and powers of 109.28 Wh/kg and 800.51 W/kg, as well as long-term cycle stability of 87.04% at the current density of 1 A/g. However, all the samples provided high capacitance retention values greater than 80%, which reveals that the delafossite AgFeO_2 -based nanostructures have potential as a candidate for the future electrode material in the energy storage applications.



School of Physics
Academic Year 2023

Student's Signature _____
Advisor's Signature _____

Signature
Signature

ACKNOWLEDGEMENTS

I want to begin by thanking my advisor, Prof. Dr. Santi Maensiri, for his unwavering support, guidance, and counsel throughout this attempt, which drew on his extensive expertise and experience. Further, I'm pleased to convey my gratitude to the members of my thesis examination committee, Assoc. Prof. Dr. Worawat Meewasna, Asst. Prof. Dr. Wittawat Saengrang and Dr. Narong Chanlek for their insightful comments, thoughtful suggestions and critical evaluation of my research.

I really appreciate the assistance and cooperation of all the staffs and members of School of Physics, Institute of Science, Suranaree University of Technology, Advanced Materials Physics (AMP) group, and Synchrotron Light Research Institute (SLRI).

I would like to thank One Research One Graduate scholarship for the financial support of my M.Sc. degree. In addition, I gratefully acknowledge all supports from the SUT CoE on Advanced Functional Materials (SUT-AFM), Suranaree University of Technology, Thailand Science, Research and Innovation (TSRI), National Science, Research and Innovation Fund (NSRF).

Lastly, I want to acknowledge my parents, sister, and brother for their wonderful love, fantastic encouragement, and support throughout my M.Sc. studies.

Choulong Veann

CONTENTS

	Page
ABSTRACT IN THAI	I
ABSTRACT IN ENGLISH	III
ACKNOWLEDGEMENTS	V
CONTENTS	VI
LIST OF TABLES	X
LIST OF FIGURES	XI
LIST OF ABBREVIATIONS.....	XVIII
CHAPTER	
I INTRODUCTION	1
1.1 Background and significance of the study.....	1
1.2 Research objective.....	3
1.3 Scope and limitation	4
1.4 Location of the research.....	4
1.5 Expected results.....	4
1.6 Thesis structure	5
II LITERATURE REVIEWS.....	6
2.1 Conventional capacitor.....	6
2.2 Electrochemical capacitors.....	7
2.2.1 Electrical double layer capacitors.....	8
2.2.2 Pseudocapacitors	11
2.3 Delafossite silver ferrite (AgFeO ₂)	13
2.4 Electrochemical properties of AgFeO ₂	15
III RESEARCH METHEDODOLOGY.....	20
3.1 Raw Materials.....	20

CONTENTS (Continued)

	Page
3.2 Co-precipitation method and synthesis of AgFeO ₂ -based nanostructures.....	20
3.3 Material characterization technique.....	25
3.3.1 X-ray diffraction technique (XRD)	25
3.3.2 Scanning electron microscopy (SEM)	27
3.3.3 Transmission electron microscopy (TEM)	29
3.3.4 Nitrogen (N ₂) adsorption technique	31
3.3.4.1 Pore size distribution.....	33
3.3.4.2 Brunauer-Emmett-Teller method (BET)	34
3.3.5 X-ray absorption spectroscopy (XAS)	34
3.3.6 X-ray photoelectron spectroscopy (XPS)	38
3.4 Electrochemical measurement.....	39
3.4.1 Cyclic voltammetry (CV)	40
3.4.2 Galvanostatic charge discharge (GCD)	42
3.4.3 Electrochemical impedance spectroscopy (EIS)	43
3.4.4 Preparation of working electrode.....	45
IV RESULTS AND DISCUSSION.....	47
4.1 AgFeO ₂ nanoparticles.....	47
4.1.1 Structure and morphologies analysis of AgFeO ₂ nanoparticles by XRD, TEM and SEM	47
4.1.2 Oxidation state and surface chemical composition study of AgFeO ₂ nanoparticles by XAS and XPS.....	52
4.1.3 Surface area pore volume and distribution of pore size analysis of AgFeO ₂ nanoparticles by BJH and BET methods	61
4.1.4 Electrochemical performance of AgFeO ₂ nanoparticles.....	65
4.1.4.1 Cyclic voltammetry performance.....	65

CONTENTS (Continued)

	Page
4.1.4.2 Galvanostatic charge discharge measurement.....	68
4.1.4.3 Electrochemical impedance spectroscopy analysis	72
4.1.4.4 Specific energy and specific power study	73
4.2 Co-doped AgFeO ₂ nanoparticles	75
4.2.1 Structure and morphologies analysis of the Co-doped AgFeO ₂ nanoparticles by XRD, TEM and SEM.....	75
4.2.2 Oxidation state and surface chemical composition study of Co-doped AgFeO ₂ nanoparticles by XAS and XPS	79
4.2.3 Surface area, pore volume and distribution of pore size analysis of Co-doped AgFeO ₂ nanoparticles by BJH and BET methods.....	89
4.2.4 Electrochemical performance of Co-doped AgFeO ₂ nanoparticles.....	92
4.2.4.1 Cyclic voltammetry performance	92
4.2.4.2 Galvanostatic charge discharge measurement.....	95
4.2.4.3 Electrochemical impedance spectroscopy analysis	98
4.2.4.4 Specific energy and specific power study.....	100
4.3 Ni-doped AgFeO ₂ nanoparticles.....	101
4.3.1 Structure and morphologies analysis of the Ni-doped AgFeO ₂ nanoparticles by XRD, TEM and SEM.....	101
4.3.2 Oxidation state and surface chemical composition study of Ni-doped AgFeO ₂ nanoparticles by XAS and XPS.....	105
4.3.3 Surface area, pore volume and distribution of pore size analysis of Ni-doped AgFeO ₂ nanoparticles by BJH and BTE methods.....	115

CONTENTS (Continued)

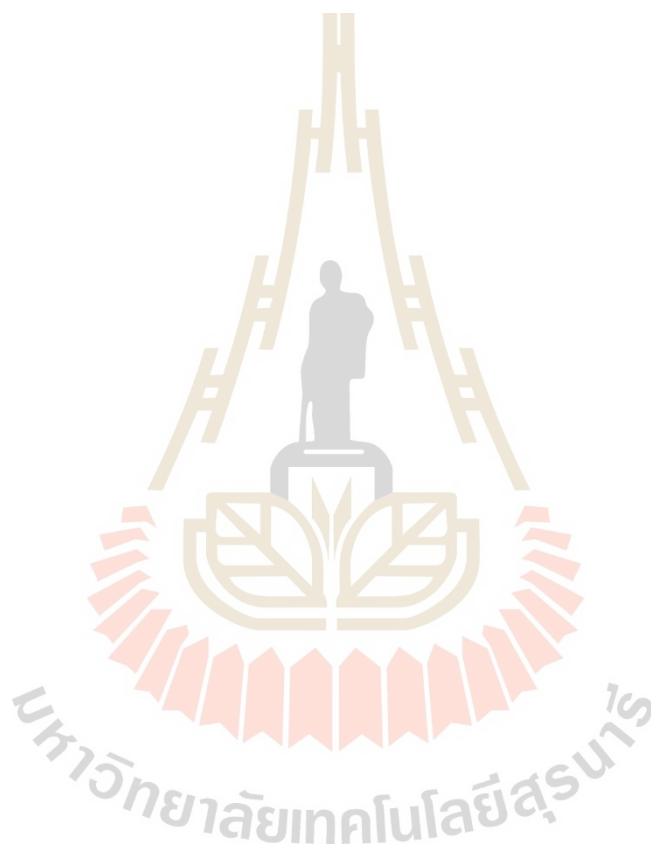
	Page
4.3.4 Electrochemical performance of Ni-doped AgFeO ₂ nanoparticles.....	119
4.3.4.1 Cyclic voltammetry performance	119
4.3.4.2 Galvanostatic charge discharge measurement.....	121
4.3.4.3 Electrochemical impedance spectroscopy analysis	124
4.3.4.4 Specific energy and specific power study	125
V CONCLUSIONS AND SUGGESTIONS	127
5.1 Effect of different calcination temperatures on structure and electrochemical performance of AgFeO ₂ nanoparticles	127
5.2 effect of Co and Ni-doped AgFeO ₂ on structure and electrochemical performance.....	128
5.3 Suggestions	129
REFERENCES	130
APPENDIX.....	138
CURRICULUM VITAE.....	142

LIST OF TABLES

Table	Page
2.1	Reports of metal oxides electrode material for pseudocapacitors 13
2.2	The lattice parameters values of delafossite AgFeO_2 nanoparticles 15
3.1	The advantages and disadvantages comparison of co-precipitation with other methods 21
3.2	Expression of the calculated amounts of starting materials employed for the synthesis of AgFeO_2 -based nanoparticles 23
4.1	2H and 3R percentages in AgFeO_2 structure at various calcination temperatures 48
4.2	The oxidation states with corresponding edge energies of the references and prepared AgFeO_2 nanostructures 53
4.3	Porosity parameters of AgFeO_2 nanoparticles 64
4.4	The summarized results of the calculated specific capacitance values of AgFeO_2 electrode received from GCD method 72
4.5	Energy edge position and corresponding valence states of the reference standard and $\text{AgFe}_{1-x}\text{M}_x\text{O}_2$ samples 83
4.6	The values specific surface area, pore volume and pore size of the $\text{AgFe}_{1-x}\text{Co}_x\text{O}_2$ 92
4.7	List of the specific capacitance values of Co-doped AgFeO_2 nanoparticles with various Co concentrations calculated employing GCD technique 97
4.8	Energy edge position and corresponding valence states of the reference standard and Ni-doped AgFeO_2 109
4.9	BET specific surface area, pore volume and average pore size values for the $\text{AgFe}_{1-x}\text{Ni}_x\text{O}_2$ nanoparticles with various Ni content 118

LIST OF TABLES (Continued)

Table		Page
4.10	List of the specific capacitance values of $\text{AgFe}_{1-x}\text{Ni}_x\text{O}_2$ nanoparticles, calculated employing GCD technique	123



LIST OF FIGURES

Figure		Page
1.1	A comparison graph of energy storage technology of Ragone plot between specific energy and specific power.....	1
2.1	Schematic of the types of supercapacitors.....	8
2.2	The construction of a double-layer capacitor.....	9
2.3	Three different types of the faradaic mechanism of pseudocapacitive materials.....	12
2.4	AgFeO ₂ structure with the 3R and 2H types.....	14
2.5	CV curve at the slow scan rate of 5×10 ⁻⁵ V/s of AgFeO ₂ electrochemical cell.....	16
2.6	Discharge capacitance retention after 50 cycles of AgFeO ₂ electrochemical cell.....	16
2.7	(a) Discharge/charge profile of galvanostatic of a Li half-cell that uses composite AgFeO ₂ as the electrode material. (b) The average values of charge and discharge potentials per cycle of Li half-cell. (c) The charge/discharge capacities of cycle performance. (d) Round-trip and coulombic efficiencies of Li half-cell.....	17
2.8	(a) Charge/discharge profiles of galvanostatic of a full Li-ion cell. (b) The average values evolution of discharge and charge potentials of Li full-cell. (c) The charge/discharge capacities of cycle performance. (d) Round-trip and coulombic efficiencies of Li full-cell.....	18
2.9	CV curves at different scan rates of 1 mV/s to 100 mV/s of AgFeO ₂ nanoparticles at the calcination temperature of 400°C.....	19
2.10	Cyclic voltammetry (CV) curves of AgFeO ₂ -400/AC as a scan rate function.....	19

LIST OF FIGURES (Continued)

Figure	Page
3.1 A diagram of the synthesis process and the characterization of $\text{AgFe}_{1-x}\text{M}_x\text{O}_2$ nanoparticles.....	24
3.2 The schematic illustration of Bragg's law interpretation	26
3.3 Representing the SEM components.....	27
3.4 Schematic diagram of TEM components.....	31
3.5 Classification of adsorption isotherm.....	32
3.6 Representing the regions of XANES and EXAFS for XAS spectrum	36
3.7 The typical mode of XAS measurement.....	37
3.8 Schematic diagram of XPS principle	38
3.9 Electrochemical measurement system includes a three-electrode system, potentiostat/galvanostat and a computer.....	40
3.10 CV curve of the ideal EDLC and pseudocapacitor.....	41
3.11 GCD curve.....	42
3.12 The impedance of complex plane plots (a) non-Faradaic region and (b) Faradaic electron transfer with mass transfer	45
4.1 The pattern of XRD of AgFeO_2 nanoparticles calcined at various temperatures ranging from 100°C to 500°C	48
4.2 FESEM images of the pure AgFeO_2 samples calcined at different temperatures (a) 100°C , (b) 200°C , (c) 300°C , (d) 400°C and (e) 500°C	49
4.3 The bright field images of TEM with the associating SAED of the synthesized AgFeO_2 samples calcined spanning from (a,b) 100°C and (l,j) 500°C , respectively.....	50
4.4 (a) Normalized XANES with (b) associating first derivative plot of the synthesized AgFeO_2 samples at Ag L3-edge	54

LIST OF FIGURES (Continued)

Figure	Page
4.5	Normalized XANES plot of the synthesized AgFeO_2 samples at Fe K-edge ... 55
4.6	XPS survey spectrum of the prepared AgFeO_2 calcined at different temperatures 57
4.7	XPS spectrum at Ag 3d of all the prepared AgFeO_2 nanoparticles 58
4.8	XPS spectrum at Fe 2p of all the prepared AgFeO_2 samples..... 59
4.9	XPS spectrum at O 1s of all the prepared AgFeO_2 samples..... 60
4.10	The pore size distribution (inset) and N_2 adsorption-desorption isotherm of the AgFeO_2 sample calcined at (a) 100°C, (b) 200°C, (c) 300°C, (d) 400°C, and (e) 500°C..... 62
4.11	CV curves at ranging from 2 mV/s to 100 mV/s scan rates of the prepared AgFeO_2 nanoparticles calcined at at (a) 100°C, (b) 200°C, (c) 300°C, (d) 400°C, and (e) 500°C..... 67
4.12	The calculated specific capacitance at the various scan rates of the synthesized AgFeO_2 nanoparticle calcined at different temperatures 68
4.13	Galvanostatic charge/discharge plot of the AgFeO_2 sample at the various current densities of 1, 2, 5, 10, and 20 A/g..... 70
4.14	The calculated specific capacitance at the various current density of 1, 2, 5, 10 and 20 A/g of the synthesized AgFeO_2 nanoparticle calcined at different temperatures 71
4.15	Capacitance retention (%) after 1000 cycles at 5 A/g of the AgFeO_2 electrodes calcined at different temperatures 71
4.16	Nyquist plots of AgFeO_2 samples calcined at various temperatures 73
4.17	The specific energies and their corresponding specific powers of AgFeO_2 nanostructures at different current densities ranging from 1 to 20 A/g 74
4.18	XRD patterns of the $\text{AgFe}_{1-x}\text{Co}_x\text{O}_2$ nanoparticles..... 76

LIST OF FIGURES (Continued)

Figure	Page
4.19	77
The images of FESEM of $\text{AgFe}_{1-x}\text{Co}_x\text{O}_2$ samples: (a) $x = 0.00$, (b) $x = 0.05$, (c) $x = 0.10$, (d) $x = 0.15$ and (e) $x = 0.20$	
4.20	78
TEM images and associating SAED of $\text{AgFe}_{1-x}\text{Co}_x\text{O}_2$ nanoparticle: (a,b) $x = 0.00$, (c,d) $x = 0.05$, (e,f) $x = 0.10$, (g,h) $x = 0.15$, and (i,j) $x = 0.20$	
4.21	80
Normalized XANES spectrum spectra at Ag L3-edge of Co-doped AgFeO_2 nanoparticles.....	
4.22	81
Normalized XANES plot at Ag L3-edge of Co-doped AgFeO_2 with different concentration	
4.23	82
(a) Normalized XANES with (b) the first derivative plot at Ag L3-edge of Co-doped AgFeO_2 with different concentration.....	
4.24	85
XPS spectrum of $\text{AgFe}_{1-x}\text{Co}_x\text{O}_2$ samples at Ag 3d with different Co concentrations.....	
4.25	86
XPS spectrum of $\text{AgFe}_{1-x}\text{Co}_x\text{O}_2$ samples at Fe 2p with different Co concentrations.....	
4.26	87
XPS spectrum of $\text{AgFe}_{1-x}\text{Co}_x\text{O}_2$ nanostructures at Co 2p with different contents.....	
4.27	88
XPS spectrum of $\text{AgFe}_{1-x}\text{Co}_x\text{O}_2$ nanostructures at O 1s with various Co contents.....	
4.28	90
The pore size distribution (inset) and N_2 adsorption-desorption isotherms and of $\text{AgFe}_{1-x}\text{Co}_x\text{O}_2$ with (a) $x = 0.00$, (b) $x = 0.05$, (c) $x = 0.10$, (d) $x = 0.15$ and (e) $x = 0.20$	
4.29	94
CV curves of Co-doped AgFeO_2 nanoparticles at different scan rates with (a) $x = 0.00$, (b) $x = 0.05$, (c) $x = 0.10$, (d) $x = 0.15$, (e) $x = 0.20$, and (f) The values of calculated specific capacitance.....	

LIST OF FIGURES (Continued)

Figure	Page
4.30	GCD plot of Co-doped AgFeO_2 nanoparticles with (a) $x = 0.00$, (b) $x = 0.05$, (c) $x = 0.10$, (d) $x = 0.15$, (e) $x = 0.20$, and (f) the specific capacitance values at various current densities..... 96
4.31	Capacitance retention (%) of $\text{AgFe}_{1-x}\text{Co}_x\text{O}_2$ electrodes with $x = 0.00$, 0.05, 0.10, 0.15 and 0.20 98
4.32	EIS curves of Co-doped AgFeO_2 nanoparticles with different Co contents..... 99
4.33	Specific energies and corresponding specific power of Co-doped AgFeO_2 nanoparticles at current densities of 1, 2, 5, 10 and 20 A/g..... 100
4.34	XRD patterns of $\text{AgFe}_{1-x}\text{Ni}_x\text{O}_2$ nanostructures with various Ni concentrations..... 102
4.35	The images of FESEM of $\text{AgFe}_{1-x}\text{Ni}_x\text{O}_2$ samples: (a) $x = 0.00$, (b) $x = 0.05$, (c) $x = 0.10$, (d) $x = 0.15$ and (e) $x = 0.20$ 103
4.36	TEM images and associating selected area electron diffraction (SAED) and HRTEM of $\text{AgFe}_{1-x}\text{Ni}_x\text{O}_2$ nanoparticle: (a,b,c) $x = 0.00$, (d,e,f) $x = 0.05$, (g,h,i) $x = 0.10$, (j,k,l) $x = 0.15$ and (m,n,o) $x = 0.20$ 104
4.37	(a) Normalized XANES with (b) the corresponding first derivative spectra at Ag L3-edge of Ni-doped AgFeO_2 nanoparticles with different Ni concentrations..... 106
4.38	(a) Normalized XANES and (b) the associating first derivative plot at Fe K-edge of Ni-doped AgFeO_2 nanoparticles with different Ni concentrations..... 107
4.39	(a) Normalized XANES spectrum plot at Ni K-edge of $\text{AgFe}_{1-x}\text{Ni}_x\text{O}_2$ nanoparticles at different Ni concentrations 108
4.40	XPS spectra at Ag 3d of $\text{AgFe}_{1-x}\text{Ni}_x\text{O}_2$ nanoparticles 111
4.41	XPS spectra at Fe 2p of $\text{AgFe}_{1-x}\text{Ni}_x\text{O}_2$ samples..... 112

LIST OF FIGURES (Continued)

Figure	Page
4.42 XPS spectra at Ni 2p of $\text{AgFe}_{1-x}\text{Ni}_x\text{O}_2$ samples where x spanning from 0.000 to 0.20.....	113
4.43 XPS spectra at O1s of $\text{AgFe}_{1-x}\text{Ni}_x\text{O}_2$ nanoparticles with different concentrations.....	114
4.44 The pore size distribution (inset) and N_2 adsorption-desorption isotherms of $\text{AgFe}_{1-x}\text{Ni}_x\text{O}_2$ samples with (a) $x = 0.00$, (b) $x = 0.05$, (c) $x = 0.10$, (d) $x = 0.15$, and (e) $x = 0.20$	116
4.45 CV curves of $\text{AgFe}_{1-x}\text{Ni}_x\text{O}_2$ nanoparticles at different scan rates with (a) $x = 0.00$, (b) $x = 0.05$, (c) $x = 0.10$, (d) $x = 0.15$, (e) $x = 0.20$, and (f) the values of calculated specific capacitance.....	120
4.46 GCD plot of $\text{AgFe}_{1-x}\text{Ni}_x\text{O}_2$ nanoparticles with (a) $x = 0.00$, (b) $x = 0.05$, (c) $x = 0.10$, (d) $x = 0.15$, (e) $x = 0.20$, and (f) the values of specific capacitance at various current densities.....	122
4.47 Capacitance retention (%) of $\text{AgFe}_{1-x}\text{Ni}_x\text{O}_2$	123
4.48 Nyquist plot of $\text{AgFe}_{1-x}\text{Ni}_x\text{O}_2$ electrodes	125
4.49 Specific energies and corresponding specific power of Ni-doped AgFeO_2 electrodes at current densities of 1, 2, 5, 10 and 20 A/g.....	126

LIST OF ABBREVIATIONS

XRD	X-ray diffraction
SEM	Scanning electron microscopy
FESEM	Field emission scanning electron microscopy
TEM	Transmission electron microscopy
HRTEM	High resolution transmission electron microscopy
SAED	Selected area electron diffraction
XANES	X-ray absorption near edge structure
XAS	X-ray absorption spectroscopy
XPS	X-ray photoelectron spectroscopy
BET	Brunauer-Emmett-Teller method
BJH	Barrett-Joyner-Halenda method
CV	Cyclic voltammetry
GCD	Galvanostatic charge discharge
EIS	Electrochemical impedance spectroscopy
PVDF	Polyvinylidene difluoride
CB	Carbon black
NMP	N-methyl pyrrolidone

CHAPTER I

INTRODUCTION

1.1 Background and significance of the study

Recently, there has been an increase in global energy demand. With environmental concerns such as global warnings, renewable energy sources become a good choice. Energy storage and conservation have become candidates for harvesting and regulating renewable energy from solar, wind, and tide sources. Among all energy storage technology, supercapacitors have gotten attention because they have a high power density (Figure 1), long life use, and quick charge/discharge process when compares to batteries (Béguin, Presser, Balducci, and Frackowiak, 2014). They are used in various applications, including portable devices, hybrid electric vehicles, and other domestic applications.

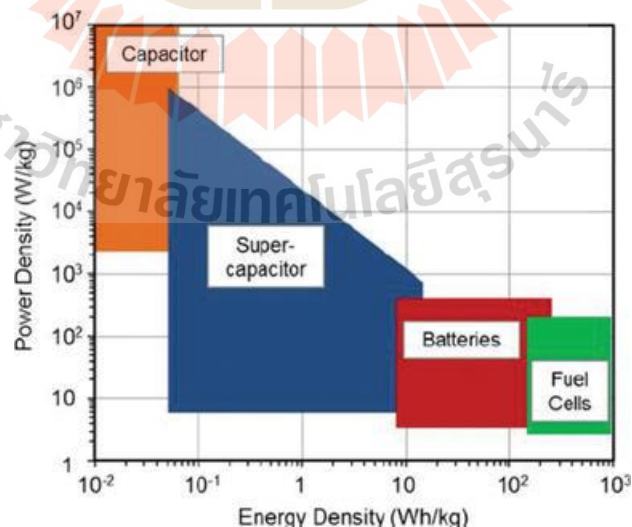


Figure 1.1 A comparison graph of energy storage technology of Ragone plot between specific energy and specific power (Adapted from (Guo, Gupta, and Teng, 2018)).

In general, there are two types of supercapacitors i.e., pseudocapacitors and electrical double-layer capacitors (EDLCs). Carbon materials, such as graphene and porous carbon are developed for the EDLCs electrode. EDLC is an energy storage device that stores electrical energy by separating positive and negative charges at the interface between a porous electrode and an electrolyte. Basically, the disadvantage of EDLCs is low power density. Compared with EDLCs, the pseudocapacitors showed much higher specific capacity and power density (Okashy, Noked, Zimrin, and Aurbach, 2013). Therefore, the development of electrode materials with high electrochemical performance for pseudocapacitors is required. Hydroxides and oxides of transition metal have unique crystal structures and multiple oxidation states that enable quick redox/intercalation reactions at their interface exhibiting good performance as pseudocapacitor electrodes. There are many materials used as the pseudocapacitors electrodes such as RuO_2 (Hu and Chen, 2004; Kim and Kim, 2006), MnO_2 (Brousse, Toupin, and Belanger, 2004; Pang, Anderson, and Chapman, 2000; Yang, Wang, Xiong, and Xia, 2007), Fe_2O_3 (Yu et al., 2010), MnCo_2O_4 (Kalawa, Kidkhunthod, Chanlek, Khajonrit, and Maensiri, 2019; Kalawa, Sichumsaeng, Kidkhunthod, Chanlek, and Maensiri, 2022), Bi_2O_3 (Gujar, Shinde, Lokhande, and Han, 2006), Fe_3O_4 (S.-Y. Wang, Ho, Kuo, and Wu, 2005), V_2O_5 (Lee and Goodenough, 1999), In_2O_3 (Prasad, Koga, and Miura, 2004), Bi_2WO_6 (Nithya, Selvan, Kalpana, Vasylechko, and Sanjeeviraja, 2013), SnO_2 (Prasad and Miura, 2004), Co_3O_4 (Gao, Chen, Cao, Wang, and Yin, 2010), NiO (Nam, Yoon, and Kim, 2002; Zhao, Zhang, Liu, Zhang, and Liu, 2013), etc. Among them, iron oxides have been interested in for use as supercapacitors electrode materials due to their three main points: (I) iron has rich chemical redox ($\text{Fe}^0/\text{Fe}^{3+}$, $\text{Fe}^{2+}/\text{Fe}^{3+}$, $\text{Fe}^0/\text{Fe}^{3+}$, $\text{Fe}^{3+}/\text{Fe}^{4+}$, etc.) and multiple oxidation states (Fe^{4+} , Fe^{3+} , Fe^{2+} , Fe^{0+} , etc.), enabling them the high capacity (Qu, Yang, and Feng, 2011). (II) They are non-toxic and more environmentally friendly (M.-S. Wu and Lee, 2009). (III) Iron oxides are earth-abundant and low-cost, which are worthy of being chosen for commercial applications (Shivakomara et al., 2013). In recent years, the oxides of mixed transition metals of iron such as AgFO_2 (Berastegui, Tai, and Valvo, 2018; Farley, Marschilok, Takeuchi, and Takeuchi, 2011; Singh, Mondal, Rath, and Singh, 2021) have been studied as energy storage electrode materials due to

their less toxic, inexpensive, environmentally friendliness and good electrochemical properties.

This study focuses on developing of high-performance supercapacitor electrode materials. The co-precipitation approach was used to create pure AgFeO_2 and $\text{AgFe}_{1-x}\text{M}_x\text{O}_2$ ($\text{M} = \text{Co}$ and Ni) nanoparticles. This method is a simple synthesis, that significantly saves time and energy consumption over other approaches including solid state, hydrothermal and sol-gel. The effects of Co and Ni-doping and calcination temperature in AgFeO_2 nanoparticles on the electrochemical properties were examined. The techniques of SEM, XRD, and TEM were employed to determine the morphology and structure of the synthesized AgFeO_2 -based nanoparticles. The nitrogen gas adsorption technique was utilized to examine the porosity and specific surface area of the AgFeO_2 -based nanoparticles. The oxidation state and elemental composition of the synthesized AgFeO_2 -based samples were examined using XAS and XPS techniques. The working electrodes will be investigated for electrochemical properties by the techniques of CV, GCD and EIS in the electrolyte of 3 M KOH.

1.2 Research objective

1.2.1 To prepare pure AgFeO_2 and $\text{AgFe}_{1-x}\text{M}_x\text{O}_2$ ($\text{M} = \text{Co}$ and Ni) nanoparticles by a co-precipitation route.

1.2.2 To characterize the synthesized pure AgFeO_2 and $\text{AgFe}_{1-x}\text{M}_x\text{O}_2$ ($\text{M} = \text{Co}$ and Ni)

nanoparticles.

1.2.3 To investigate the impact of calcined temperature on the electrochemical performance of AgFeO_2 nanoparticles.

1.2.4 To examine the electrochemical performance of the synthesized $\text{AgFe}_{1-x}\text{M}_x\text{O}_2$ ($\text{M} = \text{Co}$ and Ni) samples.

1.3 Scope and limitations

1.3.1 This work looks into the preparation of pure AgFeO_2 and $\text{AgFe}_{1-x}\text{M}_x\text{O}_2$ ($\text{M} = \text{Co}$ and Ni) nanoparticle by using a co-precipitation method with $x = 0.05, 0.10, 0.15,$ and 0.20 .

1.3.2 The morphology, local structure and microstructure of AgFeO_2 -based nanoparticles are studied by XRD, SEM, TEM, XAS, XPS, and gas absorption techniques.

1.3.3 The influence of calcined temperature on pure AgFeO_2 nanoparticle electrochemical performance is investigated by varying the calcined temperature at $100, 200, 300, 400,$ and 500°C .

1.3.4 The electrochemical properties of $\text{AgFe}_{1-x}\text{M}_x\text{O}_2$ ($\text{M} = \text{Co}$ and Ni) nanoparticles are studied via GCD, CV, and EIS and compare with those of pure AgFeO_2 .

1.4 Locations of the research

1.4.1 The Center for Scientific and Technological Equipment, Suranaree University of Technology, Nakhon Ratchasima, Thailand.

1.4.2 Advanced Materials Physics Laboratory (AMP Lab), School of Physics, Institute of Science, Suranaree University of Technology, Nakhon Ratchasima, Thailand.

1.4.3 Synchrotron Light Research Institute (Public Organization) (SLRI), Nakhon Ratchasima, Thailand.

1.5 Expected results

1.5.1 Having the skill of preparation of pure AgFeO_2 and $\text{AgFe}_{1-x}\text{M}_x\text{O}_2$ nanoparticles.

1.5.2 Gaining a well understanding of the structure and morphology of AgFeO_2 -based nanoparticles such as particle size, crystallography, oxidation state, and porosity.

1.5.3 Improving the electrochemical performance of nanoparticles for using as the supercapacitor electrode and give a good explanation of the influence of the calcined temperatures on the electrochemical properties of AgFeO_2 -based nanoparticles.

1.5.4 Gaining experience in the fabrication of the AgFeO_2 -based nanoparticles electrode and measurement of their electrochemical properties.

1.5.5 Publication in International ISI journals.

1.6 Thesis structure

There are five chapters in this thesis. The first chapter serves as the introduction and provides an overview of the research conducted. In the second chapter, Chapter II, relevant literature reviews are presented, covering topics such as the basics of the normal capacitor, electrochemical capacitor or supercapacitor and the AgFeO_2 structure and the electrochemical performance. The third chapter focuses on the fabrication and characterisation of AgFeO_2 -based nanoparticles, along with the inclusion of electrochemical measurement. The obtained results from this research and subsequent discussion are presented in Chapter IV. Finally, Chapter V concludes the dissertation by summarizing the findings and providing suggestions for future research endeavors.

CHAPTER II

LITERATURE REVIEWS

2.1 Conventional capacitor

A conventional capacitor or an electrostatic capacitor is a passive component of electronics which can store and release the energy of electricity. It is made up of two conductive plates separated by a dielectric. The conductive plates are typically made of metal and referred to as the conventional capacitor electrode. When provide a voltage difference across the plates, negative and positive charges accumulate on each plate. Between the material of dielectric and the plates, the accumulation of charge produces an electric field, preventing the charge from flowing directly across. The traditional capacitor stores the energy of electricity in an electrostatic field form.

The basic idea is that the capacitor may store electrical energy in an electrical field formed by the buildup of charges on its electrodes. Based on Gauss's law, a capacitor's electric field (E) between its plates is directly proportional to the charge (Q) therein and inversely proportional to the separation (d) between them. Mathematically, this relationship can be expressed as:

$$E = \frac{Q}{\epsilon_0 A} \quad (2.1)$$

where E is the strength of electric field, Q is the charge on the plates, ϵ_0 is the free space permittivity of (a fundamental constant) and A represents the plates surface area.

Basically, the value of capacitance (C) of a capacitor, measured in farad (F), determines its ability to store electrical energy. It depends on several factors,

including the distance between the plates, the properties of dielectric material and the surface area of the plates. Capacitors with larger surface area of the plate, smaller plate separation distances and high permittivity dielectric have higher capacitance values. The Equation that uses to determine a capacitor's capacitance (C) value is as follows:

$$C = \frac{Q}{V} \quad (2.2)$$

where V is the difference in potential between two electrodes and Q is the total electrical charge on each electrode.

Moreover, the capacitance value can also be written as the function of the surface area A of conducting plate and the distance d between them as follow:

$$C = \frac{\epsilon_0 \epsilon_r A}{d} \quad (2.3)$$

where ϵ_0 represents a constant value of the dielectric in a vacuum, ϵ_r represents the constant value of the relative dielectric of materials and.

When the voltage across a capacitor is changed, the charge on the plates adjusts accordingly. The stored energy of the capacitor is determined by equation:

$$E = \frac{CV^2}{2} \quad (2.4)$$

2.2 Electrochemical capacitors

An electrochemical capacitor or ultracapacitor (supercapacitor), is a type of energy storage device which bridges the gap between batteries and traditional capacitors. It was first invented in 1957 by Howard Becker of General Electric (GE). Supercapacitors store energy the electrical through electrostatic double layer capacitance (EDLC) and pseudocapacitance mechanisms. It offers rapid charge/discharge capabilities, long cycle life, high power density. Two electrodes are separated by an electrolyte and a separator in a supercapacitor. The electrodes are often comprised of materials with a high surface area like activated carbon, carbon nanotubes, metal oxides and conducting polymer. Generally, Electrochemical capacitors are categorized into two main types: (i) electrochemical double-layer

capacitor that apply carbon as the electrode materials and (ii) pseudocapacitor that use conducting polymer and metal oxides as the electrode materials, as exhibited in Figure 2. The basic energy storage method in supercapacitors is electrostatic double layer capacitance. When a voltage is given to the electrolyte, charge ions collect at the electrode-electrolyte contact, forming a double layer of charge. This electrical double layer stores energy and contributes to the overall capacitance. Supercapacitors exhibit pseudocapacitive behavior, which involves reversible redox process at the surface of electrode. Pseudocapacitance is associated with the transfer of charge between the electrode material and the electrolyte, allowing for additional energy storage beyond the double layer capacitance.

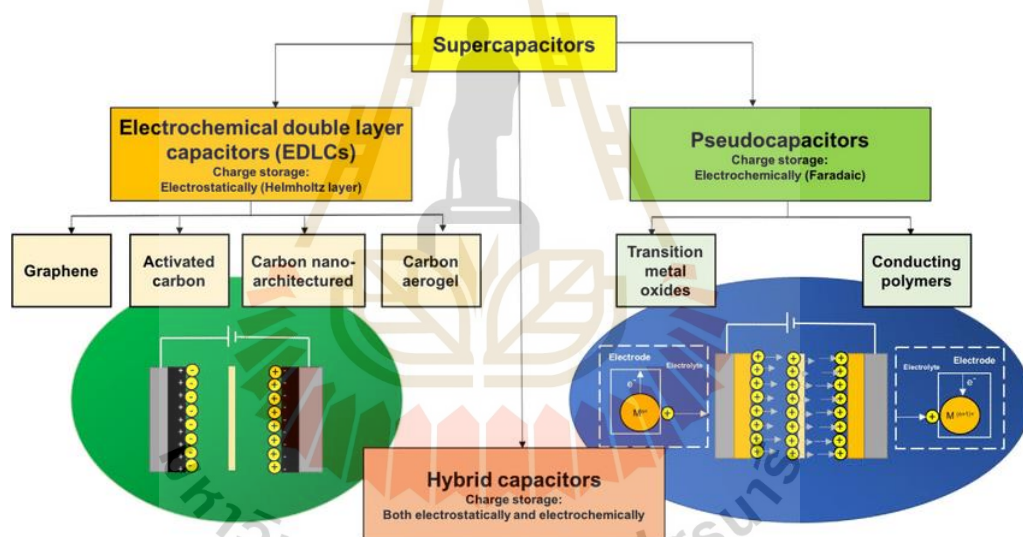


Figure 2.1 Schematic of the types of supercapacitors (Adapted from (Abdah, Azman, Kulandaivalu, and Sulaiman, 2020)).

2.2.1 Electrical double layer capacitors

Electric double-layer capacitor (EDLCs) is another term use to describe electrochemical capacitor or supercapacitor. The graphene and carbon nanotubes (CNTs) have been interesting materials for use as electrodes for EDLCs due to their properties such as high surface area and good conducting. In 2011, An et al. reported

that CNTs have a high 180 F/g specific capacitance with 20 kW/kg power density and 7 Wh/kg energy density (An et al., 2001). Further, in 2009, Wang et al. (Wang et al., 2009) obtained the high 205 F/g specific capacitance from the measurement of graphene with 20kW/g power density and 7 Wh/g energy density. The concept of the electric double layer was represented by von Helmholtz. As shown in Figure 3, EDLCs contain two electrodes that are separated by a separator and used the electrolyte as the ionic connection to each other. The electrolyte is a solution of positive and negative ions in a solvent like water. The surface of each of the two electrodes has an area where the liquid electrolyte comes into touch with the electrode conducting metallic surface which these interfaces are bordered between the two different phases of matter. The double-layer effect occurs in these interfaces. An electrical double layer is generated by the electrodes in the capacitor when applying a voltage to the electrochemical capacitor. There are two layers of charge that make up these double layers. One electrical layer is found in the electrode's surface lattice structure, while the other, with opposite polarity, originates from the electrolyte's dissolved and solvated ions. The solvent molecule monolayer is a separator between these two layers.

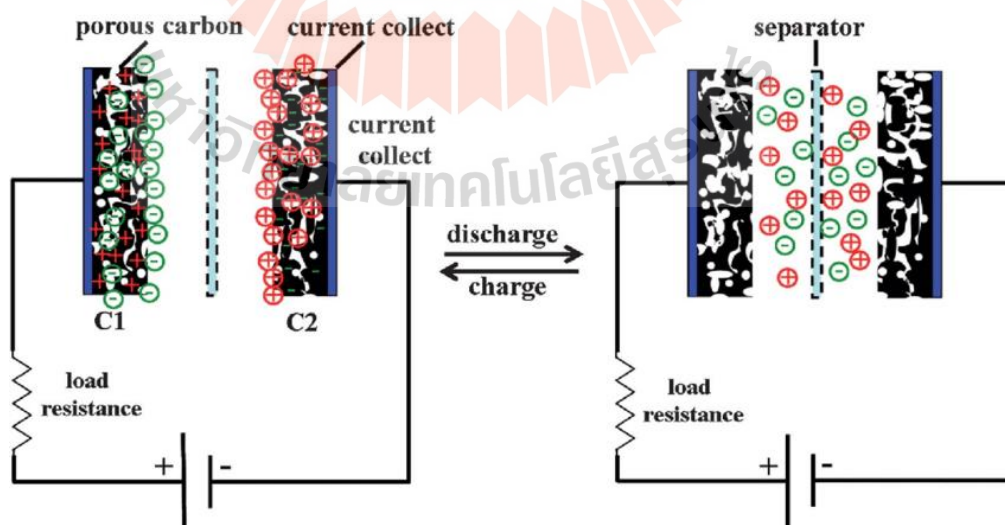


Figure 2.2 The construction of a double-layer capacitor (Adapted from (Wu and Xu, 2014)).

EDLCs can deliver and absorb high power quickly due to their low internal resistance. This makes them suitable for applications that require rapid energy transfer such as regenerative braking systems or power backup solutions. It can undergo numerous charge and discharge cycles without significant degradation. They are designed to maintain their performance over a large number of cycles, often in the range of hundreds of thousands to millions of cycles. Compared to batteries, EDLCs generally have a lower energy density, meaning they can store less energy per unit weight or volume. However, they compensate for this with their high power density and fast charge/discharge capabilities. The physics equations related to EDLCs involve principles of electrostatic, electrical circuits and energy storage. The capacitance of an EDLC represents its ability to store electrical charge. It is given by the equation:

$$C = \frac{Q}{V} \quad (2.5)$$

where C is the capacitance (F), Q is the total electrical charge on each electrode (C), and V is the different potential between two electrodes (V). The energy stored in an EDLC can be calculated using the equation:

$$E = \frac{CV^2}{2} \quad (2.6)$$

where E is the stored energy (J), C is the capacitance (F) and V is the voltage across the EDLC (V). Furthermore, the power delivered or absorbed by an EDLC can be determined by equation:

$$P = \frac{dE}{dt} = V \frac{dQ}{dt} \quad (2.7)$$

where P is the power (W), E is the energy stored (J), t is time (s), V is the voltage across the EDLC (V) and $\frac{dQ}{dt}$ is the rate of change of the charge with respect to time (C/s).

Moreover, another important parameter in determining the device's performance of EDLC is the equivalent series resistance (ERS). The ERS represents the internal resistance of the EDLC. It can be included in the circuit model of an EDLC.

2.2.2 Pseudocapacitors

A pseudocapacitor is a type of electrochemical capacitor that exhibits capacitance beyond the electrostatic double layer capacitance. Unlike electric double layer capacitors (EDLCs) that rely solely on the physical separation of charges at the electrode-electrolyte interface, pseudocapacitors involve additional redox reactions that contribute to the overall capacitance. The transition metal oxides such as MnO_2 , RuO_2 , IrO_2 , and conducting polymers like polyaniline (Table 2.1) have been used as the electrode materials in pseudocapacitors because they have excellent behavior of faradaic redox reactions, intercalation, or electrosorption process. The key feature of pseudocapacitors is the occurrence of faradaic reactions, which involve reversible and fast redox (oxidation-reduction) reaction. The three faradaic mechanisms such as redox pseudocapacitance, underpotential deposition, and intercalation pseudocapacitance, as seen in Figure 4 that can guide to increase the capacitance performance were identified by Conway (Conway, 2013). Underpotential deposition is a phenomenon that occurs during an electrochemical process involving the deposition of a metal onto an electrode surface. It refers to the deposition of a metal at a potential that is more negative than its thermodynamically expected potential. Redox pseudocapacitance occurs when the energy storage mechanism in a system involves redox reactions at the electrode-electrolyte interface. It is a combination of both electrical double layer capacitance (EDLC) and faradaic redox reactions. Intercalation pseudocapacitance refers to the process in which guest species, typically ions or molecules, are inserted or intercalated into the crystal structure of host materials.

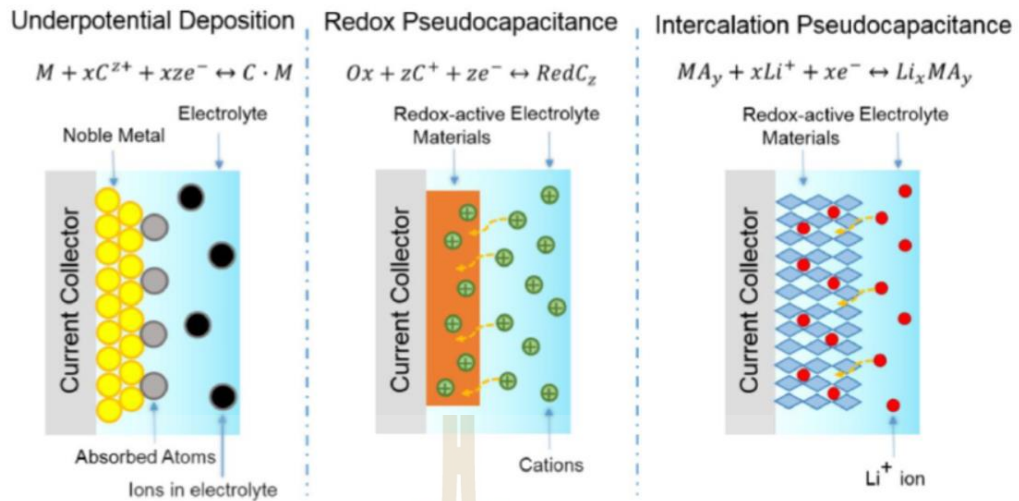


Figure 2.3 Three different types of the faradaic mechanism of pseudocapacitive materials (Adapted from (Jiang, 2019)).

Generally, redox material is regularly allocated on the layer of electrode. The redox reaction is explained as follow (A. Yu, Chabot, and Zhang, 2013):



where O_x is the oxidized types, n is the amount of electrons exchange in the reduction/oxidation reaction, and R_d is the reduced types. The flow of charge associated with the redox reaction in the pseudocapacitor is represented by faradaic current. It can be calculated using Faraday's law of electrolysis:

$$i = nFv \quad (2.9)$$

where i is faradaic current (A), n is the transferred electrons number in redox reaction, F is Faraday's constant ~ 96485 C/mol and v is the rate of reaction (mol/s).

The importance of pseudocapacitive materials is mainly recognized by the fact that they have a higher capacitance than EDLC. The computed specific capacitance value (C) of pseudocapacitor material can be determined by equation as follows (Zhi, Xiang, Li, Li, and Wu, 2013):

$$C = \frac{nF}{MV} \quad (2.10)$$

where n is the electron amount exchanged in the redox reaction, F is the constant value of Faraday, V represents the window of potential, and M is the molar mass.

Table 2.1 Reports of metal oxides electrode material for pseudocapacitors.

Electrode materials	Electrolytes	Specific capacitances (F/g)	References
MnO ₂	0.5 M K ₂ SO ₄	261	(Yang et al., 2007)
AgFeO ₂	1 M Na ₂ SO ₄	110.4	(Abhay et al., 2021)
MnO ₂	0.1 M H ₂ SO ₄	678	(Pang et al., 2000)
Fe ₃ O ₄	1 M Mn ₂ SO ₃	170	(Wang et al., 2006)
V ₂ O ₅	2 M KCl	350	(Lee et al., 1999)
MnO ₂ /AC	0.65 M K ₂ SO ₄	678	(Brousse et al., 2004)
NiO	1 M KOH	138	Zhao et al., 2007)
In ₂ O ₃	0.1M Na ₂ SO ₃	190	(Prasad et al., 2004)
SnO ₂	0.1 M Na ₂ SO ₄	285	(Prasad and Miura, 2004)
Bi ₂ O ₃	1 M NaOH	98	(Gurja et al., 2006)
NiO	1 M KOH	278	(Nam et al., 2002)
Bi ₂ WO ₆	1 M KOH	608	(Nithya et al., 2013)
BFO nanorods	1 M Na ₂ SO ₄	450	(Rana et al., 2014)
RuO ₂ .H ₂ O	0.5 M H ₂ SO ₄	650	(Kim and Kim, 2006)
BiFeO ₃ thin film	1 M NaOH	81	(Lokhande et al., 2007)
RuO _x .H ₂ O	0.1 M NaOH	1580	(Hue and Chen, 2004)
Co ₃ O ₄	6 M KOH	746	(Gao et al., 2010)

2.3 Delafossite silver ferrite (AgFeO₂)

Delafossite AgFeO₂ is a compound that belongs to the delafossite mineral family. It consists of three elements such as silver (Ag), iron (Fe) and oxygen (O). The compound is known as silver iron (III) oxide. Delafossite compounds have a layered crystal structure with a general formula ABX₂, where A and B are metal cations and X

is an anion. In the case of AgFeO_2 , the silver cation (Ag^+) and iron cation (Fe^{3+}) occupy the A and B positions, respectively, while oxygen (O^{2-}) is the anion.

On the other hand, AgFeO_2 is a non-toxic transition metal oxide that has two types of 3R and 2H structures with space groups of $R\bar{3}m$, $R\bar{3}m$ and $P6_3/mmc$. It succeeded in preparation by the hydrothermal method by Sheets et al. in 2006 (Sheets, Mugnier, Barnabé, Marks, and Poeppelmeier, 2006). In 2017, Siedliska et al. (Siedliska, Pikula, Chocyk, and Jartych, 2017) reported the preparation of AgFeO_2 by co-precipitation route. which show 2H and 3R mixing phases with the space groups of $R\bar{3}m$ and $P6_3/mmc$, respectively as displayed in Figure 5. Moreover, in 2020, Ahmed et al. (Ahmed et al., 2020) successfully synthesized AgFeO_2 delafossite structure nanoparticles using the hydrothermal method which has a $R\bar{3}m$ space group with the parameter values of lattice of $a=3.033 \text{ \AA}$ and $c=18.591 \text{ \AA}$. In this work, Ahmed et al. also studied the comparison of lattice parameters of AgFeO_2 nanoparticles which lists in Table 2.

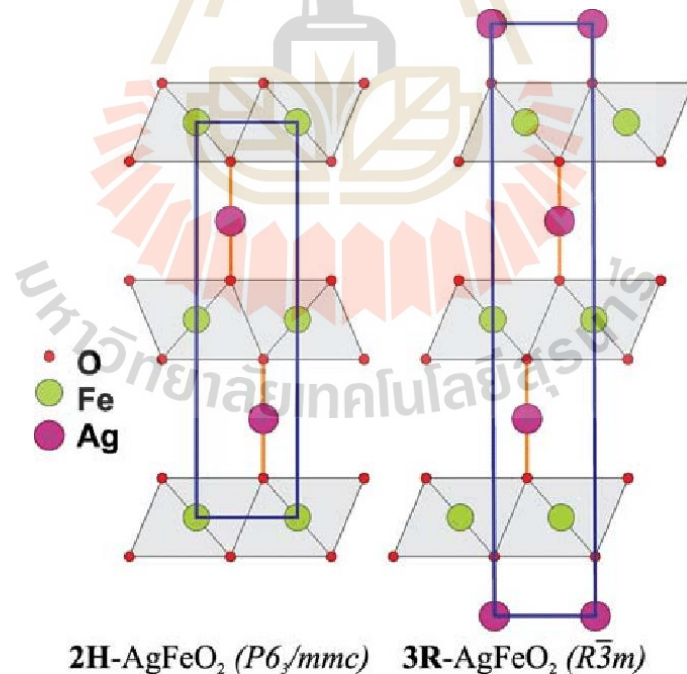


Figure 2.4 AgFeO_2 structure with the 3R and 2H types (Adapted from (Siedliska, Pikula, Chocyk, and Jartych, 2017)).

Table 2.2 The lattice parameters values of delafossite AgFeO₂ nanoparticles.

Lattice parameters		References
a (Å°)	c (Å°)	
3.035	18.592	(Siedliska et al., 2017)
3.03273	18.5838	(Noriki et al., 2013)
3.0393	18.5894	(Presniakov et al., 2014)
3.0391	18.5899	(Noriki et al., 2012)
3.033	18.591	(Ahmed et al., 2020)

2.4 Electrochemical properties of AgFeO₂

AgFeO₂ nanoparticles have become an efficient potential candidate for using as the supercapacitor electrode application because it is combined with transition metal with multiple valence states and rich redox chemistry that show better electrochemical performance.

However, in 2011, Farley et al. studied the electrochemical properties of AgFeO₂. The lithium hexafluoroarsenate (LiAsF₆) is used as the electrolyte for electrochemical performance. The AgFeO₂ materials showed larger voltage recovery with high retention of discharging as shown in Figure 6 and 7. It exhibited the delivery is greater or equal to 0.4 electron equivalents above 1.5 V under a rate of C/5 per hour.

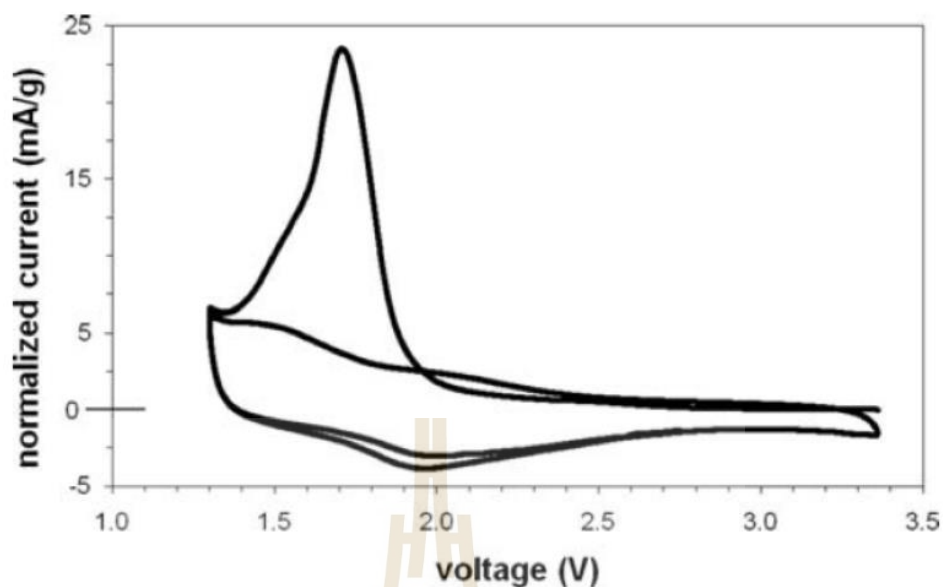


Figure 2.5 CV curve at the slow scan of 5×10^{-5} V/s of AgFeO_2 electrochemical cell (Adapted from (Farley, Marschilok, Takeuchi, and Takeuchi, 2011)).

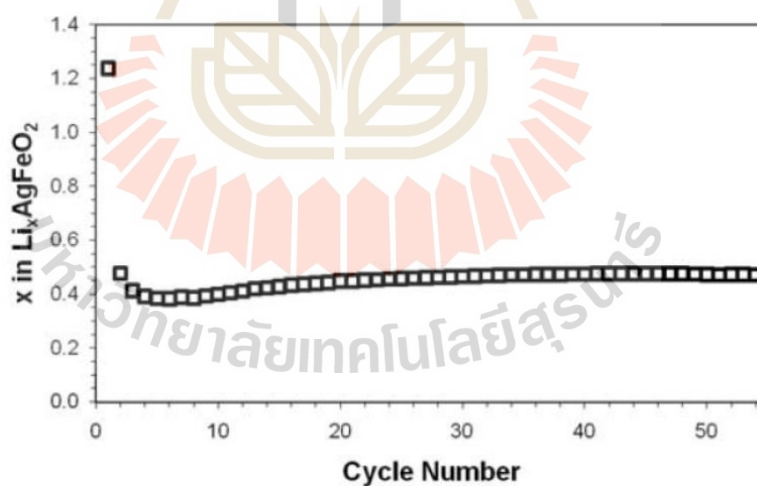


Figure 2.6 Discharge capacitance retention after 50 cycles of AgFeO_2 electrochemical cell (Adapted from (Farley, Marschilok, Takeuchi, and Takeuchi, 2011)).

In 2018, Pedro et al. studied the electrochemical performance of AgFeO_2 for use as the negative electrode in Na- and Li-ion batteries. The electrode of the Na cell is created by the components of AgFeO_2 , Na-alginate, and carbon black (CB) by a ratio

of 75:10:15 by weight, respectively. Furthermore, the Li cell exhibited good performance by using LiFePO_4 and AgFeO_2 as the positive and negative electrodes, respectively. These full cells of an iron-base material showed excellent stability with retention of capacity of $\sim 80\%$ after 100 cycles, average round trip efficiency of 89%, and 3V operational voltage as shown in Figures 8 and 9.

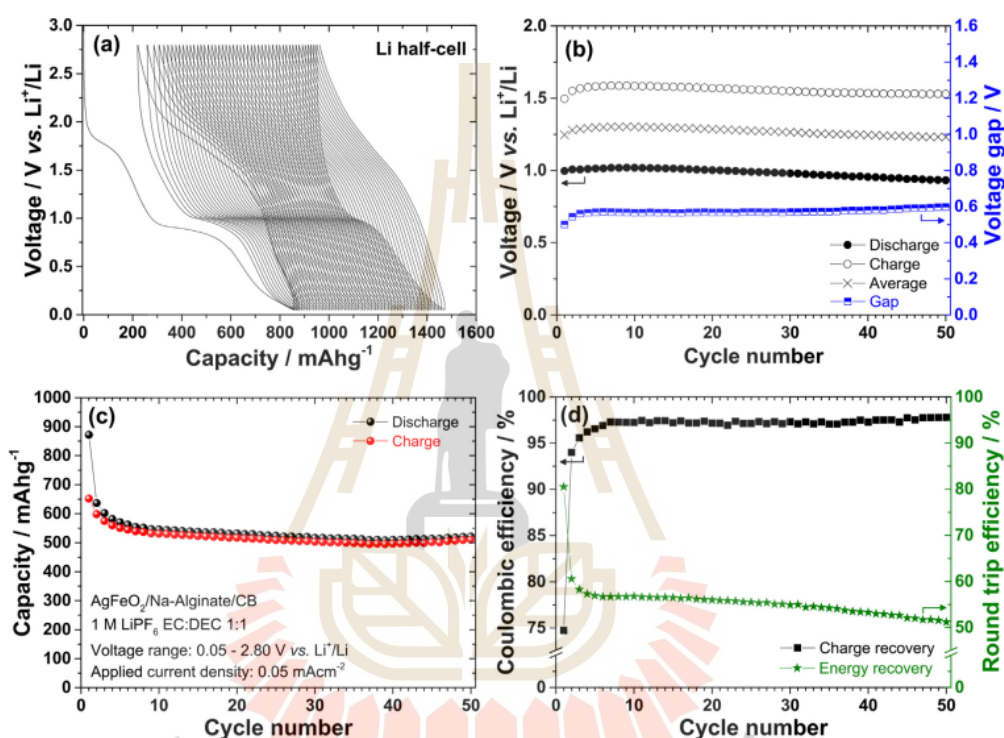


Figure 2.7 (a) Discharge/charge profile of galvanostatic of a Li half-cell that uses a composite AgFeO_2 as the electrode material. (b) The average values evolution of charge and discharge potentials per cycle of Li half-cell. (c) The charge/discharge capacities of cycle performance. (d) Round-trip and coulombic efficiencies of Li half-cell (Adapted from (Berastegui, Tai, and Valvo, 2018)).

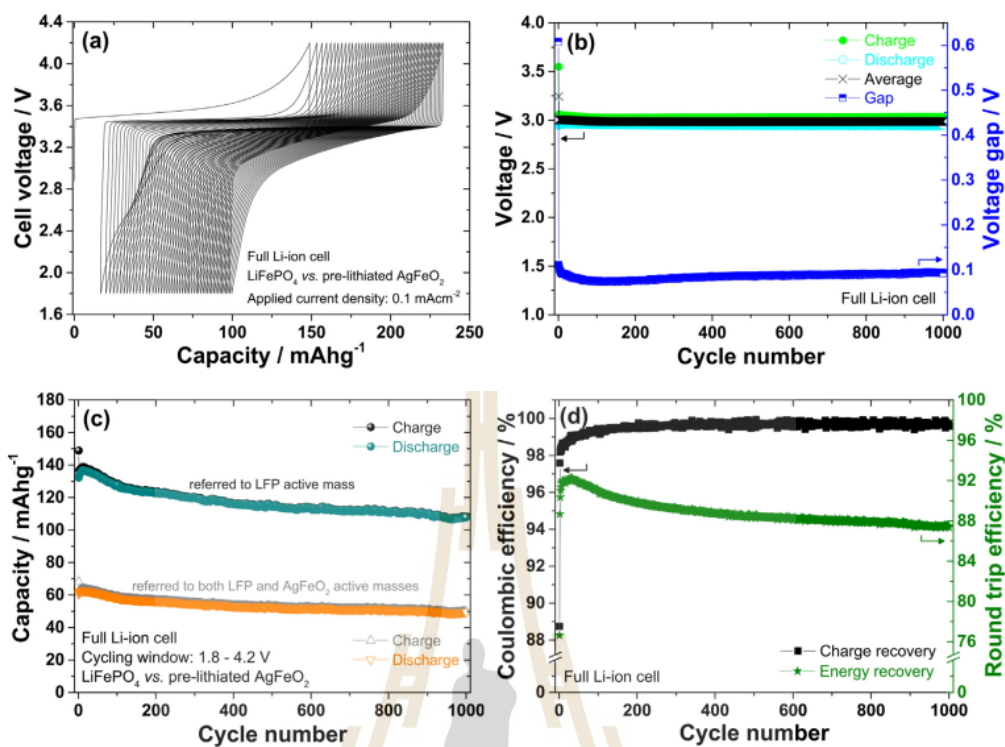


Figure 2.8 (a) Charge/discharge profiles of galvanostatic of a full Li-ion cell. (b) The average values evolution of discharge and charge potentials of Li full-cell. (c) The charge/discharge capacities of cycle performance. (d) Round-trip and coulombic efficiencies of Li full-cell (Adapted from (Berastegui, Tai, and Valvo, 2018)).

Moreover, in 2021, Abhay et al. studied the electrochemical properties of AgFeO₂ as a pseudo-capacitive electrode in an electrolyte of neutral aqueous Na₂SO₄. In this work, the electrochemical properties of AgFeO₂ materials are performed with the three electrodes system in the electrolyte of 1M Na₂SO₄ under the potential window between -0.9 to 0.1 V. At 1 A/g current density (Figure 10). The AgFeO₂ flower-like microarchitectures exhibit good electrochemical performance with a specific capacitance of 110.4 F/g and a capacitance retention of 89% after 2000 times. Moreover, the behavior of full cell of AgFeO₂ material at the calcined temperature of 400°C (AFO-400//AC) exhibited good electrochemical performance (Figure 11) (Siedliska, Pikula, Chocyk, and Jartych, 2017; Singh, Mondal, Rath, and Singh, 2021)

that provided a high-power density value of 454.3 W/kg with a high value of energy density of 33.5 Wh/g with good cycling stability.

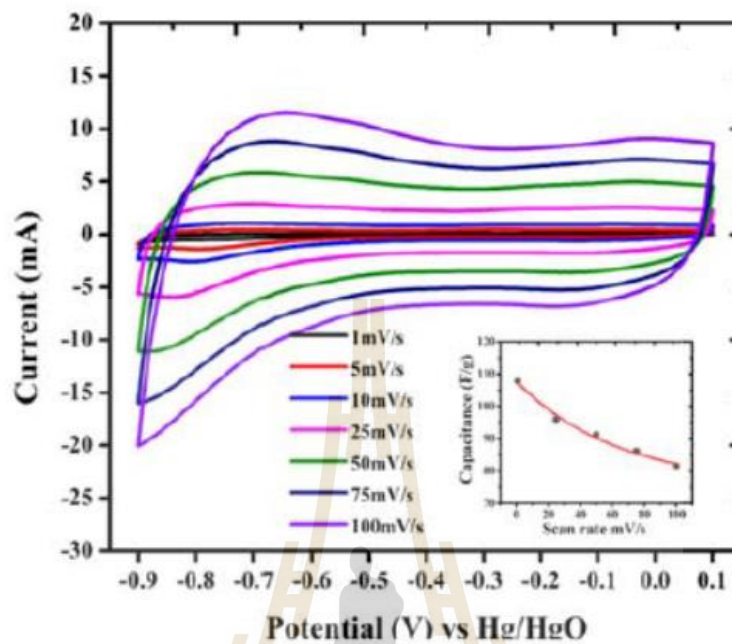


Figure 2.9 CV curves at different scan rates of 1 mV/s to 100 mV/s of AgFeO_2 nanoparticles at the calcination temperature of 400°C (Adapted from (Singh et al., 2021)).

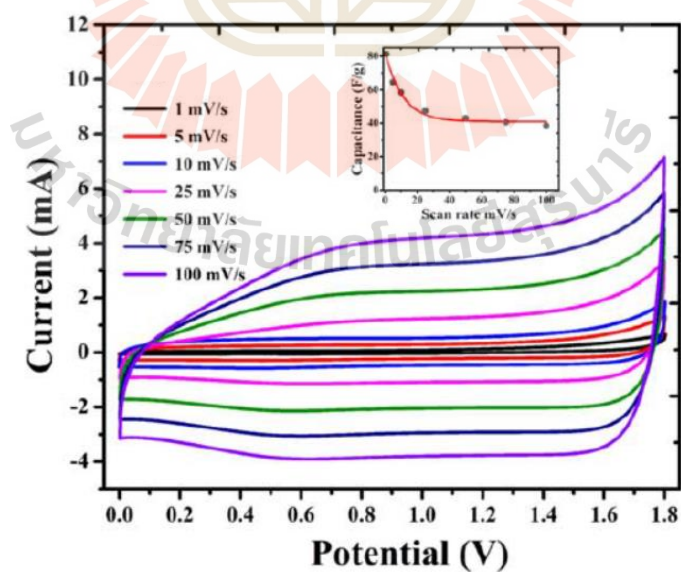


Figure 2.10 Cyclic voltammetry (CV) curves of $\text{AgFeO}_2\text{-400/AC}$ as a function of scan rates (Adapted from (Singh et al., 2021)).

CHAPTER III

RESEARCH METHODOLOGY

The experimental procedure is described in this chapter, comprising of three main sections. Initially, the materials used are provided. Subsequently, the process of AgFeO₂-based nanostructures preparation is described. Lastly, the method employed for materials characterization is also elucidated.

3.1 Raw materials

- Iron (III) Nitrate nanohydrate Fe(NO₃)₂·9H₂O, Mw = 404, 99.9%, Sigma- Aldrich
- Silver Nitrate AgNO₃, Mw = 169.87, 99.9%, Sigma-Aldrich
- Cobalt (II) nitrate hexahydrate Co(NO₃)₂·6H₂O, Mw = 348.11, 99.9%, Sigma-Aldrich
- Nickel (II) nitrate hexahydrate Ni(NO₃)₂·6H₂O, Mw = 290.79, 99.9%, Sigma-Aldrich
- Sodium hydroxide NaOH, Mw = 40.00, 99.9%, Sigma-Aldrich
- Potassium hydroxide (KOH), Mw = 56.11, 99.9%, Sigma-Aldrich
- NMP (N-methyl-2 pyrrolidinone), Sigma-Aldrich
- Acetylene black
- Polyvinylidene difluoride (PVDF), Sigma-Aldrich

3.2 Co-precipitation method and synthesis of AgFeO₂-based nanoparticles

In general, many synthetic methods including so-gel, solid- state reaction, hydrothermal, and co-precipitation have been employed to synthesize

nanostructures materials. The co-precipitation method stands out among these routes due to its ability to achieve high levels of crystallinity and purity. It also offers excellent control over composition and morphology, as well as narrow range of particle sizes. The co-precipitation method offers several advantages and disadvantages when compared to other commonly used synthesis method such as hydrothermal, solid-state reaction and so-gel methods. The comparison is given in Table 3.1.

Table 3.1 The advantages and disadvantages comparison of co-precipitation with other methods.

Methods	Advantages	Disadvantages
Co-precipitation	<ul style="list-style-type: none"> — Simple and low-cost — Ambient temperature and pressure — Better homogeneity and mixing of precursor ion 	<ul style="list-style-type: none"> — Less control over crystal structure
Hydrothermal	<ul style="list-style-type: none"> — Better crystallinity control over particles size 	<ul style="list-style-type: none"> — High pressure reactor and specific temperature condition
Solid-state reaction	<ul style="list-style-type: none"> — More stable for reactions involving thermally stable compounds 	<ul style="list-style-type: none"> — High temperature and long reaction time
So-gel	<ul style="list-style-type: none"> — More appropriate for thin film, coating, and complicated structure synthesis — Better control over the position and purity of the synthesized materials 	<ul style="list-style-type: none"> — Less control over particles morphologies — Several drying and heat treatment steps

In this study, the pure AgFeO_2 and $\text{AgFe}_{1-x}\text{M}_x\text{O}_2$ ($\text{M}=\text{Co}, \text{Ni}; x = 0.05, 0.10, 0.15, \text{ and } 0.20$) nanoparticles are prepared via the co-precipitation route. The raw materials for sample preparation consist of silver nitrate (AgNO_3), iron nitrate nonahydrate ($\text{Fe}(\text{NO}_3)_3 \cdot 9\text{H}_2\text{O}$), Cobalt (II) nitrate hexahydrate ($\text{Co}(\text{NO}_3)_2 \cdot 6\text{H}_2\text{O}$) and Nickel (II) nitrate hexahydrate ($\text{Ni}(\text{NO}_3)_2 \cdot 6\text{H}_2\text{O}$). To initiate the synthesis, calculated amounts of starting materials were dissolved in DI water using the magnetic stirrer until a homogeneous solution was achieved which is a summary of the calculated amount of the chemical composition used for the synthesis of pure AgFeO_2 and $\text{AgFe}_{1-x}\text{M}_x\text{O}_2$ nanoparticles are provided in Table 3.2. Subsequently, 1 M of NaOH was gradually added by dropping until the pH reached approximately 11. The resulting substance was gathered through sedimentation, and it was washed several times by DI water to eliminate any remaining impurities such as sodium ions and nitrate ions until the $\text{pH} \sim 7$. Afterwards, the washed precipitate was dried overnight at 70°C . Then, dried precursors were brought to calcine at various temperatures of 100, 200, 300, 400, and 500°C for 6 h in the presence of air utilizing a muffle furnace to obtain pure AgFeO_2 nanoparticles while the $\text{AgFe}_{1-x}\text{M}_x\text{O}_2$ ($\text{M}=\text{Co}, \text{Ni}; x = 0.05, 0.10, 0.15, \text{ and } 0.20$) nanoparticles were synthesized by annealing the precursors at 100°C . Figure 3.2 illustrates the schematic diagram depicting the process of synthesizing AgFeO_2 -based nanoparticles.

Table 3.2 Expression of the calculated amounts of starting materials employed for the production of AgFeO₂-based nanoparticles.

Materials	Samples	Raw materials			
		AgNO ₃ (g)	Fe(NO ₃) ₃ ·9H ₂ O (g)	Ni(NO ₃) ₂ ·6H ₂ O (g)	Co(NO ₃) ₂ ·6H ₂ O (g)
AgFe _{1-x} Ni _x O ₂	x = 0.00	1.699	4.040	-	-
	x = 0.05	1.699	3.838	0.145	-
	x = 0.10	1.699	3.636	0.291	-
	X=0.15	1.699	3.434	0.436	-
	x = 0.20	1.699	3.232	0.582	-
AgFe _{1-x} Co _x O ₂	x = 0.00	1.699	4.040	-	-
	x = 0.05	1.699	3.838	-	0.146
	x = 0.10	1.699	3.636	-	0.291
	x = 0.15	1.699	3.434	-	0.437
	x = 0.20	1.699	3.232	-	0.582



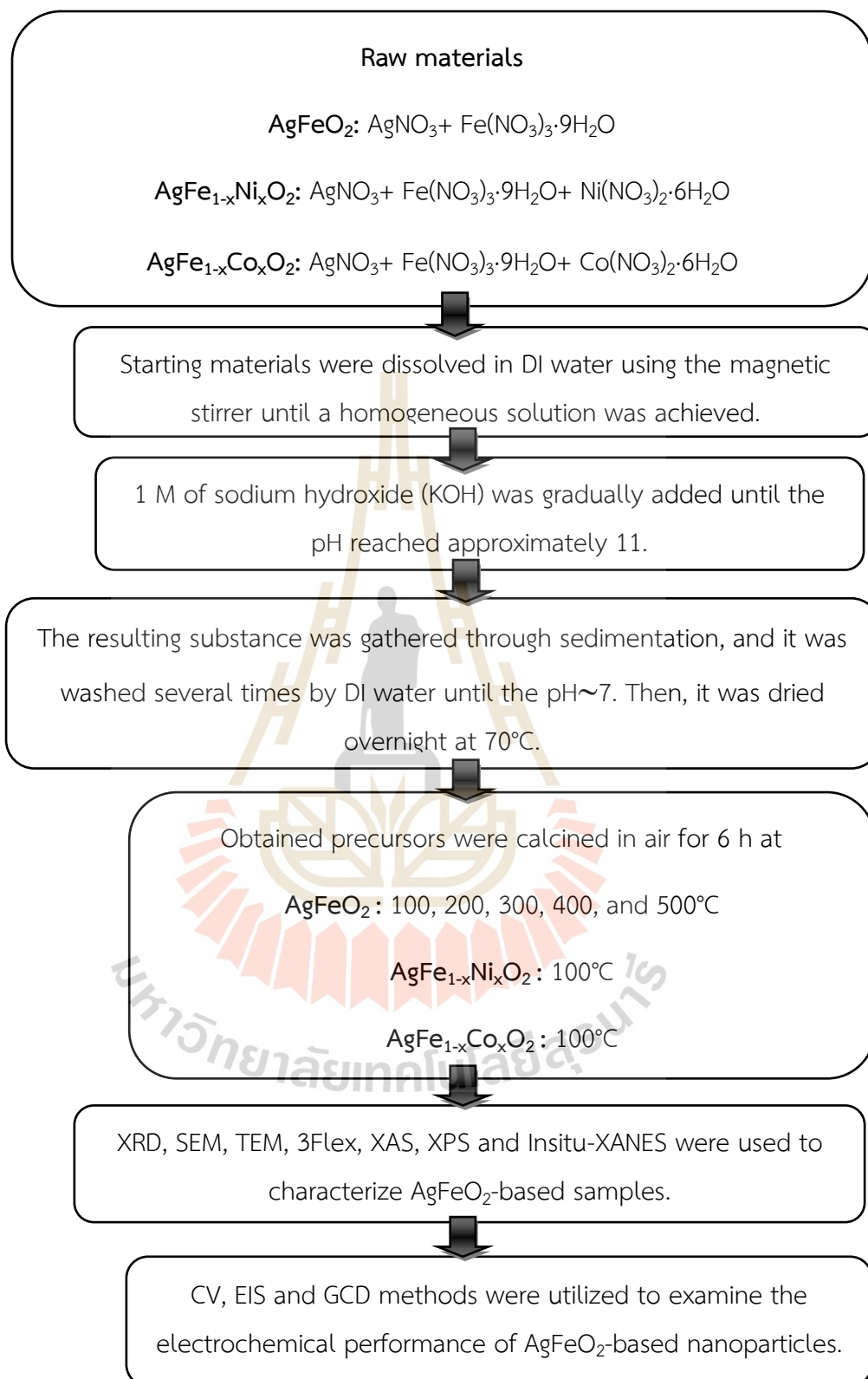


Figure 3.1 A diagram of the synthesis process and the characterisation of AgFeO_2 -based nanoparticles.

3.3 Material characterization technique

3.3.1 X-ray diffraction technique (XRD)

X-ray diffraction (XRD) is a technique for determining the molecular structure and atomic of a crystalline material. XRD works by shining a beam of X-ray onto a crystal and measuring the angles and intensities of the diffracted X-ray that are scattered by the atoms in the crystal lattice. The architectural diagram in Figure 3.1 depicts the geometric aspects of diffraction. This information can then be used to determine the positions and types of atoms in the crystal, as well as the distances between them. The principle of XRD can be described using several equations. The first is Bragg's law, which communicates the angle of diffraction (θ) to the spacing of crystal lattice planes (d) and the wavelength of the X-ray (λ) can be expressed using equation:

$$n\lambda = 2d\sin(\theta) \quad (3.1)$$

where n is an integer representing the diffraction order. This equation explains why certain angles of diffraction produce particularly strong diffraction X-ray, as these angles correspond to constructive interference between the X-ray scattered by different planes in the crystal lattice. Another important equation in XRD is the Scherrer equation, which relates the full width at half maximum (FWHM) of a diffraction peak to the size (D) of the crystalline domains in the material can be written in the relation as follow.

$$\text{FWHM} = \frac{K\lambda}{D\cos(\theta)} \quad (3.2)$$

where K is a constant that bases on the shape of the diffracting crystal and the degree of strain in the material. This equation could be applied to estimate the size of the crystalline domains in a material by using the FWHM of a diffraction peak.

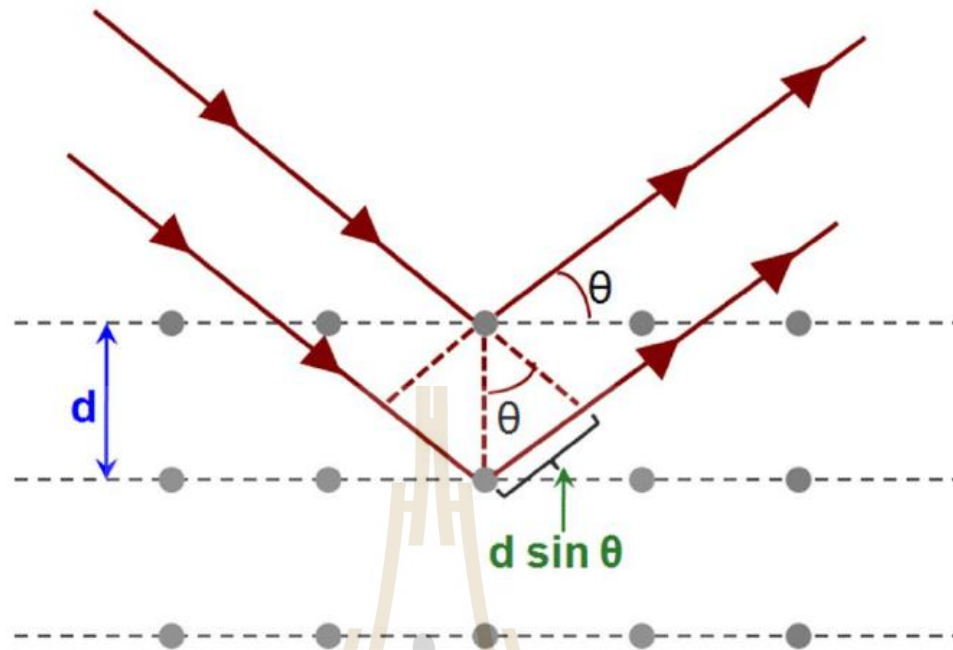


Figure 3.2 The schematic illustration of Bragg's law interpretation (Adapted from (Baskaran, 2010)).

Moreover, the equation used to calculate the d-spacing (d) is based on the relationship between the Miller indices of the diffraction plane (hkl) and the lattice parameter. For the hexagonal structure, it can be given by equation.

$$\frac{1}{d^2} = \frac{4}{3} \left(\frac{h^2 + hk + k^2}{a^2} \right) + \frac{l^2}{c^2} \quad (3.3)$$

The equation relating the d-spacing to the lattice parameters in a rhombohedral structure is as follows.

$$\frac{1}{d^2} = \frac{4(h^2 + k^2 + l^2)\sin^2\alpha + 2(hk + kl + hk)(\cos^2\alpha - \cos\alpha)}{a^2(1 - 3\cos^2\alpha + \cos^3\alpha)} \quad (3.4)$$

In this study, a D8 Advance Bruker instrument with Cu $K\alpha$ radiation and a wavelength of 0.15406 nm was employed to evaluate the structure of AgFeO₂-based nanostructures. During the measurement, the samples were positioned on silicon glass. The pattern of X-ray diffraction (XRD) was recorded in the 2θ range of 10° to 90° using a step size of 0.4 and a step time of 1. For the identification of the

crystalline material, XRD pattern was compared with the reference pattern provided by the Joint Committee for Power Diffraction Standard (JCPDS).

3.3.2 Scanning electron microscopy (SEM)

SEM technique is a widely used imaging method in materials science and other fields for observing the surface structure and morphology of a sample. The SEM works by scanning a focused beam of electron across the surface of a sample and detecting the backscattered electrons, secondary electrons, and X-rays that are emitted from the sample surface. These signals can then be used to construct an image of the sample with high spatial resolution and depth of field. The diagram of the working principle for SEM technique is displayed in Figure 3.2.

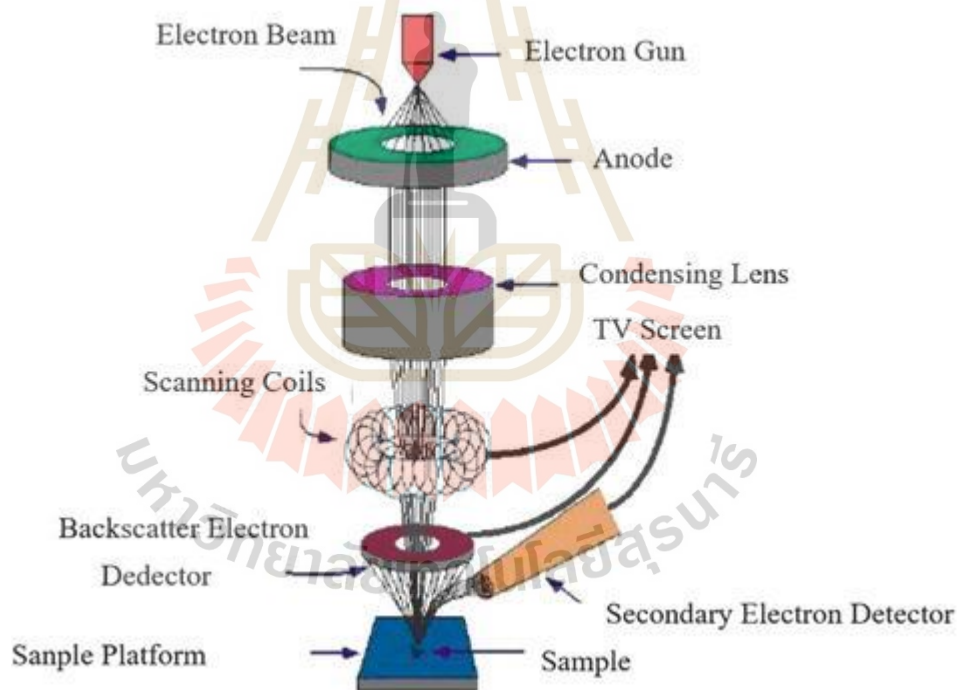


Figure 3.3 Representing the SEM components (Adapted from (Temiz, Yilmaz, and Kolemen, 2022)).

The principles of SEM can be described using several equations. The first is the Schrödinger equation, which explains the behavior of electrons in the presence of a potential energy field:

$$i\hbar \frac{\partial \Psi}{\partial t} = H\Psi \quad (3.5)$$

where \hbar is the reduced Planck constant, t is time, Ψ is the wavefunction of the electron, and H is the Hamiltonian operator describing the potential energy field. Another important equation in SEM is the secondary electron yield equation, which relates the number of secondary electrons emitted from the sample surface (I) to the primary electron beam current (i) and the secondary electron yield (δ):

$$I = i\delta \quad (3.6)$$

This equation explains why secondary electron emission is an important signal in SEM imaging, as it is directly proportional to the beam current of primary electron and the secondary electron yield of the sample surface. The backscattered electron yield equation is another important equation in SEM, which relates the number of backscattered electrons (I) to the primary electron beam current (i), the atomic number of the sample ($f(\theta)$), and the angle of incidence of the primary electron beam (θ).

$$I = iz^2f(\theta) \quad (3.7)$$

where $f(\theta)$ is the angle of incidence function that depends on the atomic scattering factors of the sample. This equation explains why backscattered electron imaging is particularly useful for imaging materials with high atomic number, as the backscattered electron yield is proportional to z^2 .

In this work, the samples were attached to a sub using tape of carbon and covered them in a vacuum with gold for a duration of 10 minutes. The morphologies of the prepared AgFeO_2 -based nanostructures was examined using field-emission scanning electron microscopy (FESEM: JEOL, JEM. 700X).

3.3.3 Transmission electron microscopy (TEM)

TEM is a powerful analytical approach used to study the microstructure of materials at the nanoscale. The results obtained from TEM analysis can inform about the crystal structure, composition, and morphology of a material. In simple terms, TEM works by shooting the electrons beam through a thin sample, which interacts with the sample and is then projected onto a screen or detector. The components of TEM consist of several important parts such as electron source, electron lenses, condenser lens, sample holder, specimen, Object lens, Imaging system, vacuum system, Electron energy filter (optional) and computer and control system which displayed in Figure 3.3. The source of electron in a TEM is usually a field emission gun (FEG) or a heated filament. It emits a beam of electrons, which is accelerated to high energies. The electron beam is focused and controlled by a set of electromagnetic lenses. These lenses are responsible for forming a highly focused and coherent electron beam. The condenser lens is the first lens that the electron beam encounters after leaving the electron source. It focuses the beam onto the sample, adjusting its convergence and illumination. The sample holder, also known as the specimen stage, is a platform where the specimen to be analyzed is mounted. It allows for precise positioning and movement of the sample during imaging. The specimen is the material or sample being studied in the TEM. It is typically prepared as an ultrathin section, often less than 100 nanometers thick, to allow electrons to pass through. The objective lens are the main lens in the TEM and is responsible for forming a magnified image of the specimen. It focuses the transmitted electrons onto the imaging system. The imaging system consists of a combination of lenses, apertures, and detectors that capture and magnify the electron beam transmitted through the specimen. It includes the intermediate lens, projector lens, and various detectors such as scintillators or CCD cameras. TEM operates under high vacuum conditions to prevent electron scattering and interactions with air molecules. A vacuum system is employed to create and maintain a suitable environment for the electron beam to travel through. Some advanced TEM setups may include an electron energy filter, which allows for selective energy filtering of the electron beam. This enables spectroscopic analysis and imaging at specific electron energy

ranges. 10 Computer and Control System: TEM instruments are typically connected to a computer and control system that enables the user to manipulate and adjust various parameters, control the microscope, and acquire images. The resulting image shows a highly magnified view of the sample's internal structure, revealing details that cannot be seen with other types of microscopies. TEM analysis can provide information about the materials crystal structures using electron diffraction patterns. These patterns are generated by the interaction of electrons with the crystal lattice of the material and can be employed to determine the orientation and symmetry of the crystal structure. TEM can also be utilized to identify the chemical composition of a material by employing energy dispersive X-ray spectroscopy (EDS). This technique measures X-rays emitted by the sample when it is bombarded with electrons, allowing the identification of the elements present in the material. Overall, TEM can be used to examine the morphology of a material by producing high resolution images of its surface and internal structure. This allows researchers to study the arrangement of atoms and molecules within a material, providing insights into its properties and behavior.



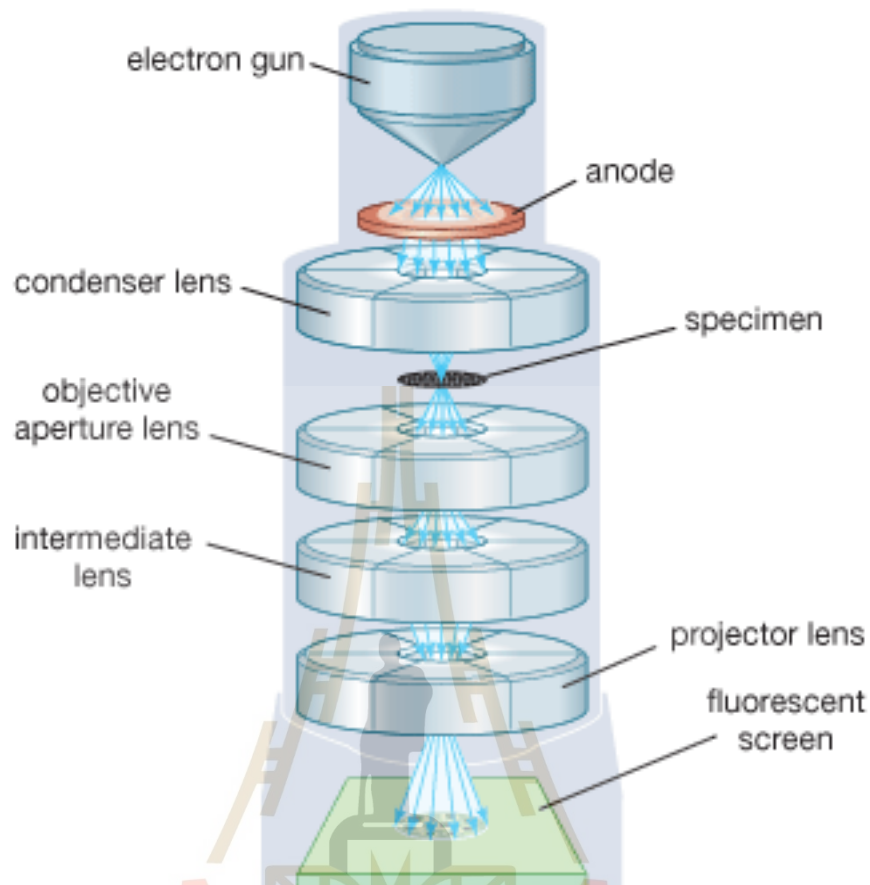


Figure 3.4 Schematic diagram of TEM components (Adapted from (Encyclopaedia Britannica, 2008)).

3.3.4 Nitrogen (N_2) adsorption technique

Nitrogen adsorption is a technique commonly used in materials science and surface chemistry to characterize the surface area and porosity of materials. The principle behind this technique is dependent on the principle of nitrogen gas adsorption onto the material's surface, which allows the determination of the distribution of pore size, pore volume, and surface area. Based on the International Union of Pure and Applied Chemistry (IUPAC), there are six types of adsorption isotherms that can be classified. Adsorption isotherms describe the relationship between the concentration of a substance and its adsorption onto a solid surface at a constant temperature (Figure 3.4).

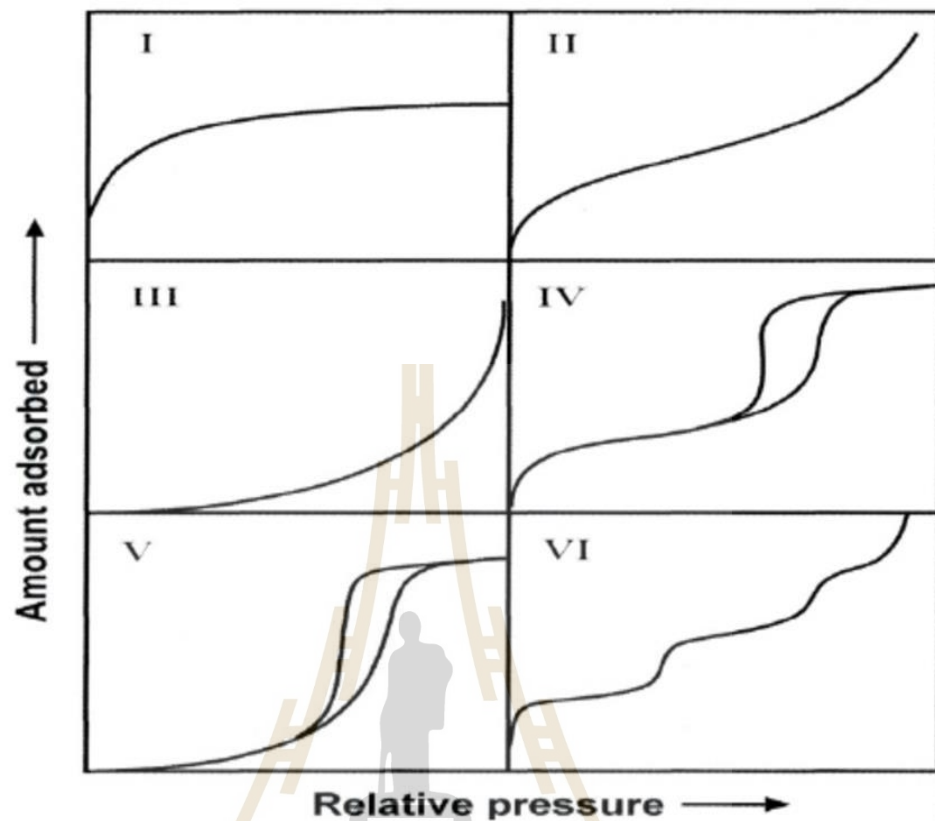


Figure 3.5 Classification of adsorption isotherm (Adapted from (Zeid A Allothman, 2012)).

As shown in Figure 3.4, in Type I, the materials that show the small external surface area with a diameter of pore of smaller than 2 nm are known as microporous materials. For Type II, it represents non-porous materials. Type III is typically associated with non-porous materials or microporous materials, which displays a pore diameter greater than 50 nm. The materials with pore diameter ranging from 2 to 50 nm are observed in mesoporous materials (Type IV). Type V isotherms are indicative of mesoporous and microporous materials due to their weak interaction of the adsorbate/adsorbent. Lastly, Type VI is an isotherm commonly observed in non-porous materials.

3.3.4.1 Brunauer-Emmett-Teller method (BET)

The most common method for nitrogen adsorption analysis is known as the Brunauer-Emmett-Teller (BET) method. The BET method is dependent on the theory developed by Brunauer, Emmett, and Teller in 1938, which assumes that the adsorption of nitrogen follows a multilayer adsorption model on a homogeneous surface. The BET theory relates the amount of gas adsorption at different pressures to the material's specific surface area. The equation applied in BET theory is as follows:

$$\frac{1}{W\left(\frac{P_0}{P}-1\right)} = \frac{P}{P_0} \left(\frac{C-1}{W_m C}\right) + \frac{1}{W_m C} \quad (3.8)$$

where W is a volume of gas adsorbed at a constant pressure and temperature of 1.013×10^5 Pa and 273.15 K, respectively, P_0 is the saturation pressure of the adsorbate gas, W_m is the volume of gas adsorbed for a monolayer on the material surface and C is a constant related to the energetic of adsorption. To estimate the specific surface area using the BET theory, the experimental data obtained from the nitrogen adsorption isotherm is plotted on a graph of $\frac{1}{W\left(\frac{P_0}{P}-1\right)}$ versus $\frac{P}{P_0}$. The linear region of this plot corresponds to the monolayer adsorption, and the slope and intercept of the linear portion could be employed to calculate the specific surface area. The specific surface area (S_{BET}) can be determined using the following equation:

$$S_{BET} = \frac{W_m N A_{cs}}{m V_0} \quad (3.9)$$

where N is 6.023×10^{23} (Avogadro's number), W_m is the volume of monolayer, V_0 is $22414 \text{ cm}^3/\text{molar}$ at atmospheric pressure (the volume of gas per molar), A_{cs} is the molecule cross-sectional area of the adsorption gas (nitrogen, $A_{cs} = 16.2 \text{ \AA}^2$) and m is the mass of the sample.

3.3.4.2 Pore size distribution

The pore size distribution of a material can be determined from the branch of desorption of the adsorption isotherm by using the Kelvin equation or the Barrett-Joyner-Halenda (BJH) method. Based on the change in gas pressure required to desorb from holes of various sizes, these methods can estimate the pore size distribution. Generally, the total pore volume (V_{total}) could be found from the amount of the vapor adsorbed which can be expressed using equation as follow:

$$V_{total} = \frac{P_a V_{ads} V_m}{RT} \quad (3.10)$$

where R is gas constant (8.314 J/K.mol), T is the surrounding temperature, V_m is the molar volume of the liquid substance being adsorbed, P_a is the surrounding pressure and V_{ads} is the volume of gas that has been adsorbed. By using the total pore volume (V_{total}), the average pore size (r_p) can be written as follows:

$$r_p = \frac{V_{total}}{S_{total}} \quad (3.11)$$

In this work, the specific surface area, pore size distribution and total pore volume of the sample were determined using Micrometric 3Flex Adsorption Analyzer which analyzes by BJH and BET methods, respectively. In the testing process, the synthesized AgFeO₂-based nanostructures were subjected to degassing at 120 °C for 10 h under a pressure of 10⁻⁵ Pa.

3.3.5 X-ray absorption spectroscopy (XAS)

XAS is an experimental approach used for probing the electronic and structure properties of materials. It gives useful information about a sample's local atomic structure and electronic states. XAS is particularly useful for studying the chemical composition, oxidation states, coordination environments, and electronic bonding in a wide range of materials, including solids and liquids. The basic principle of XAS involves the interaction of X-rays with matter. When a beam of X-rays passes through a sample, the X-rays can be absorbed by the atoms present in the material.

The probability of absorption depends on the energy of the X-rays and the electronic structure of the absorbing atoms. The absorbed X-rays can excite core electrons from their ground states to higher energy levels or ionize them completely. The XAS spectrum is obtained by measuring the intensity of X-rays transmitted through the sample as a function of the X-ray energy. The X-ray absorption near edge structure (XANES) and the extended X-ray absorption fine structure (EXAFS) (Figure 3.5) are the two key aspects of the XAS spectrum. The spectrum XANES shows the element oxidation states information in the sample. In XANES spectroscopy, a sample is irradiated with a beam of X-rays whose energy is gradually increased. The atoms in the sample absorb the X-rays, causing transitions of inner shell electrons to vacant states. The XANES spectrum is obtained by measuring the intensity of the X-rays that are transmitted or scattered as a function of their energy. The EXAFS region, which extends beyond the absorption edge, contains oscillatory features resulting from the X-ray wave interference with the backscattered wave from neighboring atoms. These oscillations provide information about the local atomic environment, such as bond distances, coordination numbers, and disorder.



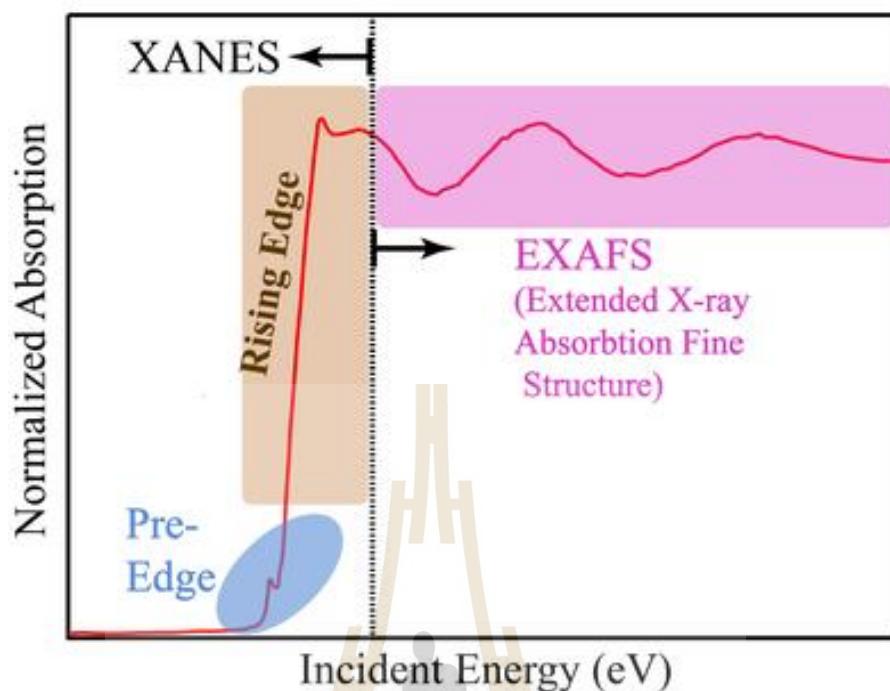


Figure 3.6 Representing the regions of XANES and EXAFS for XAS spectrum (Adapted from Wikipedia).

There are two modes of XAS measurement including transmission and fluorescence mode (figure 3.6). The transmission mode measurement is performed by comparing the X-ray intensity before and after passing through the sample. The absorption of X-ray by the sample based on the energy of the X-ray and the absorption cross-section of the element presents in the material. The absorption cross-section is a measure of the probability of X-ray absorption by an atom as a function of X-ray energy. XAS transmission mode measurement principle can be described using the Beer-Lambert law, which relates the transmitted intensity (I) to the incident intensity (I_0), the sample thickness (x) and the coefficient of absorption (μ) of the material:

$$I = I_0 e^{-\mu x} \quad (3.12)$$

The absorption coefficient depends on the X-ray energy and the properties of the material. By measuring the transmitted intensity at different X-ray energy, one can

obtain the absorption coefficient, which provides insight into the structure of electronic of the material.

For XAS fluorescence mode, the X-ray is used to excite electrons in the material, and the emitted fluorescence radiation is measured. The principle behind XAS fluorescence measurement is that when a core electron in an atom is excited by an incident X-ray photon, it can jump to an unoccupied higher energy level. This creates a core hole in the atom. Subsequently, an electron from higher energy level can drop down to complete the core hole, releasing energy in the form of a fluorescence X-ray photon.

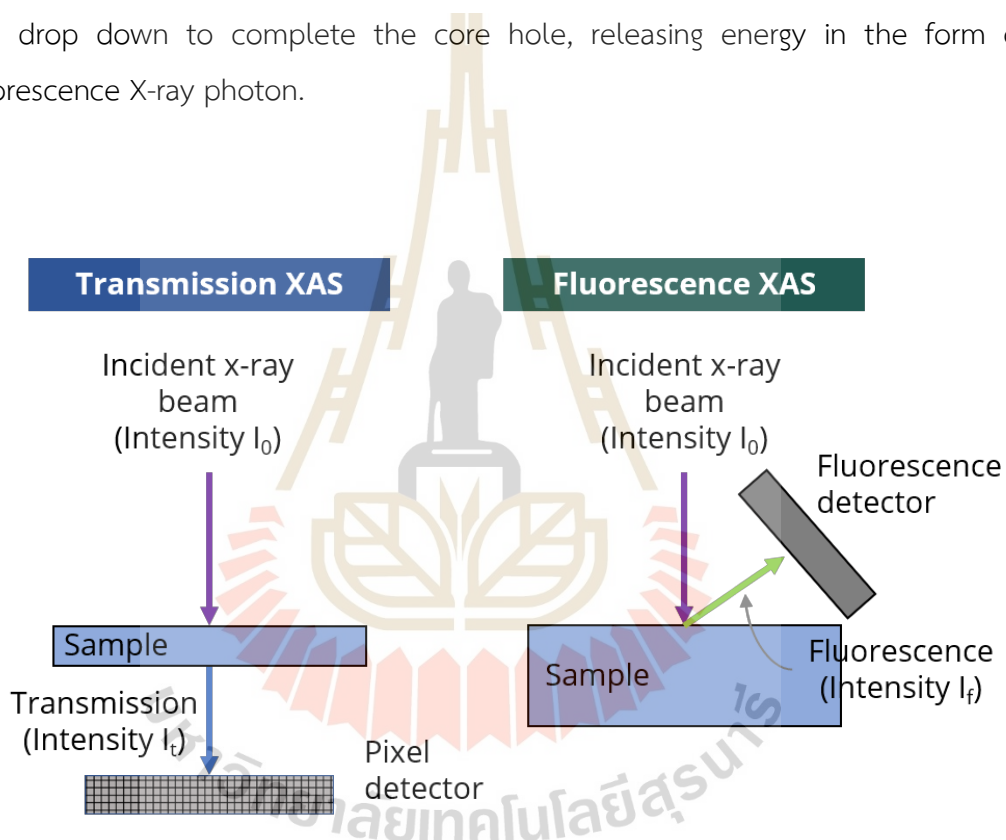


Figure 3.7 The typical mode of XAS measurement (Adapted from Wikipedia).

In this work, XANES spectra of Ag, Fe, Co and Ni were measured at BL 5.2 SUT-NANOTEC-SLRI, XAS of Synchrotron Light Research Institute of Thailand. Athena software was used to analyze the oxidation states of the elements in the samples.

3.3.6 X-ray photoelectron spectroscopy (XPS)

The XPS technique is an employed surface analysis method that provides information about the chemical composition and electronic state of material's surface. It involves bombarding a sample with X-ray and detecting the kinetic energy and intensity of the emitted photoelectrons. XPS basic principle is based on the effect of photoelectric, where X-ray photons are absorbed by atom in the sample (Figure 3.7), resulting in the ejection of core-level electrons. The emitted photoelectrons kinetic energy is directly correlated to the core-level electrons binding energy in the atom. By analyzing the kinetic energies of the emitted photoelectrons, information about atom position, element state and electronic structure of the samples can be obtained.

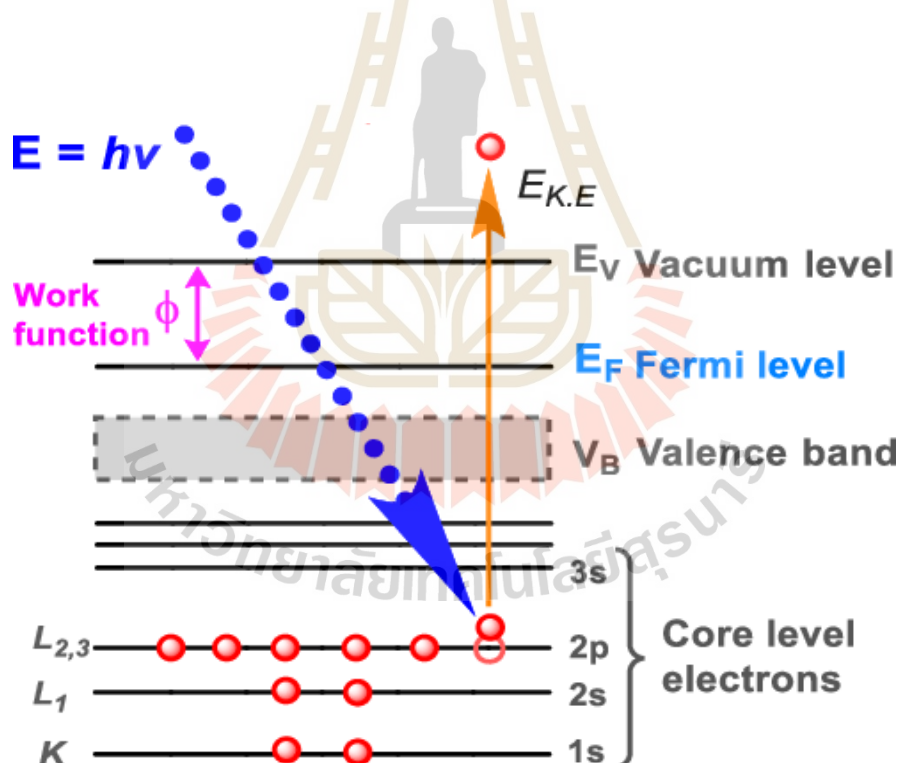


Figure 3.8 Schematic diagram of XPS principle (Adapted from (John Onyango Adongo, 2019)).

The binding energy (E_B) of a core-level electron can be determined using the equation:

$$E_B = h\nu - E_k - \phi \quad (3.13)$$

where $h\nu$ is the energy of incident X-ray photon, E_k is the kinetic energy of the emitted photoelectron and ϕ is the work function. The energy of incident X-ray photon is typically specified in electron volt (eV), and the kinetic energy of the emitted photoelectron is also measured in eV. The binding energy is a characteristic property of each element and its chemical environment, allowing for the identification and qualification of the elements present in the sample. Additionally, the elemental composition of the sample could be achieved from information of the emitted photoelectrons. The related intensities of the photoelectron peaks can be used to investigate the atomic concentrations of the elements present.

In this study, the XPS with an Al $K\alpha$ radiation (1486.6 eV) of ULVAC-PHI (PHI Versa Probe II XPS system) was used to carry out the oxidation states and chemical composition of the prepared AgFeO₂-based nanostructures.

3.4 Electrochemical measurement

Electrochemical measurements refer to the techniques or methods used to study and analyze electrochemical processes. These processes involve the interconversion of chemical and electrical energy such as redox reaction, electrolysis, corrosion and electroplating. Generally, it was utilized to compute the electrochemical performance of the material's electrode or the energy storage devices that associate with the electrochemical process such as supercapacitor and batteries. In the electrochemical measurement, there are several techniques including cyclic voltammetry (CV), electrochemical impedance spectroscopy (EIS) and galvanostatic charge discharge (GCD). For the electrochemical cell setup, a three-electrode system was used to perform the electrochemical properties. The three-electrode system refers to an electrochemical setup that consists of three electrodes: a working electrode, a reference electrode and a counter electrode. The working electrode is the electrode where the electrochemical reaction of interest

take place. The reference electrode provides a stable and known potential against which the potential of the working electrode is measured. It maintains a constant potential and acts as a reference point for the electrochemical measurement. The counter electrode completes the circuit and balance the current flowing through the system. It helps to maintain charge neutrality during the electrochemical process by providing or accepting electrons.

In this work, the AgFeO_2 -based electrode was utilized as the working electrode while the platinum plate and Ag/AgCl are the counter electrode and reference, respectively. The electrochemical performance of $\text{AgFe}_{1-x}\text{M}_x\text{O}_2$ electrode was evaluated by GCD, EIS and CV by Potentionstat/galvanostat in the electrolyte of 3 M KOH. Figure 3.9 shows the electrochemical cell setup for electrochemical measurement of the AgFeO_2 -based nanostructures materials.



Figure 3.9 Electrochemical measurement system includes a three-electrode system, potentionstat/galvanostat and a computer.

3.4.1 Cyclic voltammetry (CV)

Cyclic voltammetry (CV) is an electrochemical technique used to determine the electrode material and examining its electrochemical properties including the specific capacitance. It involves sweeping the voltage applied to an electrochemical cell between two limits and measuring the resulting current. The technique is commonly used for studying energy storage devices such as

supercapacitors. Figure 3.10 represents the CV curve of the EDLC and pseudocapacitor. For pseudocapacitors, the CV curve consists of the anodic and cathodic peaks, which present the oxidation and reduction process, respectively. The capacitance (C) of the supercapacitor can be estimated using the CV curve which relates to the current ($I = \frac{dQ}{dt}$) and the scan rate ($v = \frac{dV}{dt}$). Mathematically, it can be expressed as follows:

$$C \frac{dV}{dt} = \frac{dQ}{dt} \quad (3.14)$$

$$Cv = I \quad (3.15)$$

$$C = \frac{I}{v} \quad (3.16)$$

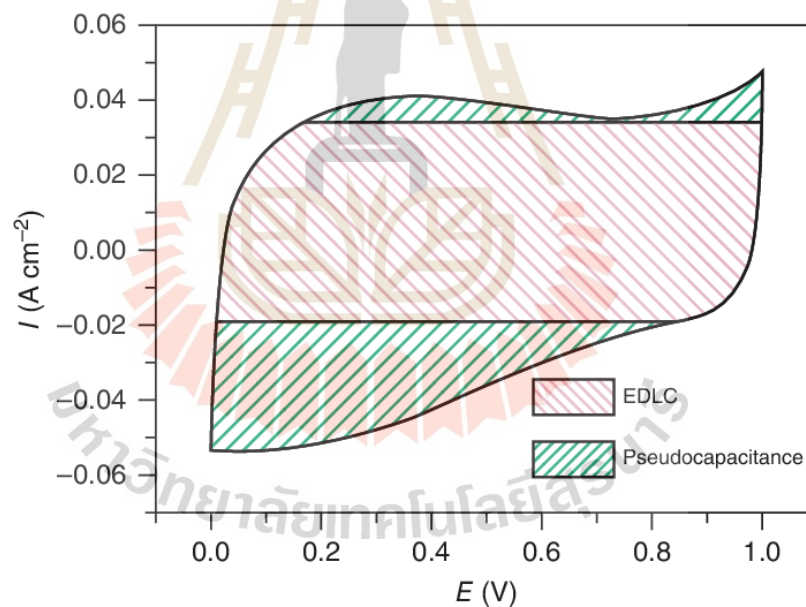


Figure 3.10 CV curve of the ideal EDLC and pseudocapacitor (Adapted from (Sohrabi et al., 2021)).

On the other hands, the electrode material specific capacitance can be estimated from the experimental results using the equation as follow:

$$C_{CV} = \frac{\int I(V)dv}{mv\Delta V} \quad (3.17)$$

where the $\int I(V)dV$ term is the surrounding area of the curve of CV, m represents the mass of active material, ΔV is the window of potential range and ν represents the scan rate.

In this work, the cyclic voltammetry (CV) curve of the AgFeO₂-based nanostructures electrode was performed by using the potentiostat method to study electrochemical properties at 2 mV/s to 100 mV/s scan rates under the potential between -1.16 V to 0.35 V.

3.4.2 Galvanostatic charge discharge (GCD)

Galvanostatic charge-discharge (GCD) technique is a commonly used method to determine the specific capacitance of an electrochemical capacitor or supercapacitor. In this technique, the voltage response is recorded with the charging and discharging at a constant current (Figure 11). By analyzing the voltage-time data, one can calculate the specific capacitance of the capacitor.

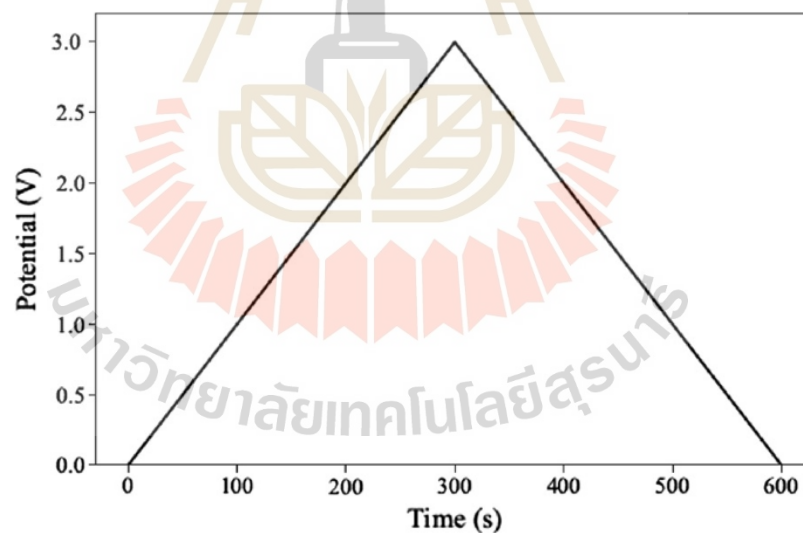


Figure 3.11 GCD curve (Adapted from (Eleri, Lou, and Yu, 2022)).

Furthermore, the specific capacitance (C_s) of the sample relates to the discharge current (I), discharge time (Δt), active material mass (m) and potential window (ΔV) which can be written as follow:

$$C_s = \frac{I\Delta t}{m\Delta V} \quad (3.18)$$

Moreover, the specific energy and power density can be found as follows:

$$E = \frac{CV^2}{2 \times 3.6} \quad (3.19)$$

$$P = \frac{E \times 3600}{t} \quad (3.20)$$

where E represents the specific energy (Wh/Kg) and P represent the specific power (W/Kg).

In this work, the specific capacitance of the materials is performed by GCD at the 1A/g to 20 A/g current densities.

3.4.3 Electrochemical impedance spectroscopy (EIS)

EIS method is employed to study the electrical behavior of electrochemical system. It involves the application of a small perturbation signal to the system and measuring the resulting response in term of impedance. EIS can provide valuable information about the charge transfer processes, electrical properties and the kinetic of electrochemical reactions. The physics equation relates to EIS are derived from the principles of electrical circuit theory and electrochemical processes. The most commonly used model for interpreting EIS data is the equivalent circuit model which interprets the electrical behavior of the system. In AC current, the correlation between the sinusoidal current (I) and voltage (V) and the complex impedance (Z) can be described using Ohm's Law. However, in AC currents, the impedance (Z) is a complex quality that considers both resistance (Z') and reactance (Z''). The relationship can be expressed mathematically as:

$$V = IZ \quad (3.21)$$

where V is the complex voltage, I is a complex current and Z is the complex impedance. Expanding the equation further, we can represent the complex voltage (V) and complex current (I) using their phasor representations. Let's denoted the magnitude of the voltage as V_0 and the phase angle as ϕ_v and the value of the current as I_0 and the phase angle as ϕ_i . Using phasor notation, the equation become:

$$V_0 e^{(j\omega t + \phi_v)} = I_0 e^{(j\omega t + \phi_i)} Z \quad (3.22)$$

where $e^{(j\omega t)}$ represents the time-varying sinusoidal component with angular frequency ωt .

By dividing both sides of the equation by $I_0 e^{(j\omega t + \phi_i)}$, we get:

$$\frac{V_0}{I_0} e^{(\phi_v - \phi_i)} = Z \quad (3.23)$$

The term $\frac{V_0}{I_0}$ represents the magnitude of ratio between the voltage and current phasors, denoted as $\left| \frac{V}{I} \right| = |Z|$. Therefore, the relationship between the sinusoidal current and voltage signals and the complex impedance in AC currents can be expressed as:

$$Z = \left| \frac{V}{I} \right| e^{j(\phi_v - \phi_i)} = |Z| e^{j\phi} \quad (3.24)$$

$$Z = Z' + jZ'' \quad (3.25)$$

where j is the imaginary unit. The magnitude $|Z|$ and angle ϕ can be defined as:

$$|Z| = \sqrt{(Z')^2 + (Z'')^2} \quad (3.26)$$

$$\phi = \arctan\left(\frac{Z''}{Z'}\right) \quad (3.27)$$

In the experiment, EIS is performed over a range of frequencies. The frequency of the applied perturbation signal is denoted as f and it typically expressed in hertz (Hz). By using the frequency (f) and the magnitude impedance ($|Z|$), the capacitance (C) can be expressed as:

$$C = \frac{1}{2\pi f |Z|} \quad (3.28)$$

In EIS technique, there are two plots such as Bode and Nyquist plot. The plot of Nyquist is a common graphical explanation of EIS data. It plots the real part (impedance (Z')) and the imaginary part (impedance (Z'')) and the. The Bode plot is another graphical representation of EIS data. It plots the magnitude of the impedance value ($|Z|$) and the phase angle (ϕ) as a function of the frequency. EIS

provides two types of impedance including Faradaic impedance and non-Faradaic impedance. Faradaic impedance represents the impedance due to charge transfer processes occurring at the electrochemical interface. It can be modeled using the Randles circuit, which consists of a resistor (R_{ct}) in parallel with the constant phase element (CPE) in series with an impedance of Warburg (Z_w) (Figure 3.12a). Non-Faradaic impedance accounts for processes that do not involve charge transfer such as double-layer capacitance and diffusion. It can be modeled using a simple parallel combination of a resistor (R_{Ω}) which is the real part (Z') intercept of Nyquist plots a capacitor (C) (Figure 3.12b).

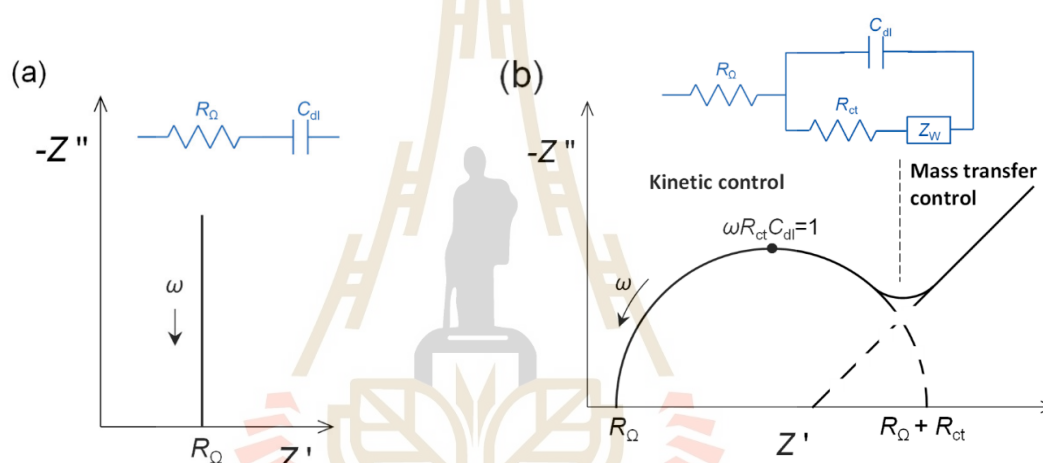


Figure 3.12 The impedance of complex plane plots a) non-Faradaic region and b) Faradaic electron transfer with mass transfer (Adapted from wikipedia).

In this work, the complex electrical resistance of the samples is tested using electrochemical impedance spectroscopy (EIS) after GCD measurement under the frequency range between 100 kHz and 100 mHz in order with 10 mV amplitude.

3.4.4 Preparation of working electrode

The working electrode component has an 80:10:10 wt% ratio of the prepared AgFeO_2 -based nanoparticles as the active materials, with polyvinylidene difluoride (PVDF) as the binder, and acetylene black as the conductive agent, respectively, and employing N-methyl-2 pyrrolidinone (NMP) of 400 μl as a solvent for slurry forming and coating on a surface of $1 \times 1.2 \text{ cm}^2$ of Ni foam plate with 50 μl

of the slurry. The electrode was dried at 70 °C for 12 h to displace the NMP solvent. After drying, the electrode was brought to press at 10 MPa for 5 minutes.



CHAPTER IV

RESULTS AND DISCUSSION

The experiment results are presented in this chapter along with a discussion of them, which consists of three main parts such as AgFeO_2 nanoparticles, $\text{AgFe}_{1-x}\text{Co}_x\text{O}_2$ nanoparticles and $\text{AgFe}_{1-x}\text{Ni}_x\text{O}_2$ nanoparticles. In each part includes the characterization and electrochemical studies. X-ray diffraction (XRD) technique is utilized to determine the crystal structure of all the prepared AgFeO_2 -based samples. The morphologies of AgFeO_2 -based samples are investigated using TEM and SEM. XAS and XPS are applied to examine the composition of elemental and valence states of the prepared $\text{AgFe}_{1-x}\text{M}_x\text{O}_2$ nanoparticles. The BET method is used to compute specific surface area, while the porosity is assessed using the BJH method. Additionally, we demonstrate the effects of calcination at different temperatures and Co and Ni-doped AgFeO_2 through electrochemical results.

4.1 AgFeO_2 nanoparticles

4.1.1 Structure and morphologies analysis of AgFeO_2 nanoparticles by XRD, TEM and SEM

The patterns of XRD of the obtained AgFeO_2 samples which calcined at the various temperatures of 100 , 200 , 300 , 400 , and 500°C are displayed in figure 4.1. The diffraction peaks observed of all the prepared samples identified that the crystal structure of the samples are closely matched with the diffraction pattern of standard of hexagonal α - AgFeO_2 with the mixing of 3R (PDF2 card no. 00-018-1175) and 2H (PDF2 card no. 00-029-1141) phases. The diffraction peaks of 3R phase is found at $2\theta = 14.29, 28.87, 34.37, 35.42, 39.31, 43.87, 48.67, 52.48, 59.68, 61.12, 68.25, \text{ and } 72.48^\circ$ associate with the lattice plane of (003), (006), (101), (102), (104), (109), (107), (108), (0012), (111), (116), and (202), respectively while 2H phase observed at $2\theta =$

14.27, 28.77, 34.82, 37.07, 40.62, 43.78, 50.52, 56.59, 59.64, 60.89, 62.96, 63.25, 68.76, and 72.09° correlate with the lattice plane of (002), (004), (101), (102), (103), (006), (105), (106), (008), (110), (112), (107), (114), and (201), respectively. Interesting, the sample calcined at 500°C has impurity phase, which contained a small amount of Ag. This is may owing to the phase deposition occurred (Siedliska et al., 2017). According to the refinement method, the percentage of 2H and 3R phase at different calcination temperatures can be found as shown in Table 4.1.

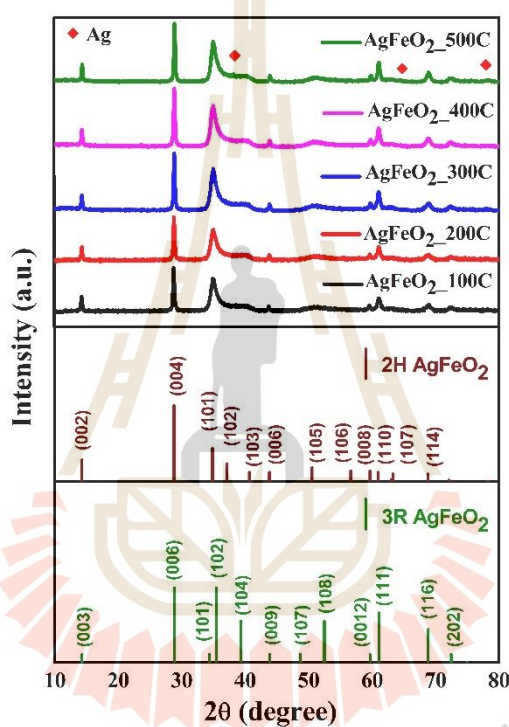


Figure 4.1 The pattern of XRD of AgFeO₂ nanoparticles calcined at various temperatures ranging from 100 to 500°C.

Table 4.1 2H and 3R percentages in AgFeO₂ structure at various calcination temperatures.

Phase type	Calcination temperatures				
	100°C	200°C	300°C	400°C	500°C
2 H	70.06%	69.97%	69.31%	67.28%	65.95%
3R	29.34%	30.03%	30.69%	32.72%	34.05%

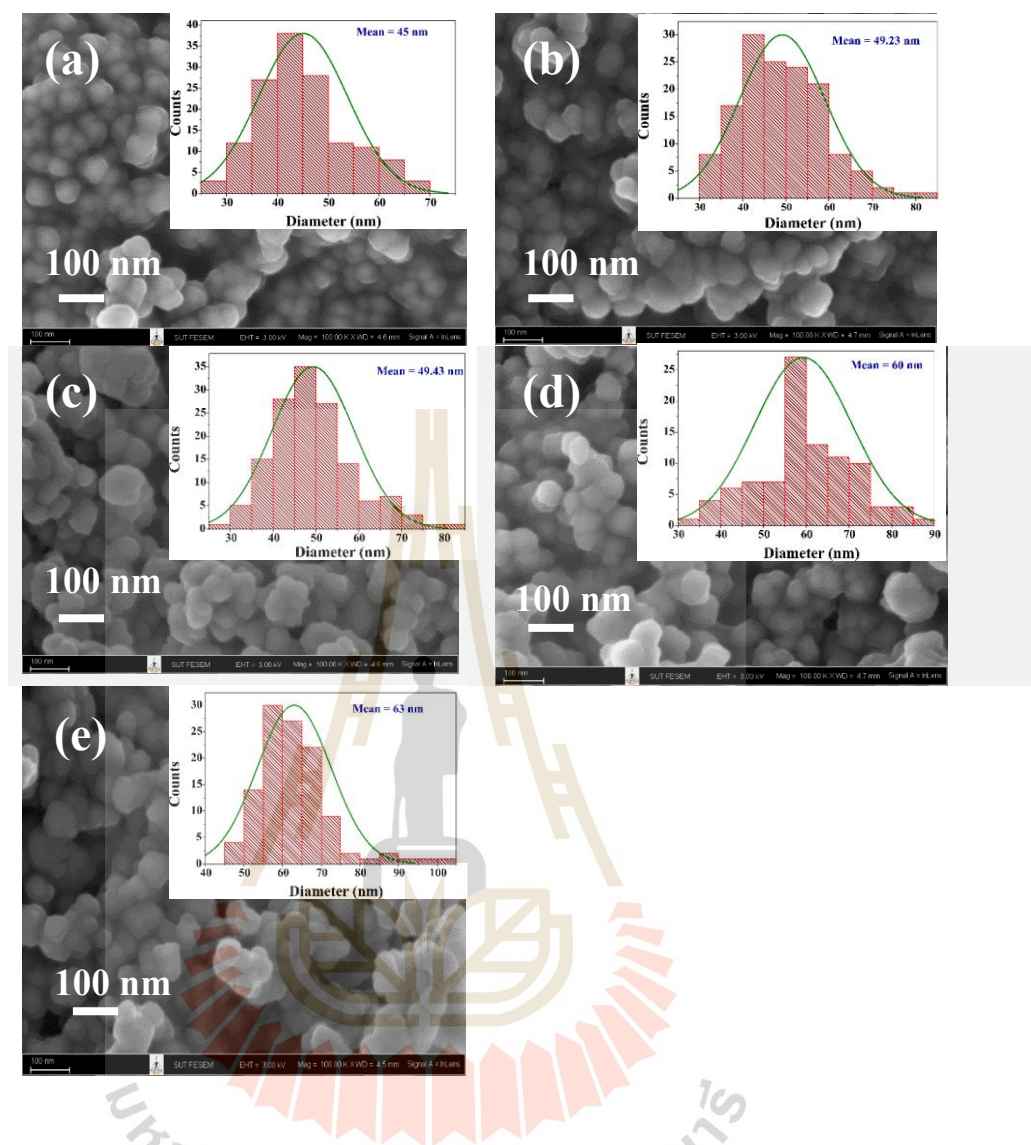


Figure 4.2 FESEM images of the pure AgFeO_2 samples calcined at different temperatures of (a) 100°C, (b) 200°C, (c) 300°C, (d) 400°C, and (e) 500°C.

The FESEM was employed to study the structure and morphologies of delafossite AgFeO_2 samples. Figure 4.2 shows the FESEM images of the AgFeO_2 samples with the different calcined temperatures. The particle size distribution of the prepared AgFeO_2 samples were analyzed by ImageJ software implying the morphologies of AgFeO_2 which the particle sizes of the sample are in the nanoscale. Additionally, the mean particle size values are 45, 49.23, 49.43, 60 and 63 nm were

obtained from the samples at different temperatures of 100, 200, 300, 400, and 500°C, respectively.

Moreover, the structural and morphology were examined by the TEM as depicted in Figure 4.3. The SAED images confirmed the presence of 2H and 3R phases of the prepared AgFeO_2 nanoparticles.

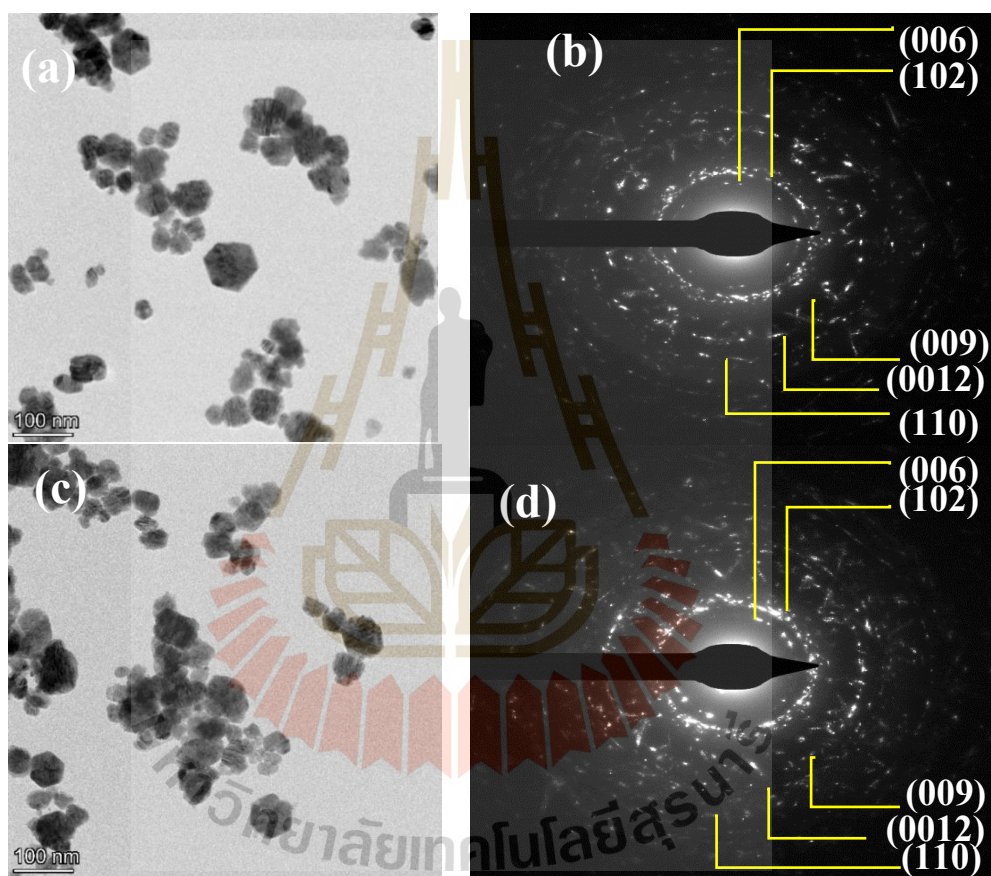


Figure 4.3 The images of TEM with associating SAED of the synthesized AgFeO_2 samples calcined spanning from (a,b) 100°C to (i,j) 500°C, respectively.

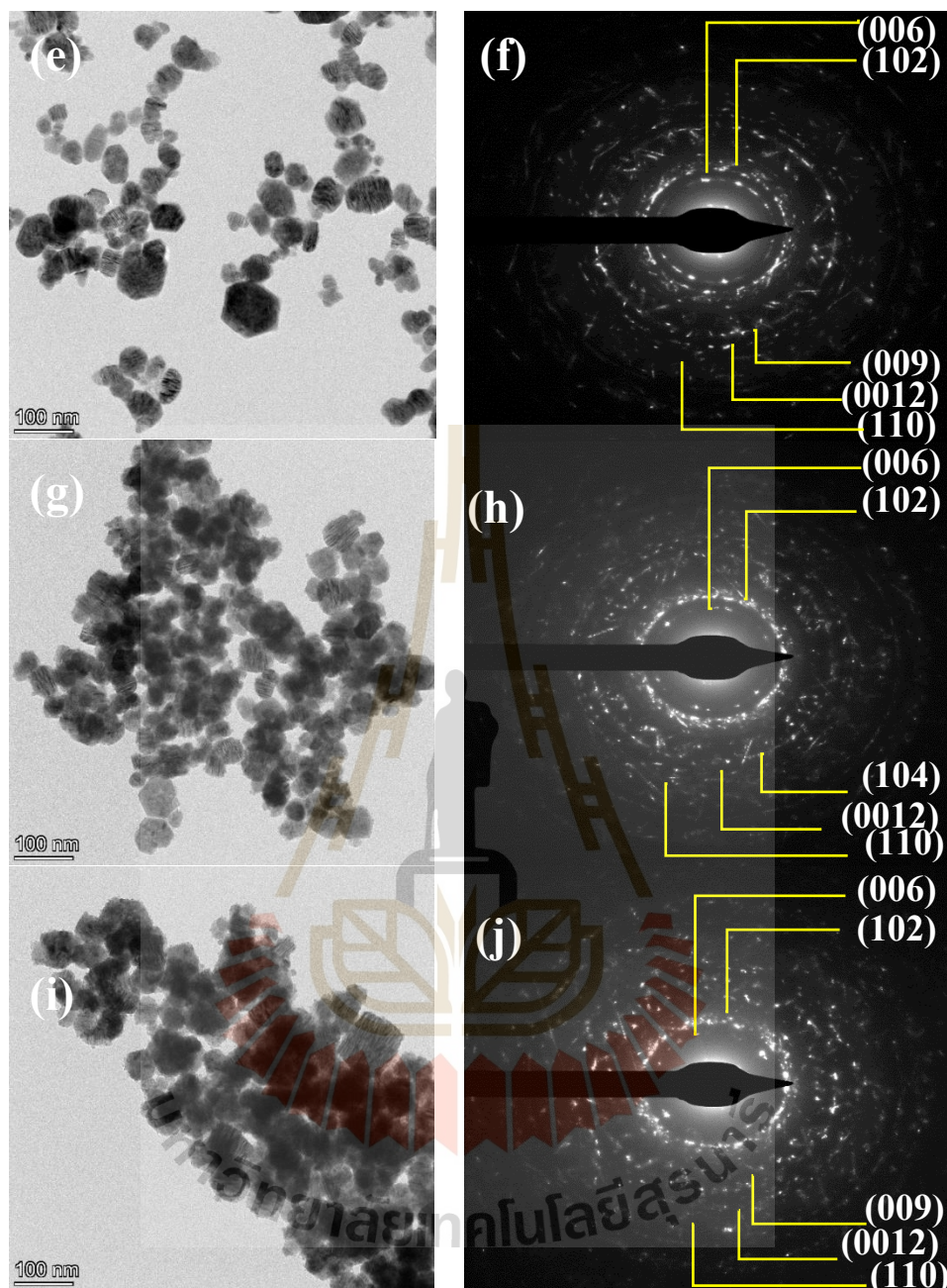


Figure 4.3 (Continued) The images of TEM with associating SAED of the synthesized AgFeO_2 samples calcined spanning from (a,b) 100°C to (l,j) 500°C , respectively.

4.1.2 Oxidation state and surface chemical composition study of AgFeO_2 nanoparticles by XAS and XPS

The Ag and Fe valence states in delafossite AgFeO_2 nanoparticles were studied by the XAS technique. The normalized spectra of XANES of Ag L3-edge of

prepared AgFeO_2 nanoparticles and reference samples of Ag_2O (Ag^{1+}) and AgO (Ag^{2+}) are displayed in Figure 4.4(a). The Ag L3-edge XANES spectra edge position of all the synthesized AgFeO_2 samples are closed to the reference samples of Ag_2O (Ag^{1+}) which are presented using Table 4.1. This indicated that Ag ion in all AgFeO_2 samples had the oxidation states of Ag^{1+} . On the other hands, For the Fe K-edge, the oxidation state increases when the K-edge energy reallocates to higher energy. As interpreted in Figure 4.5(a), the XANES spectra edge position of all prepared AgFeO_2 corresponds to the reference sample of Fe_2O_3 (Fe^{3+}) which indicated that Fe ion in all the samples had the oxidation states of between Fe^{3+} as verified utilizing the edge energy (Table 4.1) and the plot of first derivative (Figure 4.5(b)).

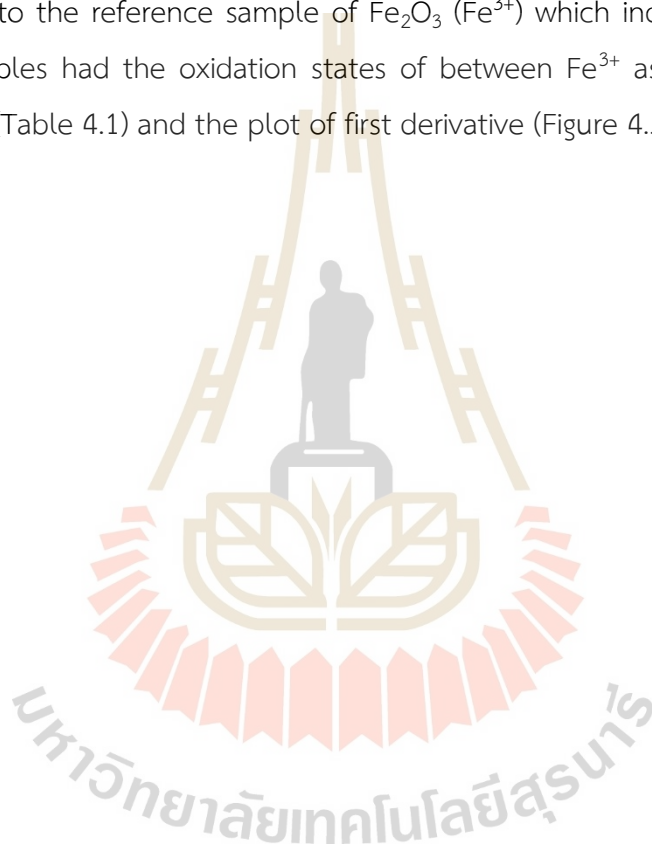


Table 4.2 The oxidation states with corresponding edge energies of the references and prepared AgFeO₂ nanostructures.

Reference Samples	Edge element	Edge energy E (eV)	Oxidation state
Ag ₂ O	Ag	3349.39	+1
AgO	Ag	3348.11	+2
Fe foil	Fe	7111.65	+0
FeO	Fe	7119.89	+2
Fe ₃ O ₄	Fe	7123.23	+2, +3
Fe ₂ O ₃	Fe	7126.76	+3
AgFeO ₂ -100C	Ag	3350.45	+0, +1
	Fe	7126.97	+3
AgFeO ₂ -200C	Ag	3350.02	+0, +1
	Fe	7126.60	+3
AgFeO ₂ -300C	Ag	3350.48	+0, +1
	Fe	7127.18	+3
AgFeO ₂ -400C	Ag	3350.27	+0, +1
	Fe	7126.40	+3
AgFeO ₂ -500C	Ag	3350.49	+0, +1
	Fe	7126.50	+3

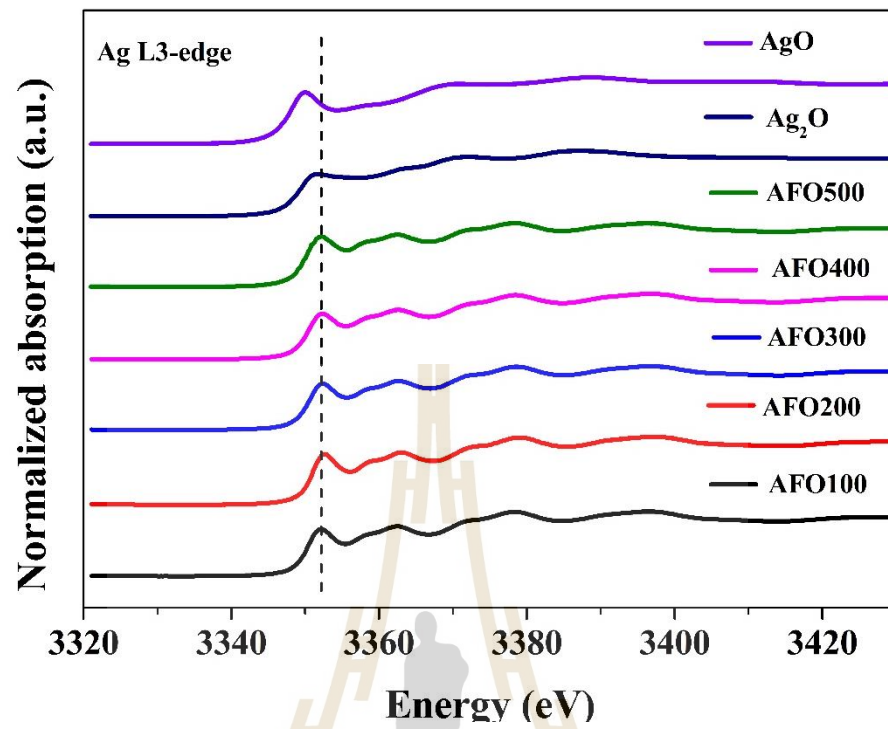


Figure 4.4 Normalized XANES plot of the synthesized AgFeO₂ samples at Ag L3-edge.



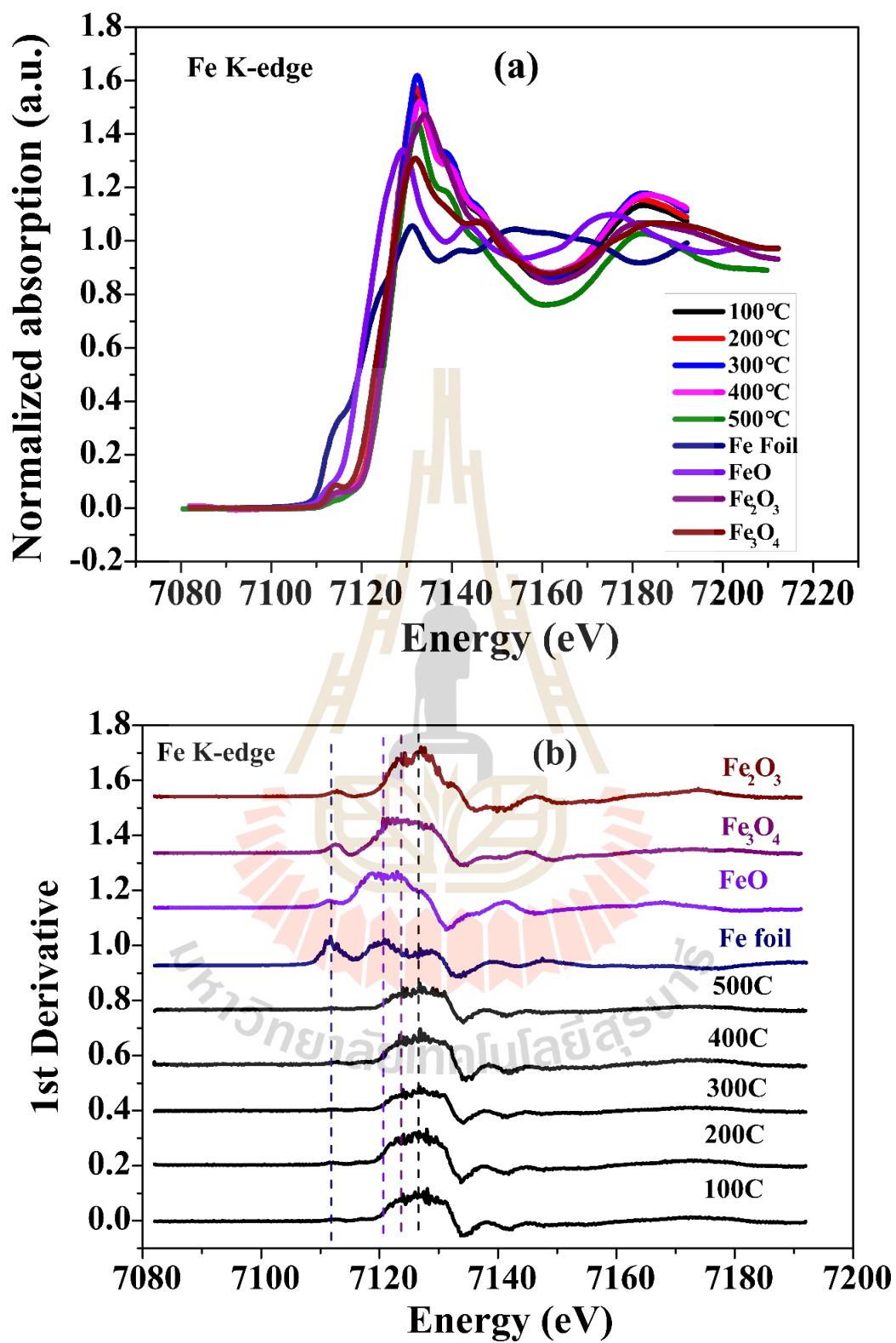


Figure 4.5 (a) Normalized XANES with (b) the associating first derivative plot of the synthesized AgFeO₂ samples at Fe K-edge.

The element composition and oxidation state of delafossite AgFeO_2 sample were characterized by XPS technique. For all the prepared AgFeO_2 samples, the binding energy associated with Ag 3d, Fe 2p, and O 1s as presented by the XPS survey spectrum (Figure 4.6). To fit the Ag 3d spectra of all the AgFeO_2 samples, the Gaussian fitting method was employed. As displayed in Figure 4.7, the two main peaks of Ag 3d spectra were found at 367.05 eV (Ag $3d_{5/2}$) and 372.98 eV (Ag $3d_{3/2}$). Furthermore, these peaks are provided the existence of Ag^+ valence state. Hence, it is clear that Ag was in the Ag^+ valence state which corresponds to the XANES results. For the XPS spectrum of Fe 2p, The Fe atom electronic configuration in the states of $2p_{3/2}$ and $2p_{1/2}$ were discovered at ~ 711 eV and ~ 724 eV binding energies, respectively with a separation of ~ 15.5 eV and two satellites (denoted as “Sat.”) (Figure 4.8). The consisting of two main peaks at ~ 711 eV (Fe $2p_{3/2}$) and ~ 724 eV (Fe $2p_{1/2}$) of the delafossite AgFeO_2 samples confirmed the oxidation states of Fe^{3+} (Ahmed et al., 2020; Yamashita and Hayes, 2008; Mills and Sullivan, 1983; Hawn and DeKoven, 1987; Muhler, Schlögl, and Ertl, 1992). By the results of O 1s fitting, the peaks are observed at ~ 529 eV and 531.5 eV corresponding to the lattice oxygen in the delafossite AgFeO_2 structure and OH^- group, respectively (Figure 4.9) (Ahmed et al., 2020; Che et al., 2016).

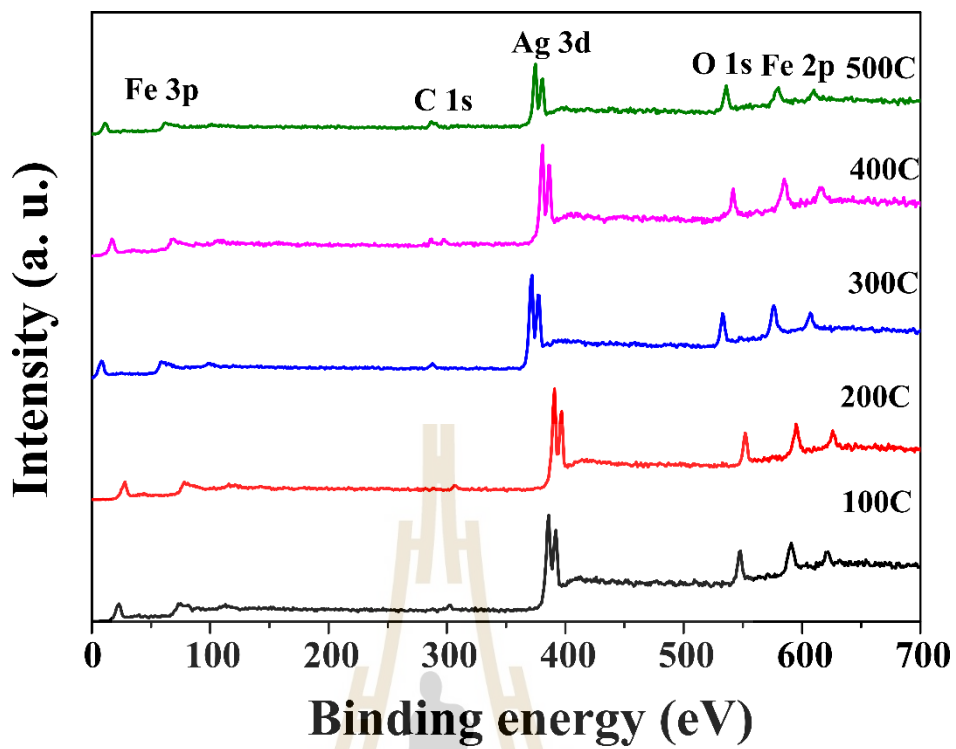


Figure 4.6 XPS survey spectrum of the prepared AgFeO₂ calcined at different temperatures.

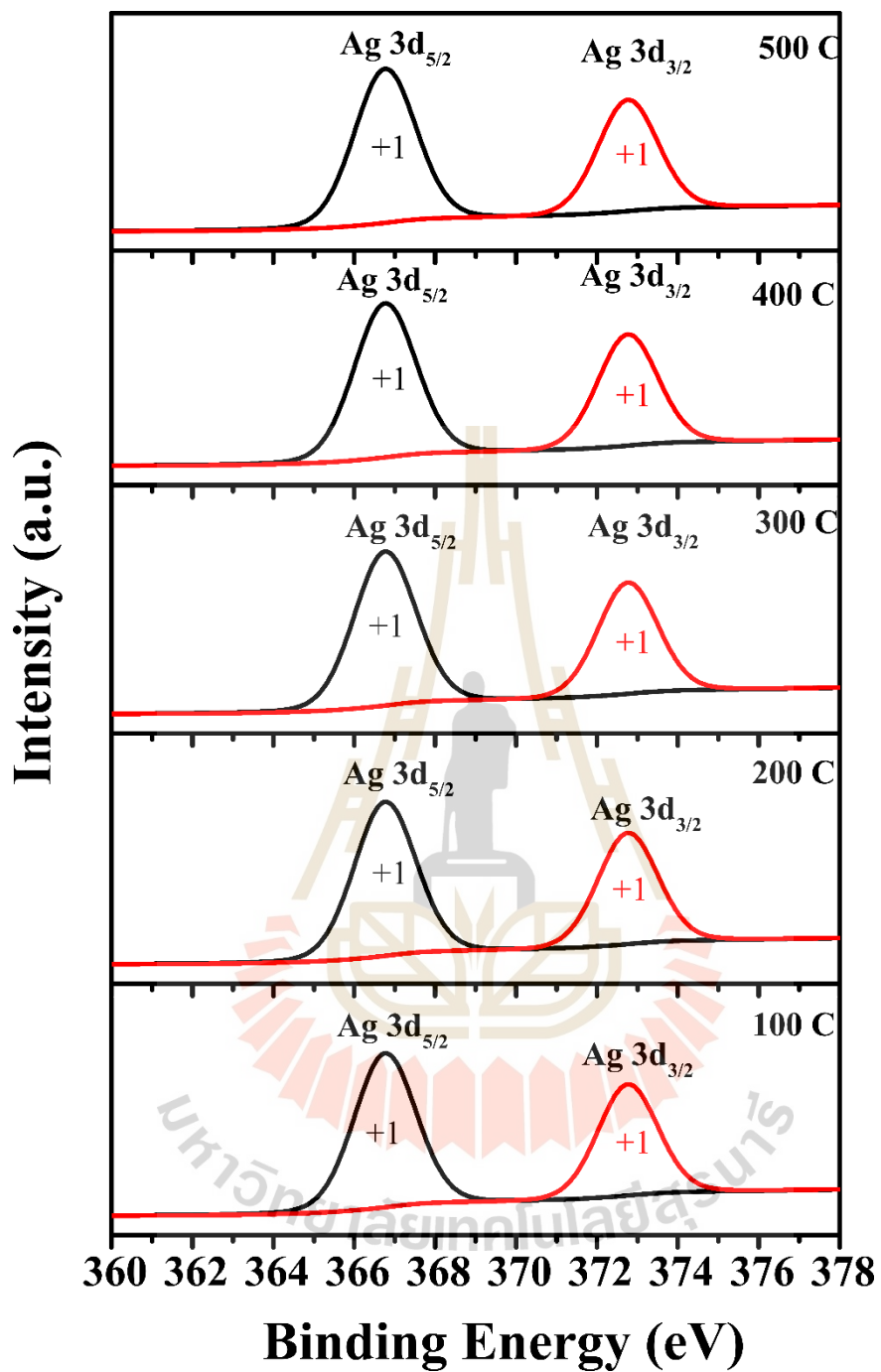


Figure 4.7 XPS spectrum at Ag 3d of all the prepared AgFeO₂.

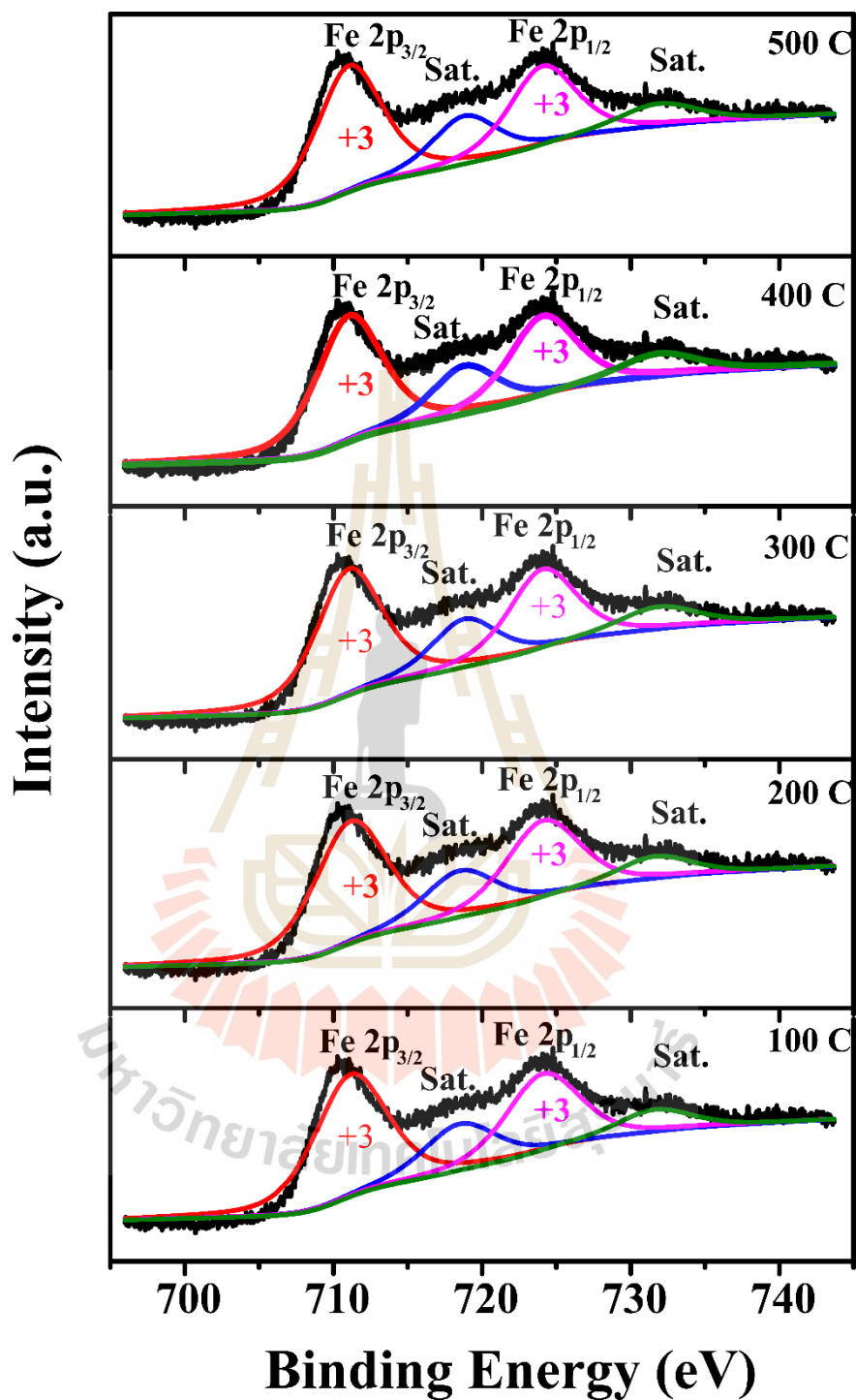


Figure 4.8 XPS spectrum at Fe 2p of all the prepared AgFeO₂ samples.

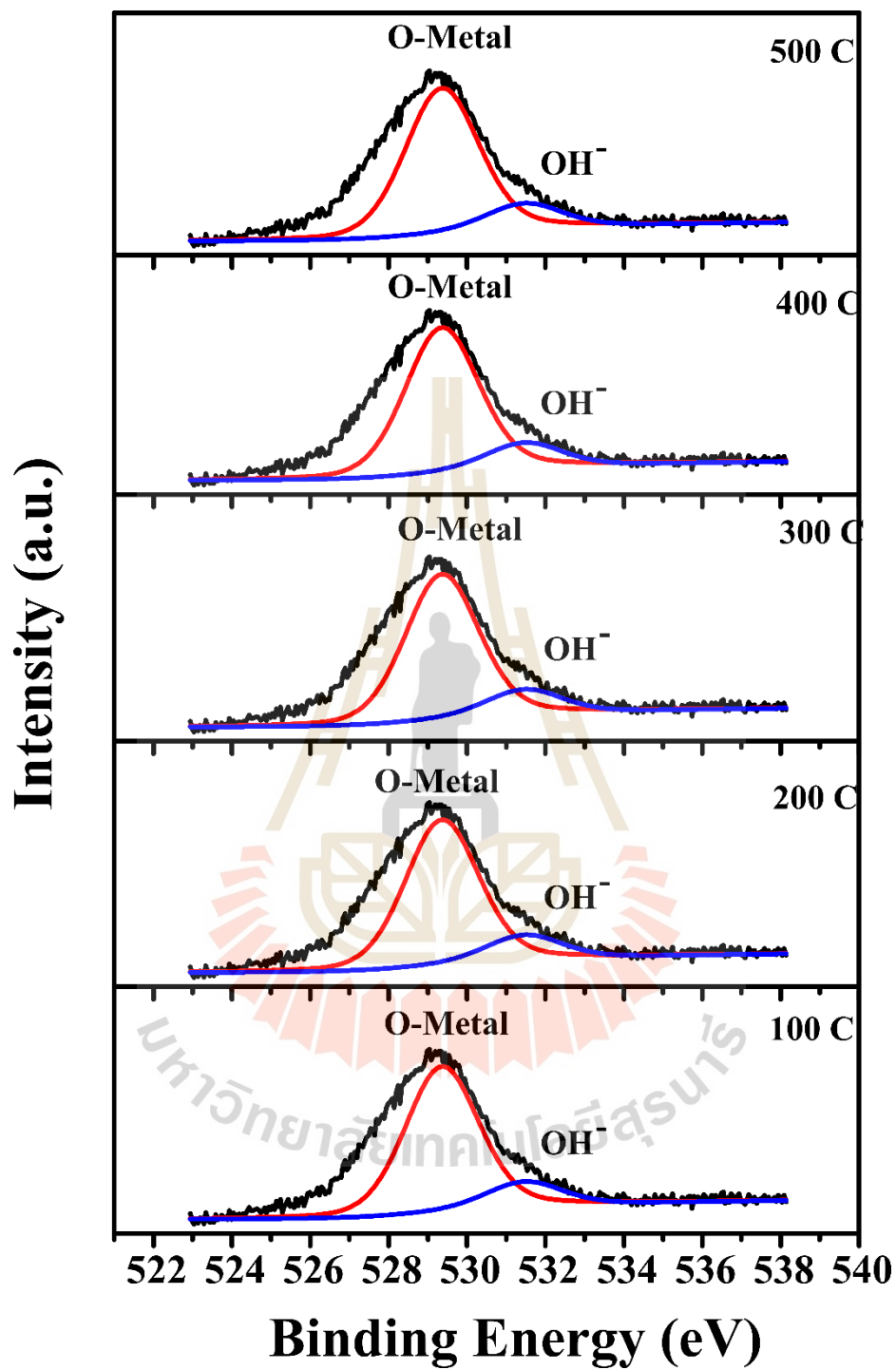


Figure 4.9 XPS spectrum at O 1s of all the prepared AgFeO₂ samples.

4.1.3 Surface area, pore volume and distribution of pore size study of AgFeO₂ nanoparticles by BJH and BET methods

The pore size distribution (inset) and N₂ adsorption-desorption isotherm of the prepared samples are depicted in Figure 4.10(a-e). N₂ adsorption-desorption isotherm results show a small hysteresis loop seeming in the 0 to 1 range which demonstrated that all the AgFeO₂ sample is related to the typical characteristic of mesoporous material. BJH approach was utilized to calculate the total pore volume and pore size distribution of the synthesized samples which confirmed that the samples have a typical attribute of mesoporous materials with the value of pore diameter in range of 2-50 nm corresponding to the adsorption-desorption isotherm of N₂. Additionally, the specific surface area of AgFeO₂ nanoparticles was estimated by BET method. The BET specific surface area (S_{BET}) values of 28.22, 27.22, 23.47, 22.45, and 21.92 m²/g were found to be the samples calcined at 100, 200, 300, 400, and 500°C, respectively. When the calcination temperatures increase, the BET specific surface area seems to decrease. These may be owing to the particle size expanding at the higher temperature. Moreover, the samples calcined at the temperatures of 100, 200, 300, 400, and 500°C exhibit the average pore size diameter (D_{avg}) and BJH pore volume (V_{BJH}) values of 18.95 nm and 0.134 cm³/g, 19.48 nm and 0.133 cm³/g, 23.52 nm and 0.132 cm³/g, 22.46 nm and 0.131 cm³/g and 22.52 nm and 0.123 cm³/g, respectively. Table 4.2 provides the average pore size diameter, BET specific surface area, and BJH pore volume values. According to the report of Naveen, Gurudatt and Shim (Naveen, Gurudatt, and Shim, 2017), the high specific surface area provides the good electrochemical performance due to their excellent ion diffusion between electrode material and electrolyte and resulting in the high specific capacitance. Based on these results, it reveals the different calcination temperatures of AgFeO₂ nanoparticles affect their physical properties including the specific surface area, pore volume and pore size distribution.

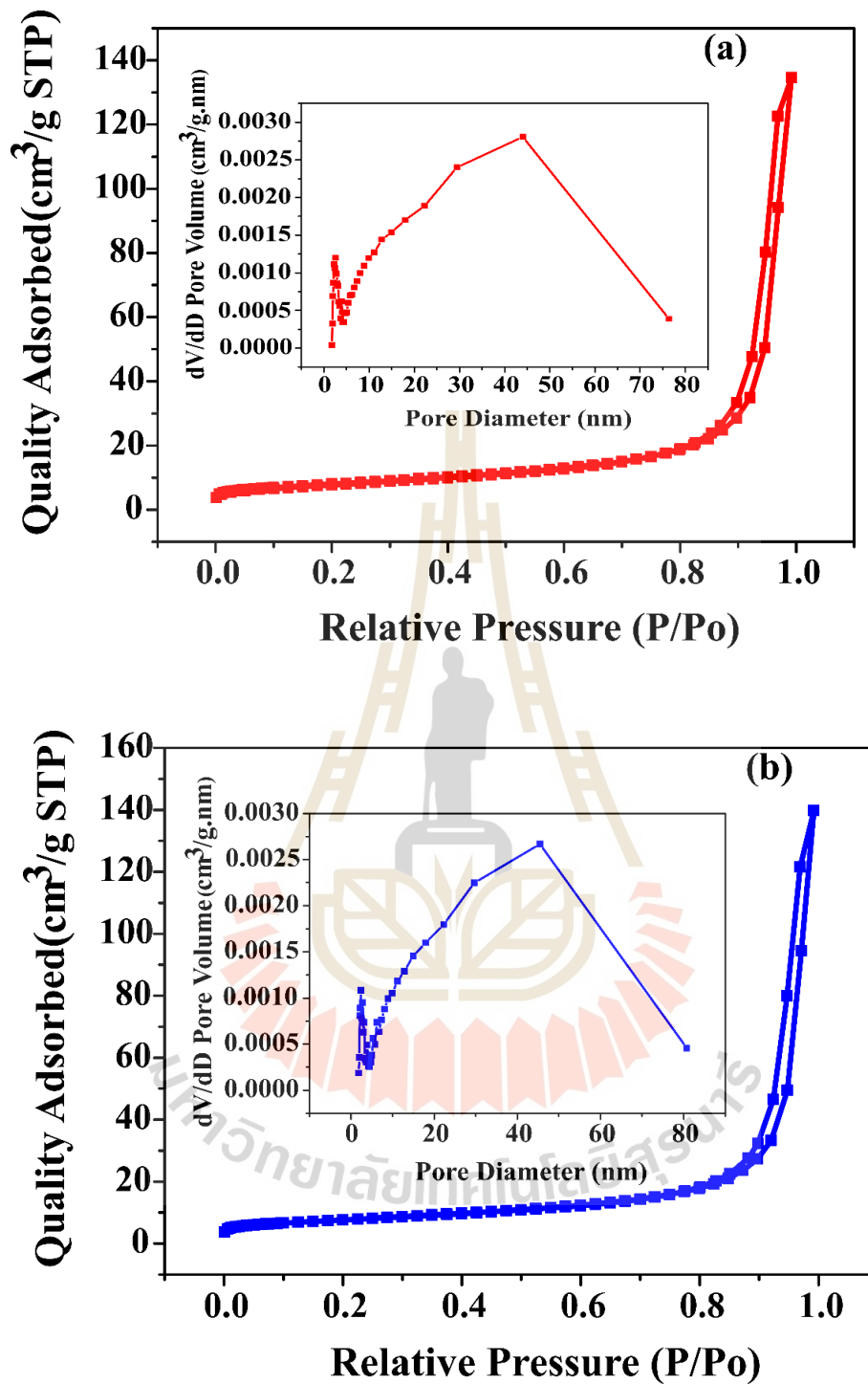


Figure 4.10 The pore size distribution (inset) and N₂ adsorption/desorption isotherm of the AgFeO₂ samples calcined at (a) 100°C, (b) 200°C, (c) 300°C, (d) 400°C, and (e) 500°C.

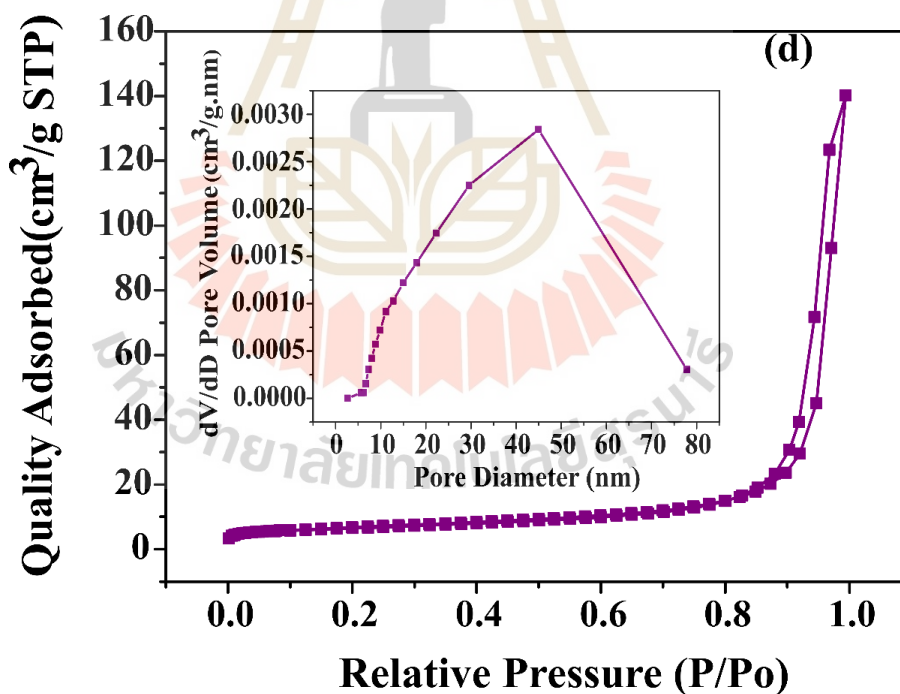
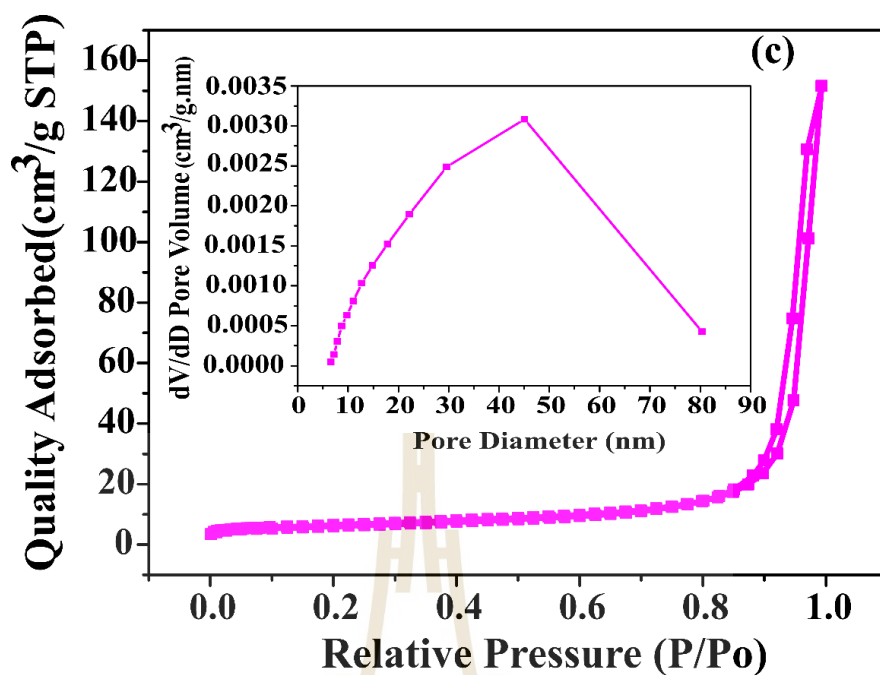


Figure 4.10 (Continued) The pore size distribution (inset) and N_2 adsorption-desorption isotherm of the $AgFeO_2$ samples calcined at (a) 100°C, (b) 200°C, (c) 300°C, (d) 400°C, and (e) 500°C.

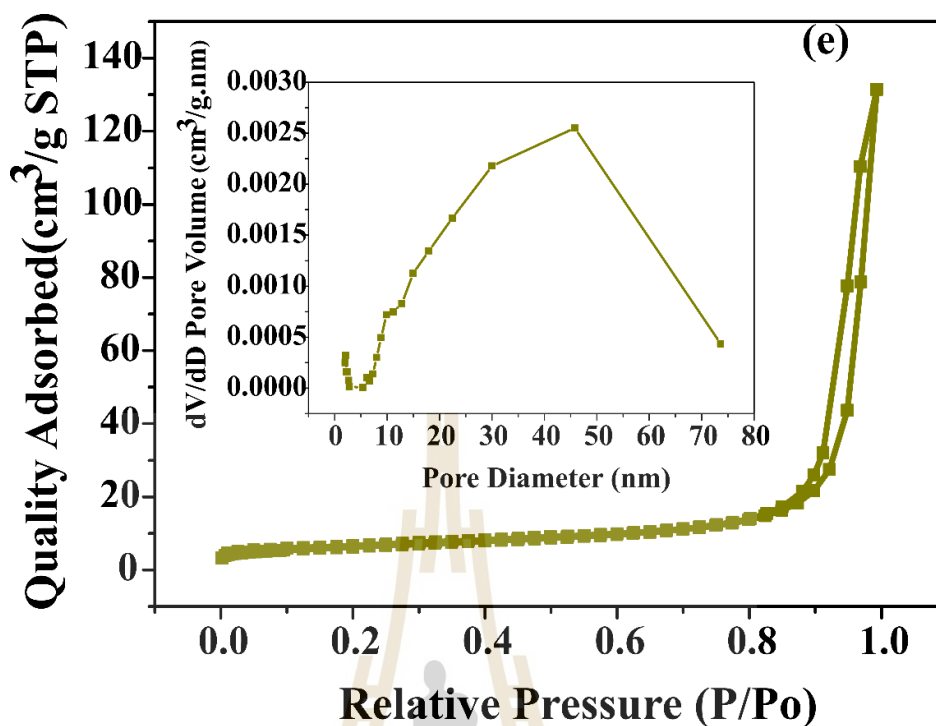


Figure 4.10 (Continued) The pore size distribution (inset) and N_2 adsorption-desorption isotherm of the $AgFeO_2$ samples calcined at (a) 100°C, (b) 200°C, (c) 300°C, (d) 400°C, and (e) 500°C.

Table 4.3 Porosity parameters of $AgFeO_2$.

Conditions	S_{BET} (m^2/g)	V_{BJH} (cm^3/g)	D_{avg} (nm)
100 °C	28.22	0.134	18.95
200 °C	27.22	0.133	19.48
300 °C	23.45	0.132	23.52
400 °C	22.47	0.131	22.46
500 °C	21.92	0.123	22.52

4.1.4 Electrochemical performance of AgFeO₂ nanoparticles

4.1.4.1 Cyclic voltammetry performance

To analyze electrochemical performance of AgFeO₂ nanoparticles, CV technique was employed to examine. The cyclic voltammetry (CV) testing of AgFeO₂ electrode was measured under the potential ranging from -1.16 V to 0.35 V at 2 mV/s to 100 mV/s scan rates in 3 KOH electrolyte. Figure 4.11(a-e) presents the CV curves of all the AgFeO₂ electrodes at the various scan rates of 2-100 mV/s. Based on the results as seen in Figure 4.11(a-e), the CV curves of the electrodes perform the typical characteristic of pseudocapacitor with the clarity of redox peaks. The CV curve of all the AgFeO₂ nanoparticles show the four reduction-oxidation peaks at the potential values of -1.10 V, -0.73 V, 0.05 V and 0.25 V. The reduction-oxidation peaks at the potential of -1.10 V and -0.73 V reveal the oxidative transformation between the reduction-oxidation pairs of Fe³⁺ and Fe²⁺ (Wongpratad et al., 2020; Pai et al., 2018). Additionally, the oxidative transformation between the reduction-oxidation pairs of Ag and Ag⁺ associate with the redox peaks at the potential of 0.05 V and 0.25 V (Anderson et al., 2017; Van der Horst et al., 2015). The reversible redox reaction of the reduction-oxidation pairs of the oxidative transformation between Ag and Ag⁺ and Fe³⁺ and Fe²⁺ can be explained by the equations as follow:



or



And



or



For all the AgFeO_2 electrodes, the anodic and cathodic peaks position shift with the increasing. These provide the high-rate performance and excellent electrochemical reversibility (Peng and Tarleton, 2015). According to the CV curve of all the samples, the specific capacitance value can be estimated by using the equation 3.17, as seen in Figure 4.12. With an increase in the ranging from 2 to 100 mV/s scan rate, the specific capacitance of all the synthesized AgFeO_2 samples exhibited a decrease. This can also be observed in pseudocapacitive electrode material when the scan rate is high, as restricts the time available for ion diffusion at the surface of the AgFeO_2 electrode. At the 2 mV/s scan rate, the calculated values of specific capacitance are 358.32, 324.76, 319.64, 332.21 and 318.55 F/g were received from the samples calcined at 100, 200, 300, 400, and 500°C, respectively. According to these specific capacitance values, the sample calcined at the temperature of 100°C provides the highest specific capacitance value may owing to its highest 2H phase percentage (70.06%) and BET specific surface area which results in good ion diffusion between the electrode material and electrolyte (Zhu et al., 2014; Padmanathan and Selladurai, 2014).



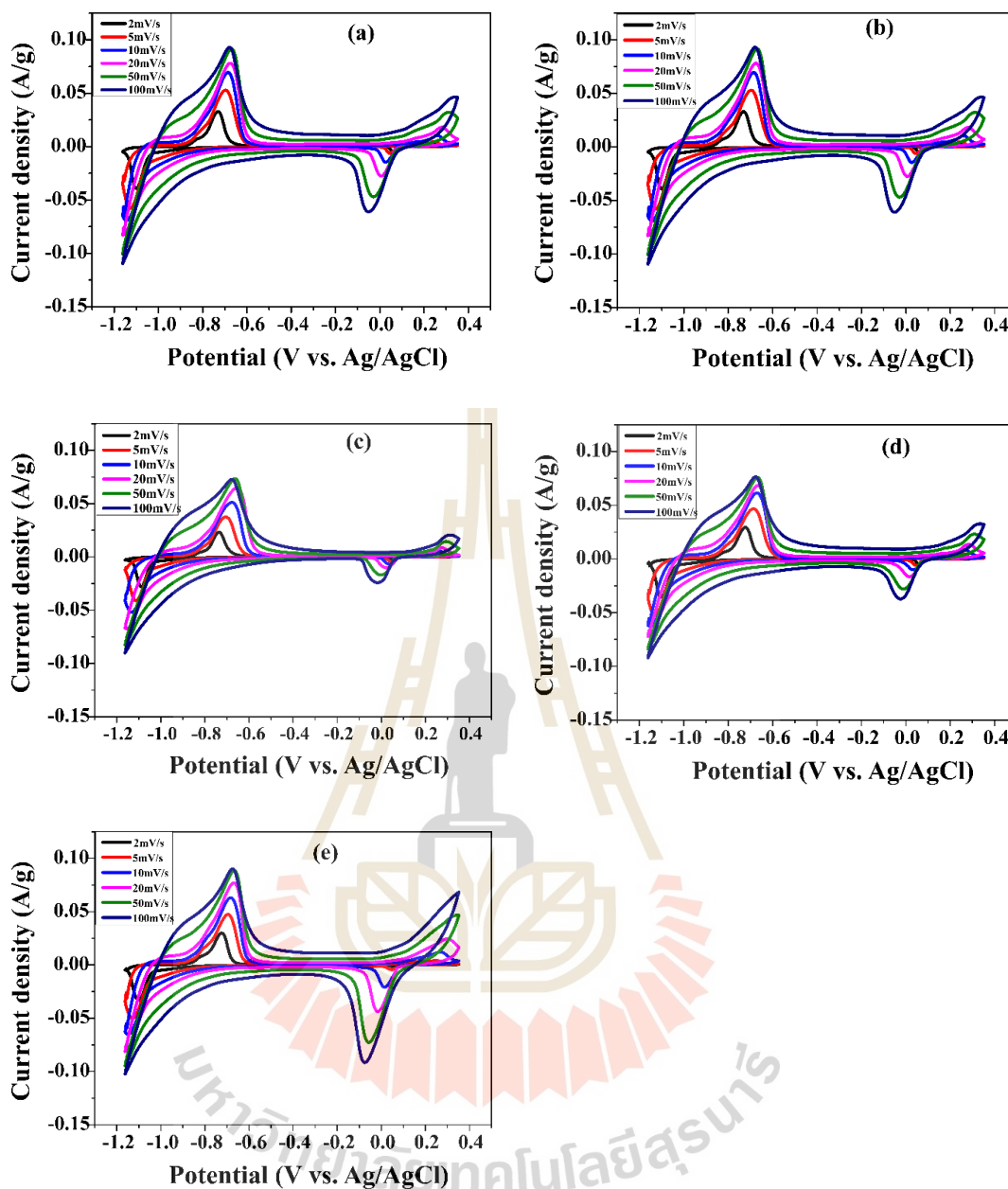


Figure 4.11 CV curves at ranging from 2 mV/s to 100 mV/s scan rates of the prepared AgFeO_2 nanoparticles calcined at at (a) 100°C , (b) 200°C , (c) 300°C , (d) 400°C , and (e) 500°C .

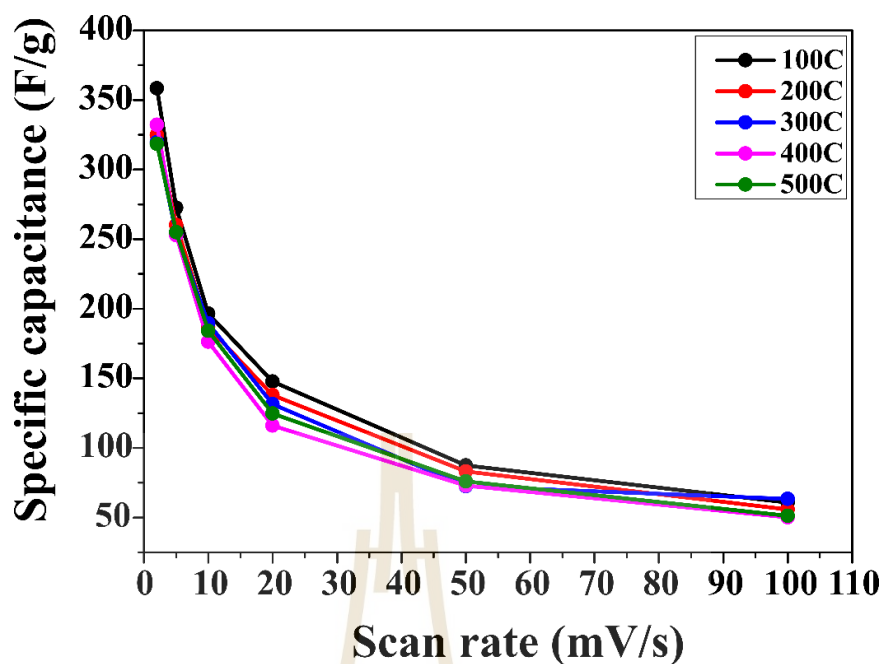


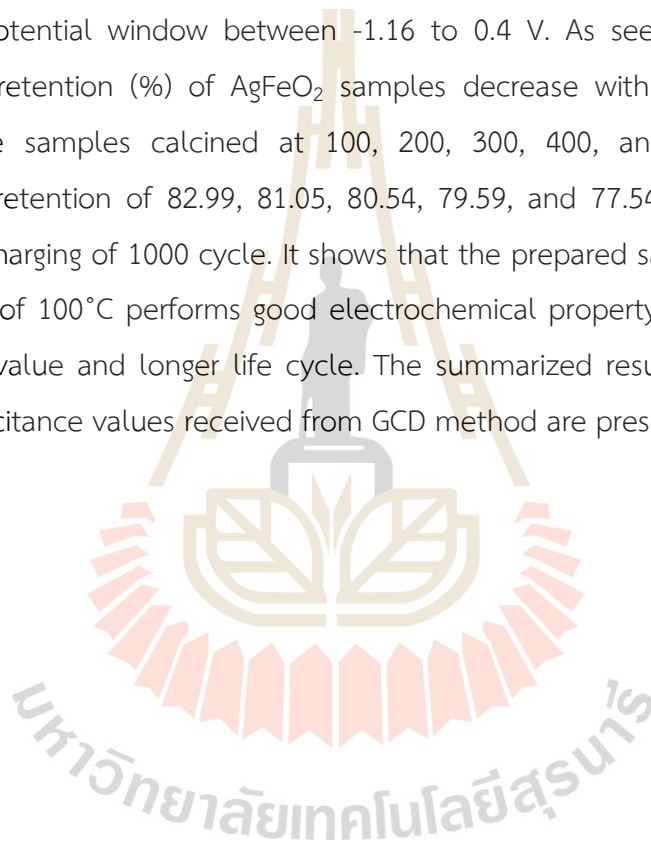
Figure 4.12 The calculated specific capacitance at the various scan rates of the synthesized AgFeO_2 nanoparticle calcined at different temperatures.

4.1.4.2 Galvanostatic charge discharge measurement

The results of GCD measurement of the AgFeO_2 samples which represented by the curves as the function of the ranging from 1 A/g to 20 A/g current densities are displayed in Figure 4.13(a-e). The GCD curves of all the AgFeO_2 electrodes indicate the behavior of pseudocapacitive communicating with the cyclic voltammetry measurement. The discharge curves of the GCD testing were utilized to evaluate the specific capacitance values of all the AgFeO_2 samples by applying equation 3.18. The calculated specific capacitance values of all the samples are displayed in Figure 4.14 which shows that when the current density increases with the decrease of specific capacitance value. The specific capacitance at different current densities is summarized in Table 4.3. This could be assigned to the rise in internal resistance and polarization of the AgFeO_2 electrode. The values of specific capacitance of 229.71, 223.32, 208.61, 195.60, and 168.96 F/g were found to be the samples calcined at temperatures of 100, 200, 300, 400, and 500°C, respectively at the low current density of 1 A/g. This correlates with the values of specific

capacitance calculated from the CV results. The highest value of specific capacitance of 229.71 F/g was observed for the AgFeO_2 calcined at 100°C which has the smallest particle size providing the highest BET specific surface area value and active area of faradaic reversible reduction-oxidation reaction.

Moreover, for the cyclic stability analysis of all the AgFeO_2 electrodes, the capacitance retention was tested employing the continuous charge-discharge measurement at the 5 A/g current density for 1000 cycles in 3 M KOH electrolyte under the potential window between -1.16 to 0.4 V. As seen in Figure 4.15, the capacitance retention (%) of AgFeO_2 samples decrease with increasing the cycle number. The samples calcined at 100, 200, 300, 400, and 500°C exhibit the capacitance retention of 82.99, 81.05, 80.54, 79.59, and 77.54%, respectively after charging/discharging of 1000 cycle. It shows that the prepared sample calcined at the temperature of 100°C performs good electrochemical property with highest specific capacitance value and longer life cycle. The summarized results of the calculated specific capacitance values received from GCD method are present in Table 4.3



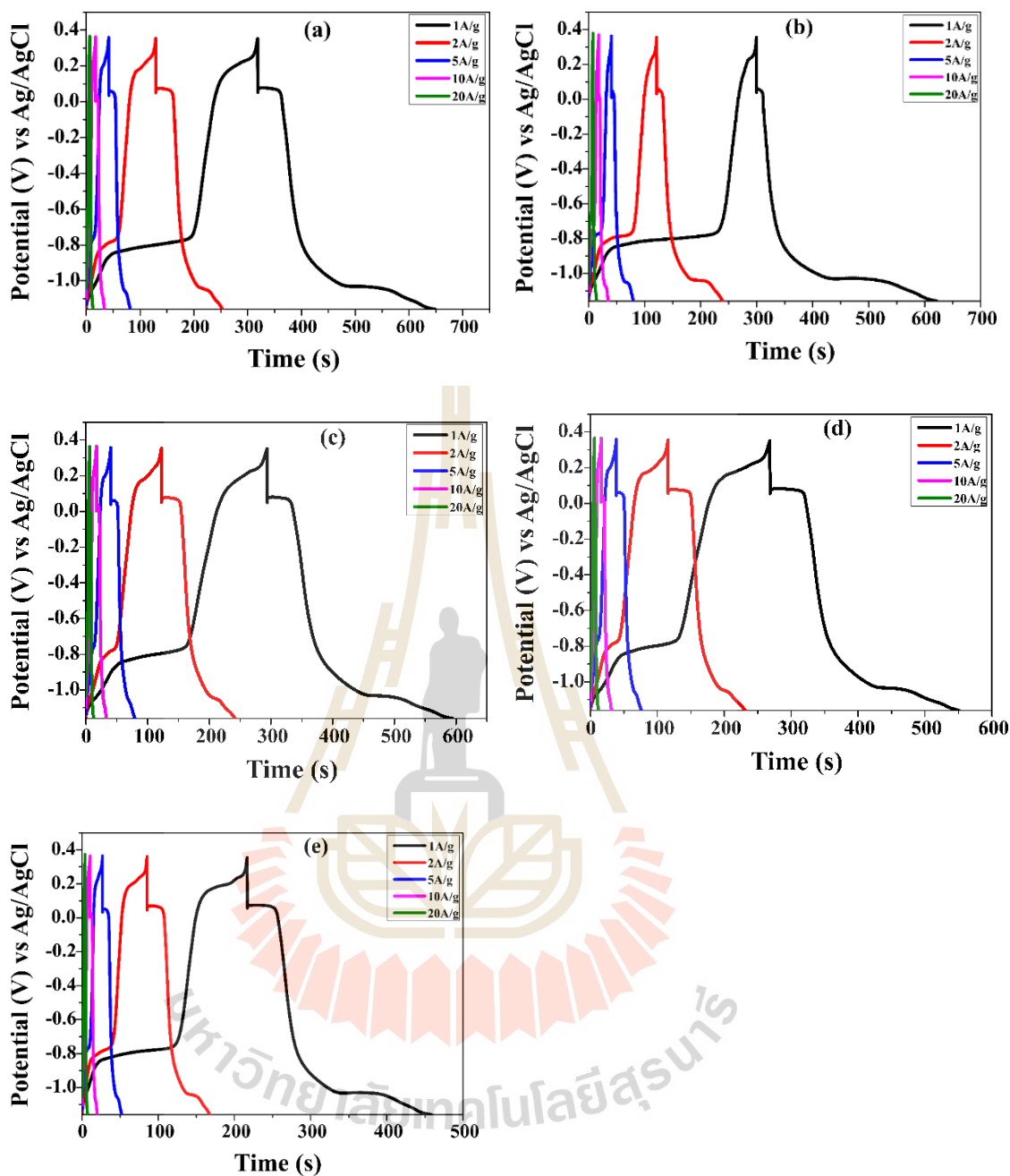


Figure 4.13 Galvanostatic charge/discharge plot of the AgFeO_2 sample at the various current densities of 1, 2, 5, 10, and 20 A/g.

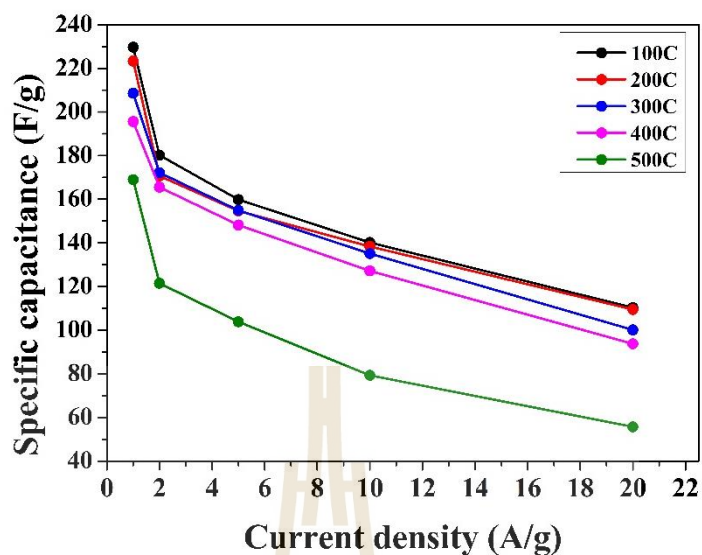


Figure 4.14 The calculated specific capacitance at the various current density of 1, 2, 5, 10 and 20 A/g of the synthesized AgFeO_2 nanoparticle calcined at different temperatures.

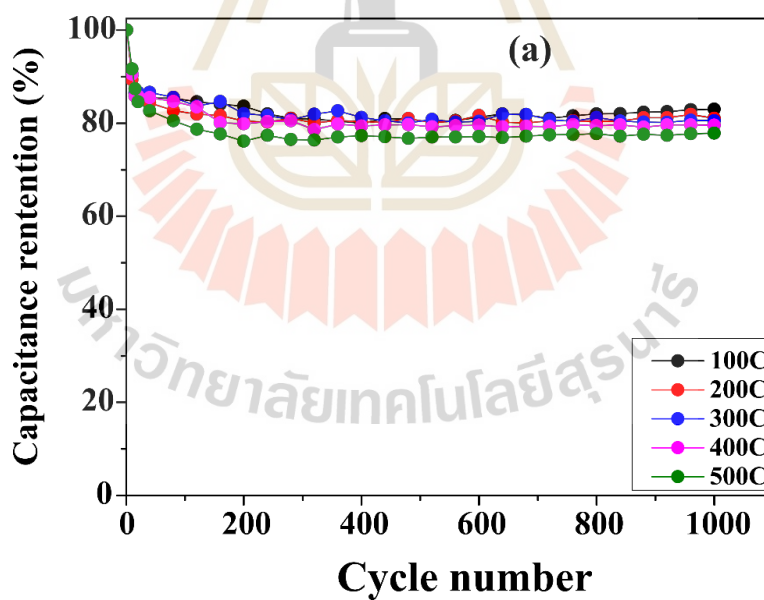


Figure 4.15 Capacitance retention (%) after 1000 cycles at 5 A/g of the AgFeO_2 electrodes calcined at different temperatures.

Table 4.4 The summarized results of the calculated specific capacitance values of AgFeO₂ electrode received from GCD method.

Current density (A/g)	Specific capacitance at various calcination temperatures (F/g)				
	100°C	200°C	300°C	400°C	500°C
1	229.71	223.32	208.6	195.60	168.96
2	180.17	170.66	172.12	165.55	121.54
5	159.87	154.68	154.95	148.14	103.85
10	140.20	138.3	135.04	127.17	79.26
20	110.28	109.43	100.09	93.72	55.73

4.1.4.3 Electrochemical impedance spectroscopy analysis

Electrochemical impedance spectroscopy (EIS) measurement was studied at the frequency range of 10 mHz to 1000 KHz with the potential of 10 mV. In the region of high frequency, EIS curves of all AgFeO₂ samples provide an incomplete semicircle as seen in Figure 4.16 which is the resistance feature at the electrolyte-oxide interface. At high frequency, the intercept on the real axis (Z') gives the solution resistance (R_s) or the equivalence series resistance (R_{esr}). The solution resistance (R_s) values of 1.24, 1.63, 1.39, 1.38 and 1.65 Ω were obtained for the AgFeO₂ calcined at the temperatures of 100, 200, 300, 400 and 500°C, respectively. On the other hands, the resistance of charge transfer (R_{ct}) is represented by the diameter of semicircle. The slopping line at the low frequency indicated the presence of Warburg impedance (W), which signifies the diffusion of the electrolyte ion within the electrode material. Based on the Nyquist plots, the samples calcined at the temperatures ranging from 100 to 500°C exhibited very low charge transfer resistance (R_{ct}) values because it shows the small semicircle in the middle frequency range. Interesting, the lowest solution resistance (R_s) value of the sample calcined at 100°C provided the highest value of specific capacitance while the sample calcined at 500°C shows the highest R_s value resulting in the lowest specific capacitance value. This work implied that the AgFeO₂ nanoparticles can be utilized as electrode material for the energy storage applications.

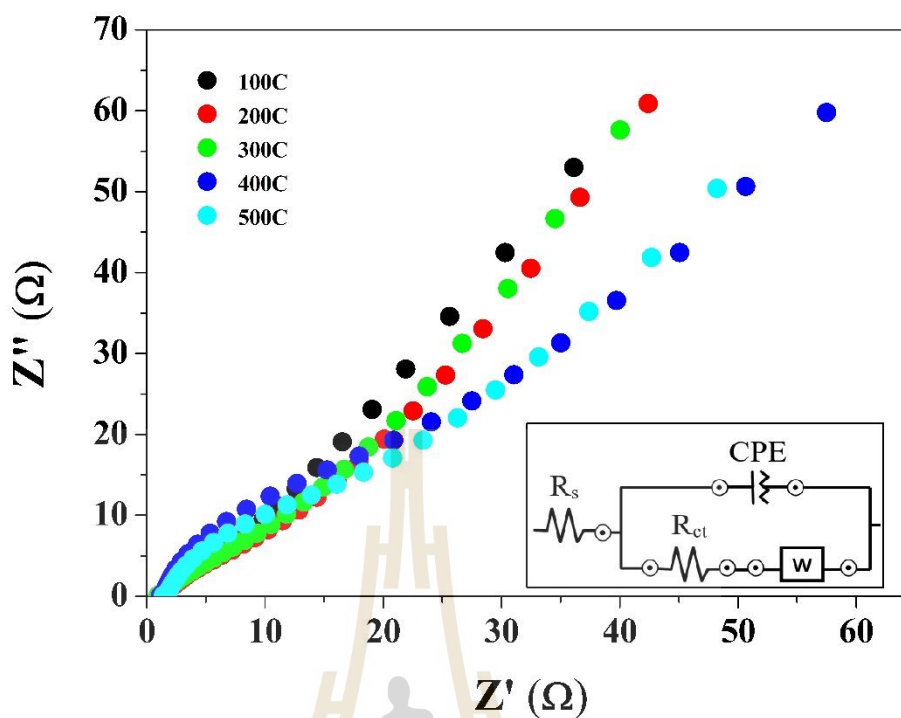


Figure 4.16 Nyquist plots of AgFeO₂ samples calcined at various temperatures.

4.1.4.4 Specific energy and specific power study

The Ragone plot is commonly used to represent the energy storage device performance. It exhibits the correlation between the specific power and specific energy at the different current densities ranging from 1 A/g to 20 A/g, as seen in Figure 4.17. The specific energy seems to decrease with increasing calcination temperature. Specifically, at a current density of 1 A/g, the sample calcined at 100, 200, 300, 400 and 500°C yielded specific energies and specific power values of 72.74 Wh/Kg and 797.46 W/Kg, 66.06 Wh/Kg and 791.17 W/Kg, 53.86 Wh/Kg and 788.39 W/Kg, 61.94 Wh/Kg and 789.75 W/Kg, and 53.50 Wh/Kg and 599.67 W/Kg, respectively. This indicates that AgFeO₂ nanoparticles have potential as electrode materials for energy storage technology.

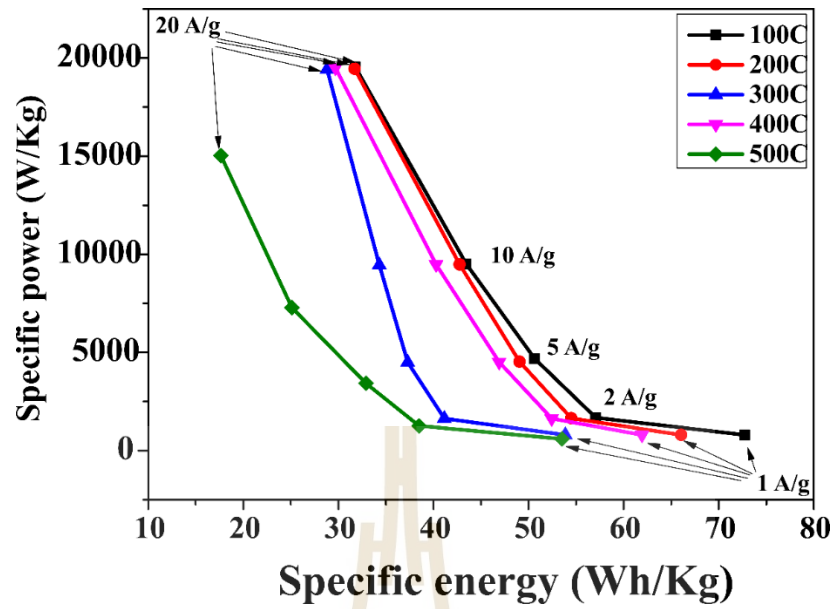


Figure 4.17 The specific energies and their corresponding specific powers of AgFeO₂ nanostructures at different current densities ranging from 1 to 20 A/g.

4.2 Co-doped AgFeO₂ nanoparticles

4.2.1 Structure and morphologies analysis of the Co-doped AgFeO₂ nanoparticles by XRD, TEM and SEM

Figure 4.18 represents the XRD patterns of the synthesized AgFe_{1-x}Co_xO₂ nanoparticles with $x = 0.00, 0.05, 0.10, 0.15$ and 0.20 . Regarding the undoped condition ($x = 0.00$), the presence of the delafossite AgFeO₂ phases of 2H (PDF2 No: 00-029-1141) and 3R (PDF2 No: 00-018-1175) was confirmed, indicating its purity. Upon comparing the obtained pattern with the database standards representing the rhombohedral 3R-AgFeO₂ and hexagonal polytype 2H-AgFeO₂, it was confirmed that both phases mixture was achieved. When analyzing the prepared AgFe_{1-x}Co_xO₂ samples with the different concentration of cobalt ($x = 0.05, 0.10, 0.15, 0.20$), their patterns exhibited similarities. The only observed difference were in broadening of the diffraction peaks and the intensity. The values of lattice parameter value of $a = 3.041 \text{ \AA}$ and $c = 18.550 \text{ \AA}$ were found for 2H phase while 3R phase shows the values of lattice parameter values of $a = 3.041 \text{ \AA}$ and $c = 18.550 \text{ \AA}$. The observation reveals that the peaks associated with the (001) family are distinct and clearly defined. Even though there are additional peaks present in the XRD spectra of the doped samples, which could be attributed to metallic silver (shown as red markers in Figure 4.18), there are no indications of impurity phases like metallic cobalt, CoO, Fe₂O₃, or CoFe₂O₄ spinel. These impurity phases typically form under condition similar to the synthesis of AgFeO₂. The absence of cobalt-related phases suggests that cobalt ions might substitute iron ions within the delafossite crystal structure. Nonetheless, the presence of metallic silver comes as a surprising observation when considering the assumption that Co²⁺ would replace Fe³⁺ ions during substitution. However, since cobalt (II) nitrate was applied as the starting material in the synthesis process, proposes that in this specific case, divalent cobalt ions could substitute trivalent iron ions. This presumption could account for the occurrence of metallic silver as a secondary phase (Siedliska et al., 2019).

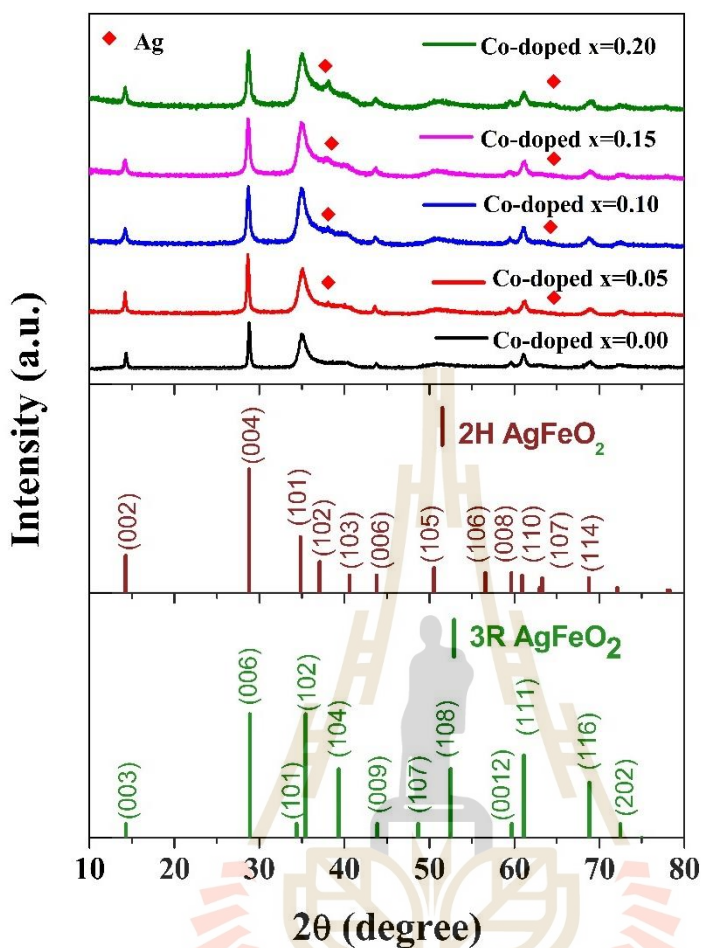


Figure 4.18 XRD patterns of the $\text{AgFe}_{1-x}\text{Co}_x\text{O}_2$ nanoparticles.

Additionally, the images of FESEM were employed to study the structural and morphologies of the Co-doped AgFeO_2 samples, as shown in Figure 4.19(a-e). FESEM result shows that the size of particle range seems to reduce with increasing the Co concentration. At the different doping concentrations, FESEM images of $\text{AgFe}_{1-x}\text{Co}_x\text{O}_2$ samples with Co concentration $x = 0.00, 0.05, 0.10, 0.15, 0.20$ exhibited the mean particle sizes of 45, 22, 20, 17, and 21 nm, respectively. Moreover, TEM results were employed to demonstrate the morphologies and structure of $\text{AgFe}_{1-x}\text{Co}_x\text{O}_2$ samples. Figure 4.20(a-j) interprets the images of TEM with the associating SAED and HRTEM images of Co-doped AgFeO_2 nanoparticle with different doping concentrations. The bright field TEM images represent the particle size of all

the samples in nanometer range. Furthermore, the corresponding SAED and high-resolution TEM images reveal the presence of delafossite AgFeO_2 phase which communicates to the XRD results.

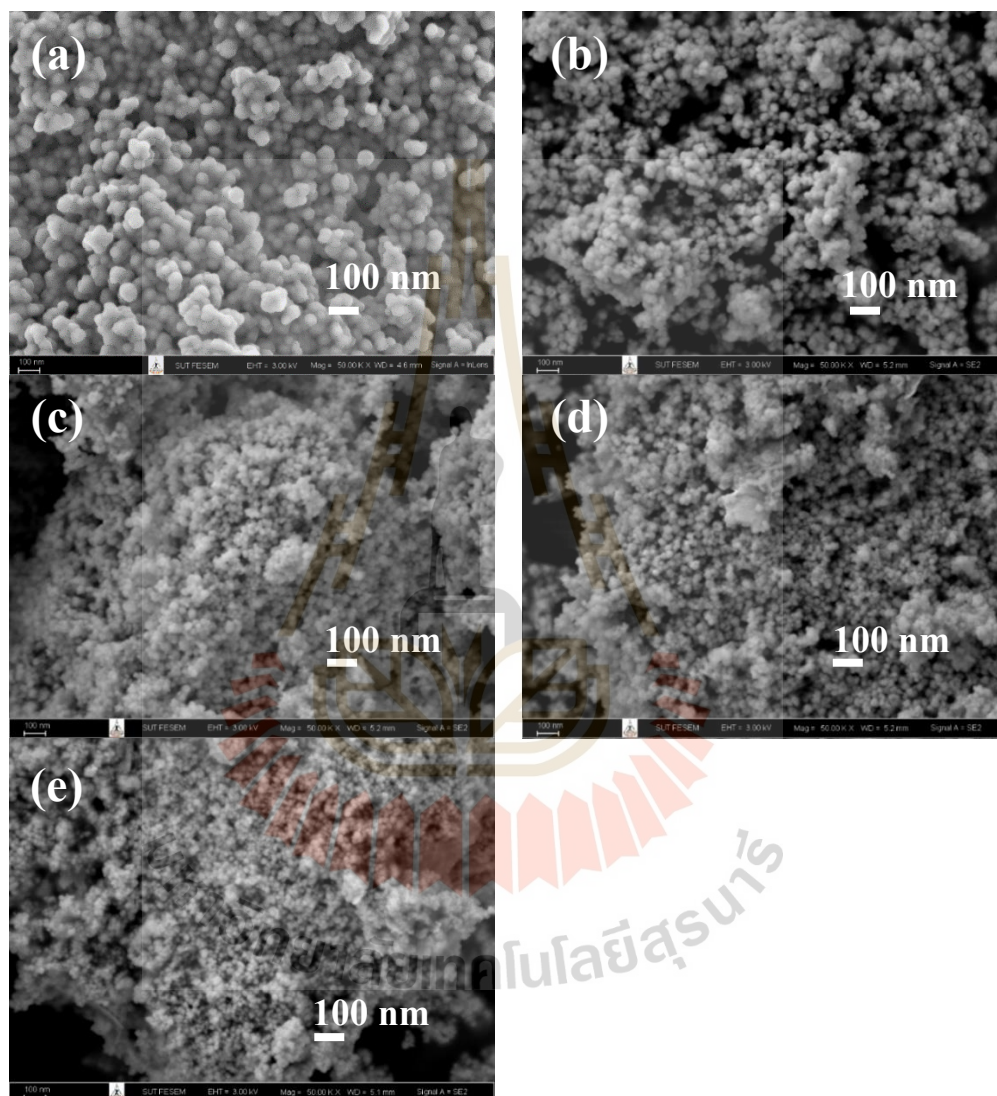


Figure 4.19 The images of FESEM of $\text{AgFe}_{1-x}\text{Co}_x\text{O}_2$ samples: (a) $x = 0.00$, (b) $x = 0.05$, (c) $x = 0.10$, (d) $x = 0.15$ and (e) $x = 0.20$.

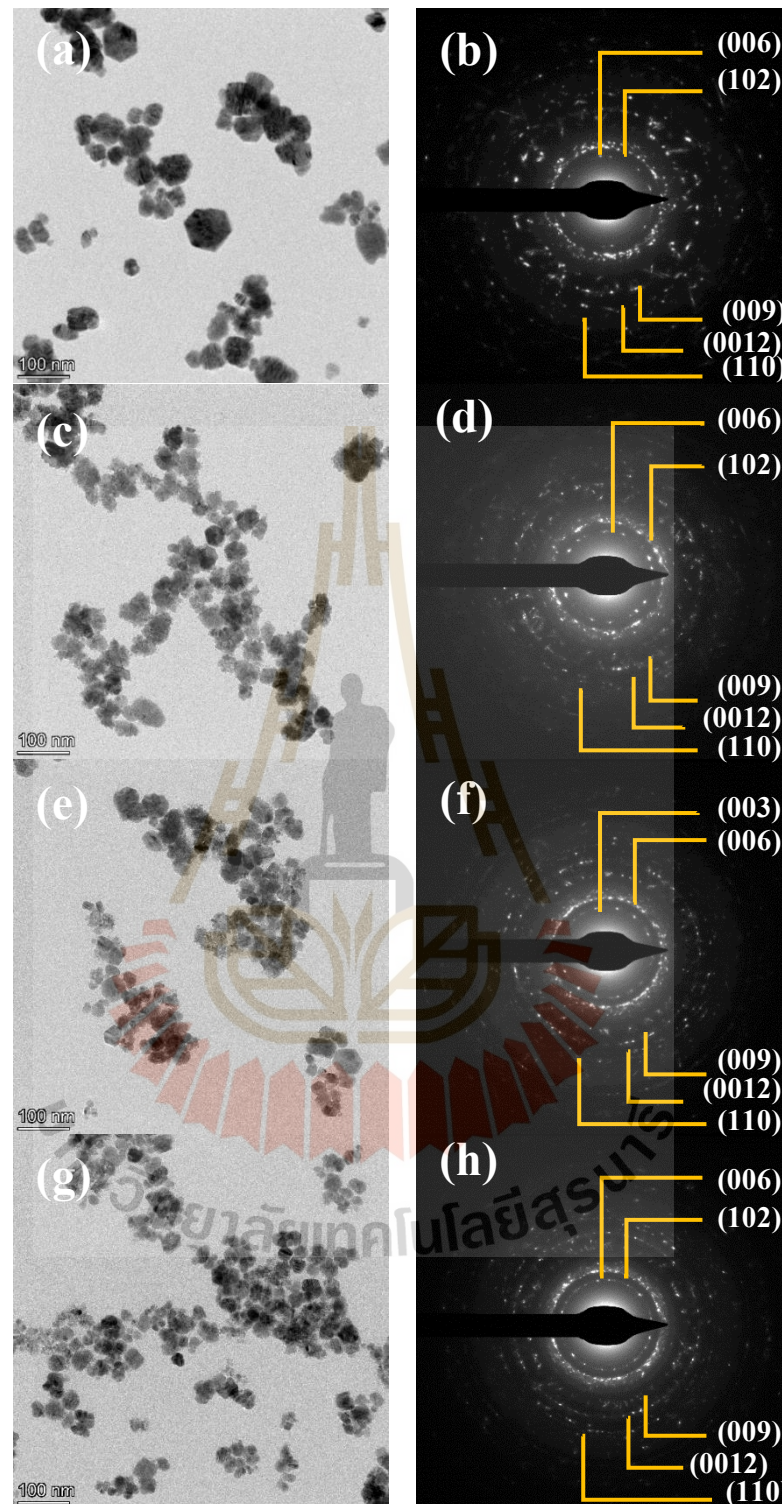


Figure 4.20 TEM images and associating SAED of $\text{AgFe}_{1-x}\text{Co}_x\text{O}_2$ nanoparticle: (a,b) $x = 0.00$, (c,d) $x = 0.05$, (e,f) $x = 0.10$, (g,h) $x = 0.15$, and (i,j) $x = 0.20$.

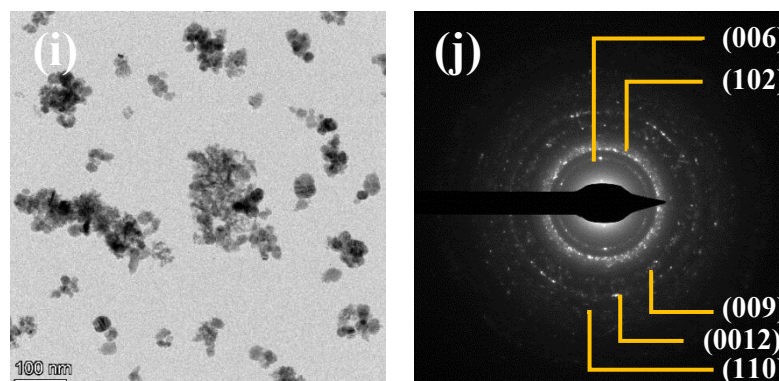


Figure 4.20 (Continued) TEM images and SAED of $\text{AgFe}_{1-x}\text{Co}_x\text{O}_2$ nanoparticle: (a,b) $x = 0.00$, (c,d) $x = 0.05$, (e,f) $x = 0.10$, (g,h) $x = 0.15$, and (i,j) $x = 0.20$.

4.2.2 Oxidation state and surface chemical composition study of Co-doped AgFeO_2 nanoparticles by XAS and XPS

The technique of XANES was employed to examine the Ag, Fe and Co oxidation states in $\text{AgFe}_{1-x}\text{Co}_x\text{O}_2$ samples. The XANES spectra of standard samples of Ag foil (Ag^0), Ag_2O (Ag^+), AgO (Ag^{2+}), Fe foil (Fe^0), FeO (Fe^{2+}), Fe_2O_3 (Fe^{3+}), Co foil, CoO (Co^{2+}), Co_3O_4 ($\text{Co}^{2+}, \text{Co}^{3+}$), and LiCoO_3 (Co^{3+}) were employed to analyze the $\text{AgFe}_{1-x}\text{Co}_x\text{O}_2$ ($x = 0.00, 0.05, 0.10, 0.15, 0.20$) nanoparticles. Basically, the Ag, Fe and Co oxidation states were indicated by the edge position shift. Figure 4.21(a), 4.22(a-b) and 4.23(a-b) show the normalized XANES spectrum and first derivative plot at Ag L3-edge, Co K-edge, and Fe K-edge of the Co-doped AgFeO_2 nanoparticles, respectively. According to the normalized XANES with the associated first derivative at Ag L3-edge of Co-doped AgFeO_2 nanoparticles, their edge positions were located close to the standard sample of Ag_2O (Ag^+). These show that Ag in the Co-doped AgFeO_2 nanoparticles exists in the mixed oxidation number of +1. At Fe K-edge for the XANES spectra in the $\text{AgFe}_{1-x}\text{Co}_x\text{O}_2$ samples, the edge positions were very close to the reference sample of Fe_2O_3 (Fe^{3+}). It reveals that the Fe ion valence state in the Co-doped AgFeO_2 samples is +3. At Co K-edge for all samples, the normalized XANES spectra exhibited edge positions similar to the edge position of LiCoO_2 (Co^{3+}) reference sample. This provides information on the oxidation state of Co.

approximately +3. The valence states of Ag, Fe and Co and their energy edge position were summarized in Table 4.4.

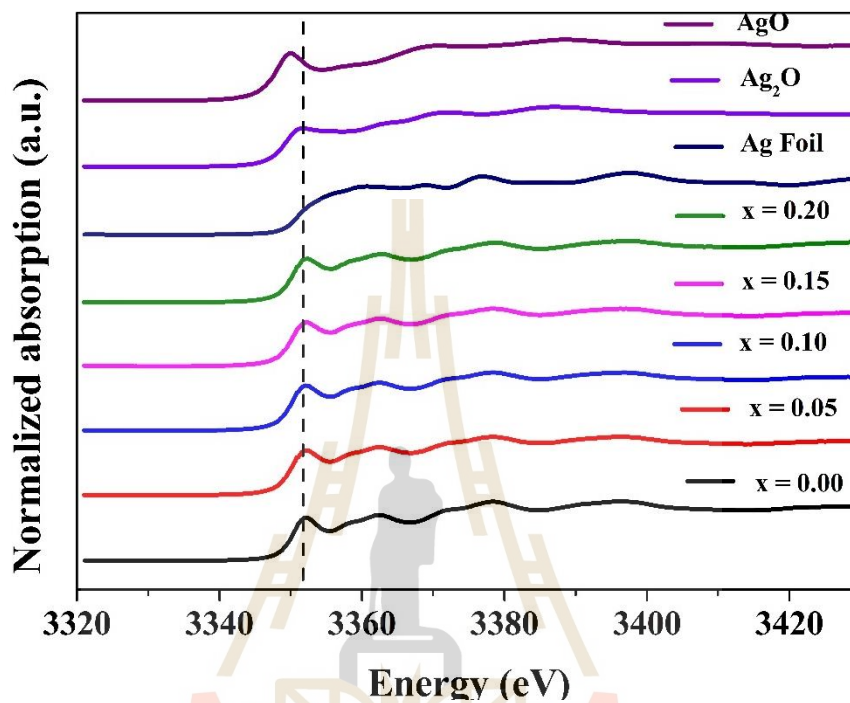


Figure 4.21 (a) Normalized XANES spectrum plot at Ag L3-edge of Co-doped AgFeO₂ nanoparticles.

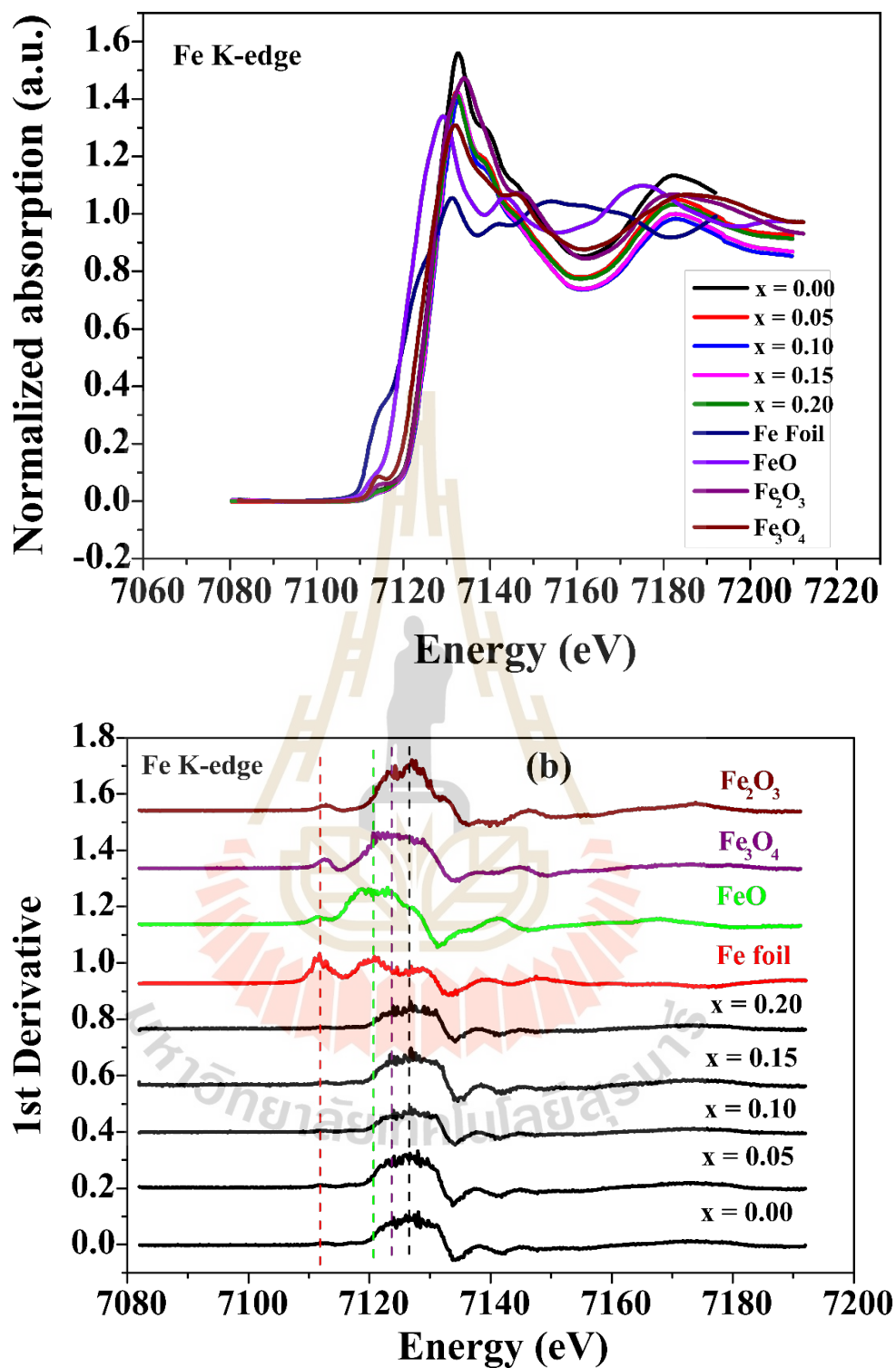


Figure 4.22 (a) Normalized XANES with (b) the associating first derivative plot at Fe K-edge of $\text{AgFe}_{1-x}\text{Co}_x\text{O}_2$ with different concentration.

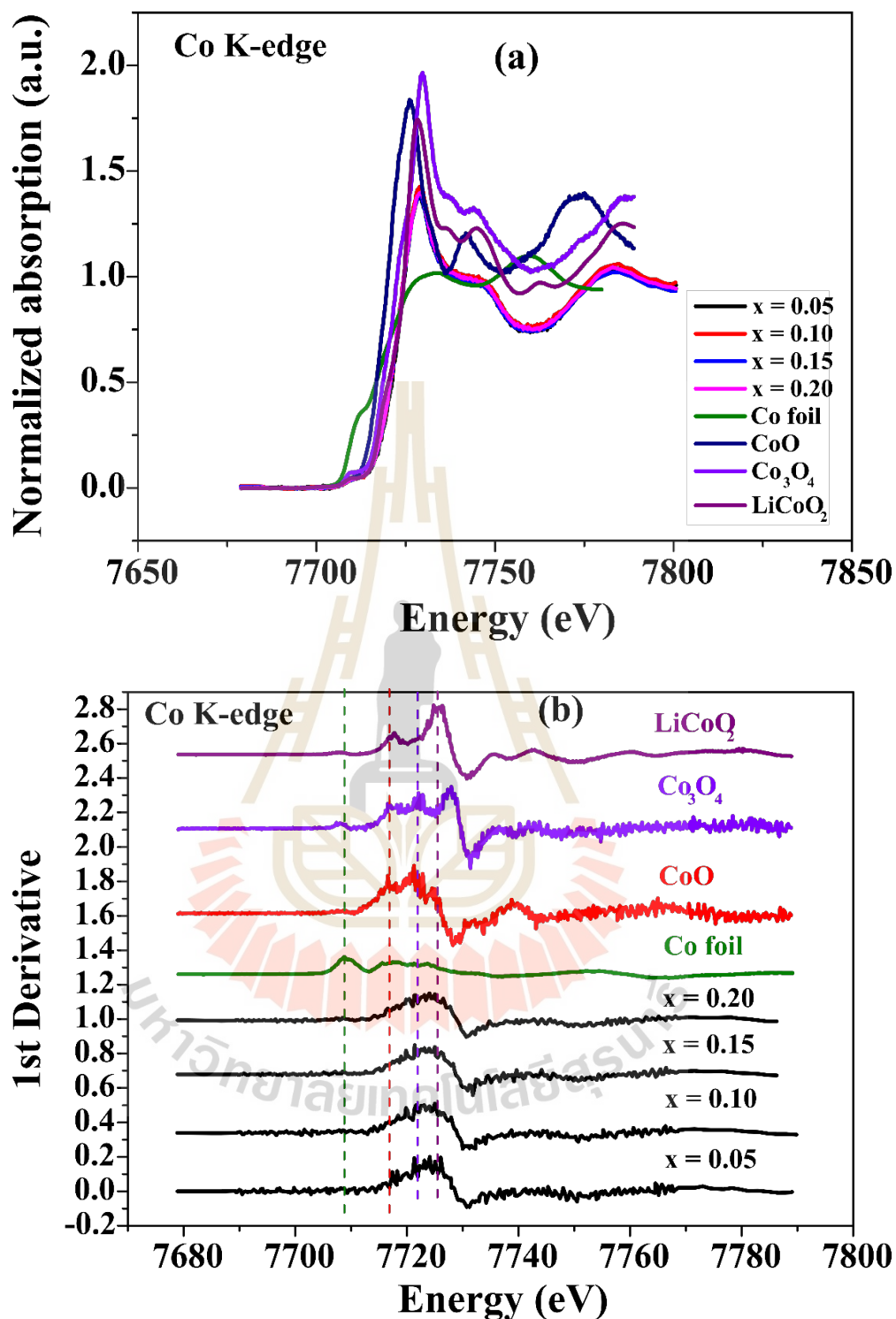


Figure 4.23 (a) Normalized XANES with (b) the first derivative plot at Co K-edge of $\text{AgFe}_{1-x}\text{Co}_x\text{O}_2$ with different concentration.

Table 4.5 Energy edge position and corresponding valence states of the reference standard and $\text{AgFe}_{1-x}\text{Co}_x\text{O}_2$ samples.

Samples	Edge element	Edge energy (E) (eV)	Oxidation state
Ag foil	Ag	3351.30	+0
Ag_2O	Ag	3349.39	+1
AgO	Ag	3348.11	+2
Fe foil	Fe	7111.65	+0
FeO	Fe	7119.89	+2
Fe_3O_4	Fe	7123.23	+2, +3
Fe_2O_3	Fe	7126.76	+3
Co foil	Co	7708.77	+0
CoO	Co	7716.84	+2
Co_3O_4	Co	7721.95	+2, +3
LiCoO_2	Co	7725.56	+3
x = 0.00	Ag	3350.48	+1
	Fe	7126.57	+3
x = 0.05	Ag	3350.87	+1
	Fe	7126.45	+3
	Co	7724.72	+3
x = 0.10	Ag	3350.63	+1
	Fe	7127.50	+3
	Co	7724.92	+3
x = 0.15	Ag	3350.29	+1
	Fe	7126.48	+3
	Co	7725.14	+3
x = 0.20	Ag	3350.56	+1
	Fe	7126.55	+3
	Co	7725.35	+3

Moreover, the XPS technique was employed to analyze the elemental composition and valence state of the Co-doped AgFeO_2 nanoparticles. For fitting the Ag 3d spectra of all the AgFeO_2 samples, the Gaussian fitting technique was employed. Figure 4.24 displays the XPS results of Ag 3d core level of all the Co-doped AgFeO_2 samples. The binding energy values of ~ 367.03 eV and ~ 373.01 eV were found for Ag $3d_{5/2}$ and Ag $3d_{3/2}$, respectively which attributes to Ag^{+1} (Mao et al., 2016; Zhou et al., 2011). According to these results, Ag in the $\text{AgFe}_{1-x}\text{Co}_x\text{O}_2$ ($x = 0.00, 0.05, 0.10, 0.15, 0.20$) nanoparticles consist the oxidation states of Ag^{+1} . In terms of the XPS spectrum of Fe 2p, the configuration of electronic of Fe atoms in the states of $2p_{3/2}$ and $2p_{1/2}$ was discerned at ~ 712 eV and ~ 725 eV binding energies, respectively, with a gap of 13 eV. Additionally, two satellite peaks (referred to as "Sat.") were observed (Figure 4.25). The presence of two main peaks at 711 eV (Fe $2p_{3/2}$) and 724 eV (Fe $2p_{1/2}$) within the AgFeO_2 delafossite samples served to confirm the oxidation state of Fe^{3+} (Ahmed et al., 2020; Yamashita and Hayes, 2008; Mills and Sullivan, 1983; Hawn and DeKoven, 1987; Muhler, Schlögl, and Ertl, 1992). For the XPS spectra of Co 2p, two main peaks were found at ~ 780 eV and ~ 795 eV (Figure 4.26) which corresponds to the Co atom electronic configuration in the Co $2p_{3/2}$ and Co $2p_{1/2}$, respectively. This shows the presence of Co^{3+} cation in the Co-doped AgFeO_2 nanoparticles (Huang et al., 2017). Through the outcomes of O 1s fitting, the main peak were identified at 531 eV which refers to lattice oxygen within the AgFeO_2 delafossite structure and the shoulder located at ~ 533 eV associating with OH^- group (Ahmed et al., 2020; Che et al., 2016) (Figure 4.27).

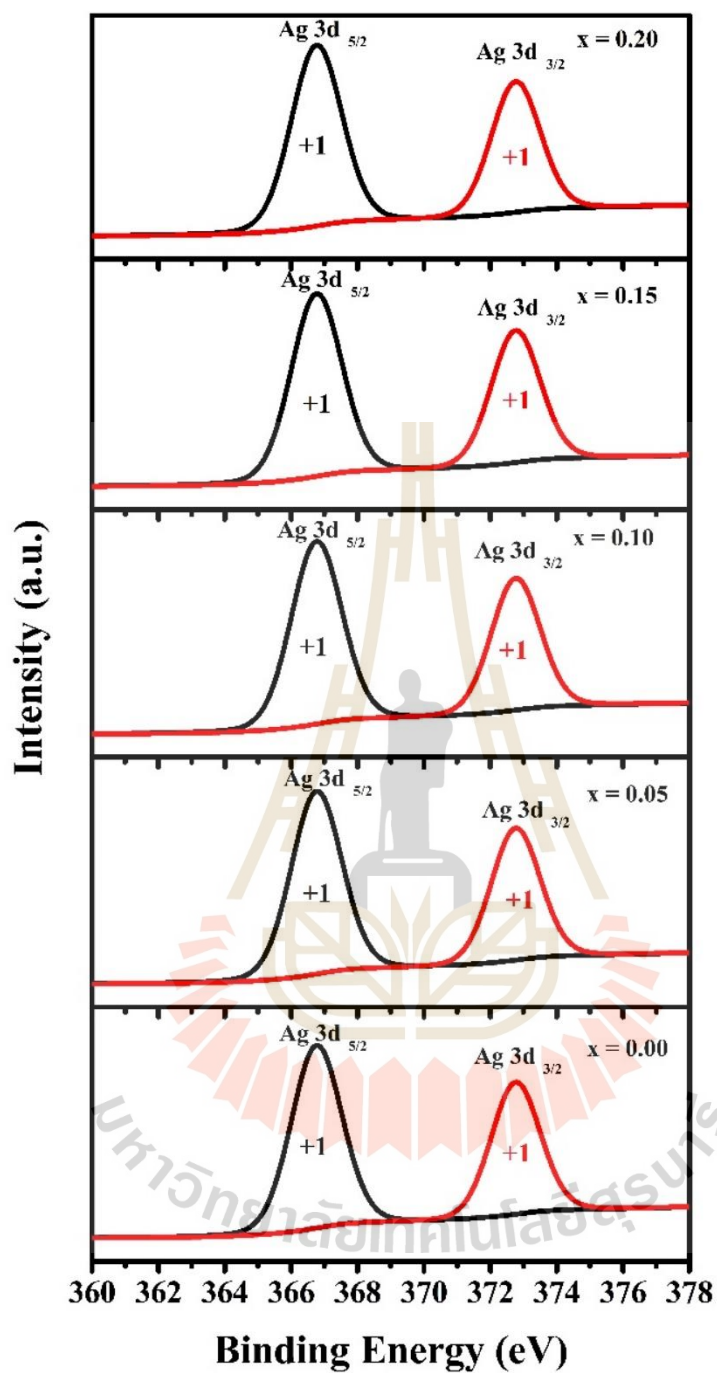


Figure 4.24 XPS spectrum of $\text{AgFe}_{1-x}\text{Co}_x\text{O}_2$ samples at Ag 3d with different Co concentrations.

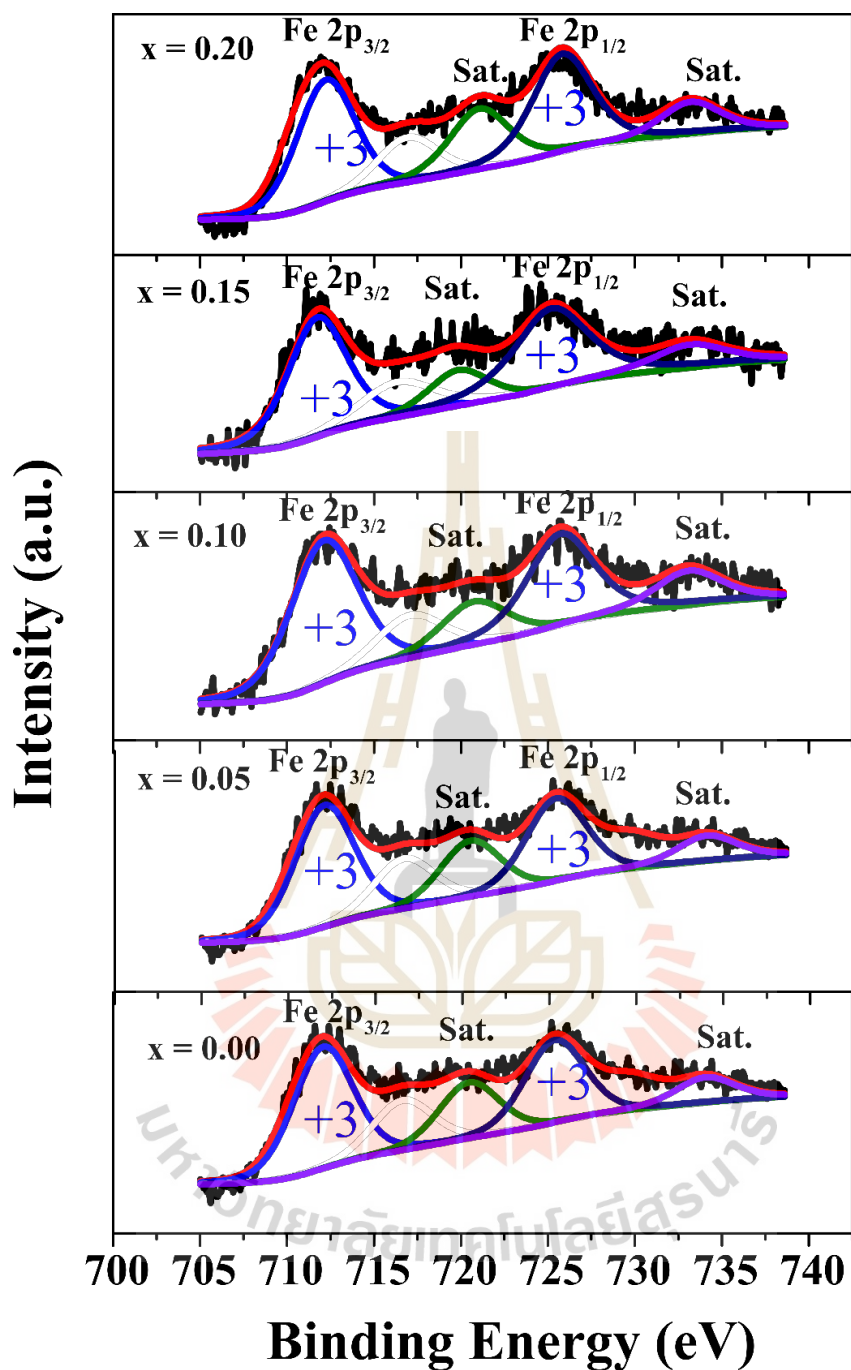


Figure 4.25 XPS spectrum of AgFe_{1-x}Co_xO₂ nanoparticles at Fe 2p with different Co concentrations.

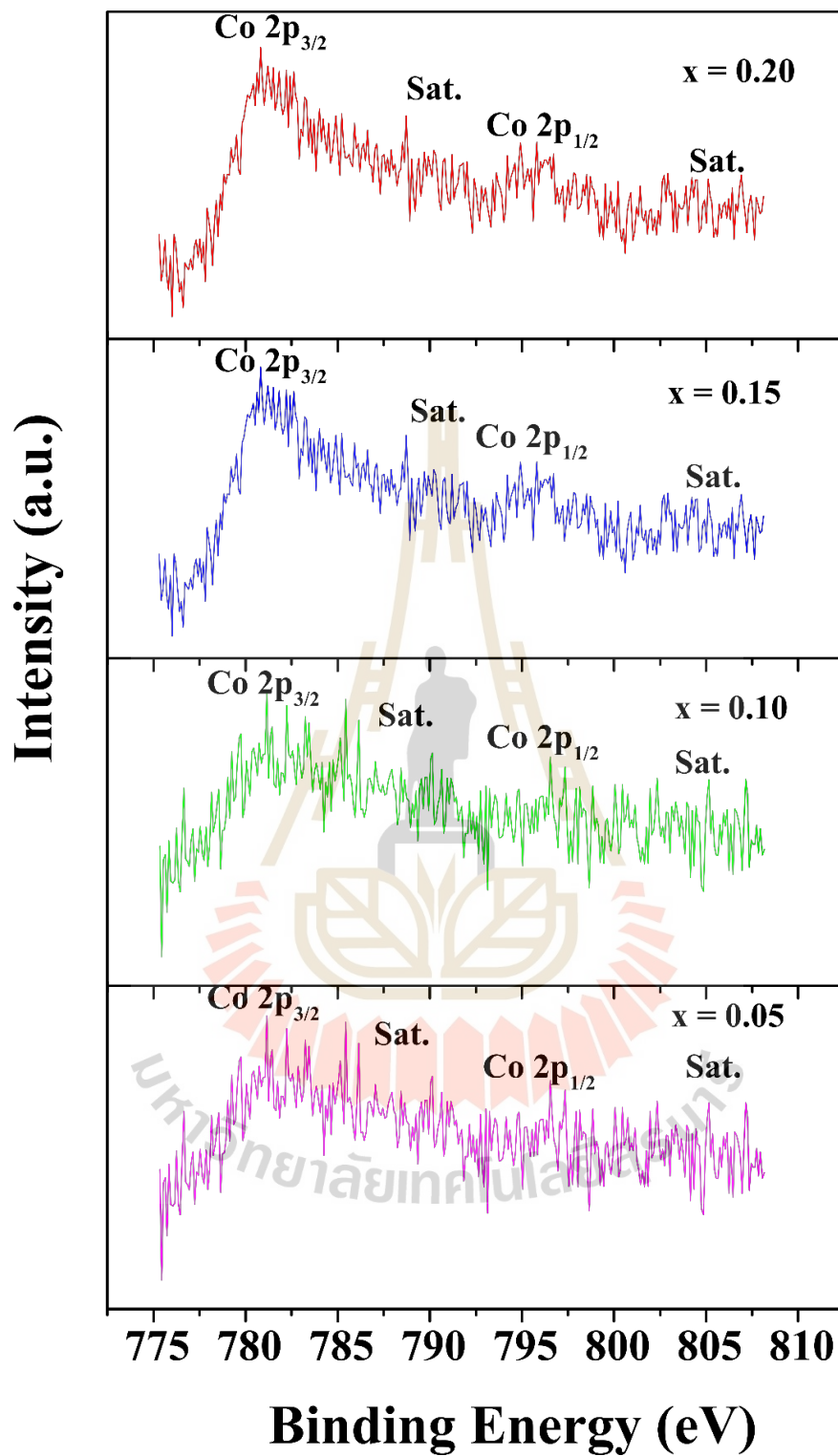


Figure 4.26 XPS spectrum of $\text{AgFe}_{1-x}\text{Co}_x\text{O}_2$ samples at Co 2p with different Co contents.

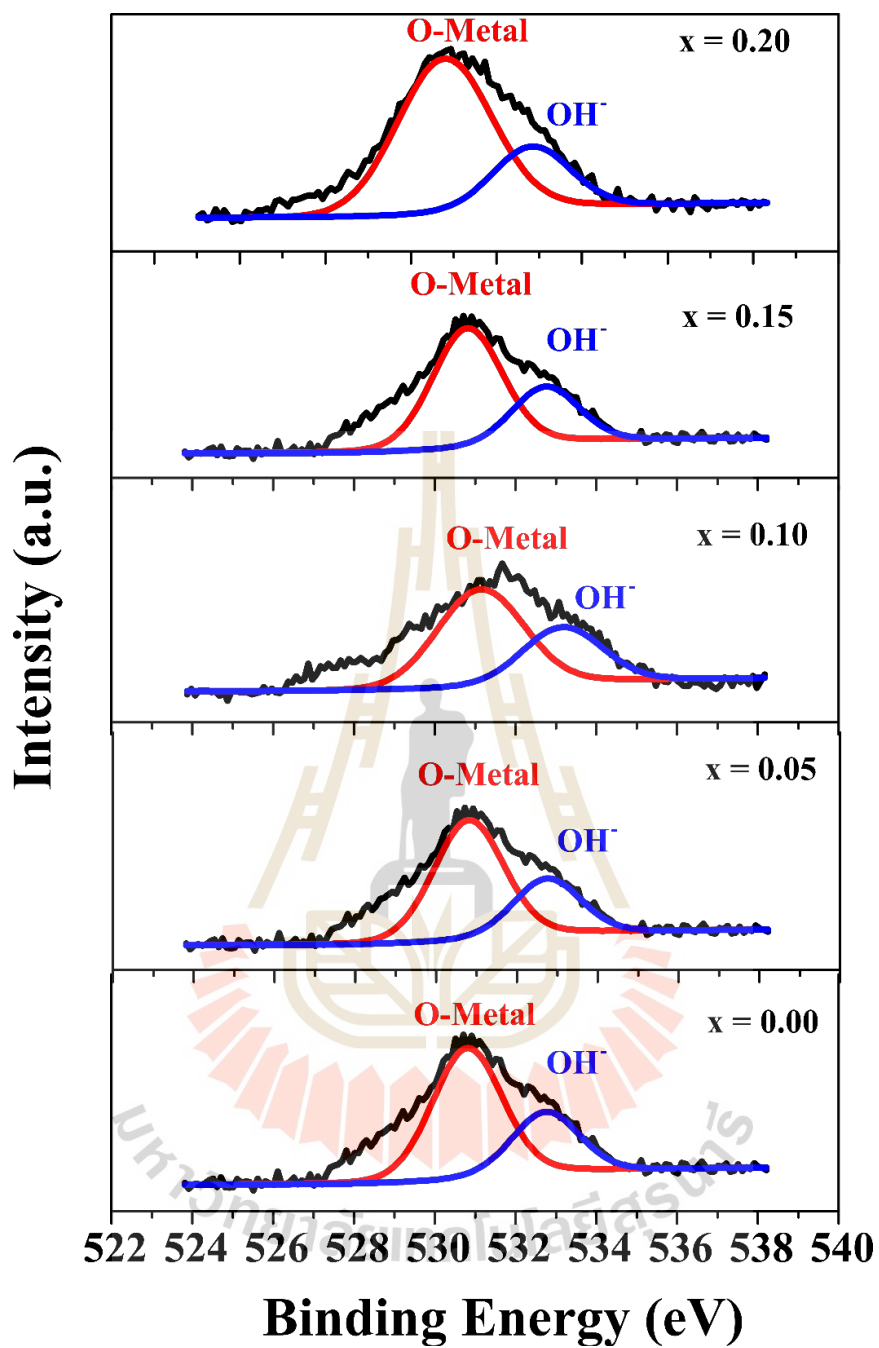


Figure 4.27 XPS spectra of $\text{AgFe}_{1-x}\text{Co}_x\text{O}_2$ samples at O 1s with various Co concentrations.

4.2.3 Surface area, pore volume and distribution of pore size study of Co-doped AgFeO₂ nanoparticles by BJH and BET methods

The BET and BJH methods were used to study the pore structure and specific surface area of the Co-doped AgFeO₂ nanoparticles with different Co content ranging from $x = 0.00$ to $x = 0.20$. Figure 4.28(a-e) represents the distribution of pore size (inset) and N₂ adsorption/desorption isotherms. The N₂ isotherms of the AgFe_{1-x}Co_xO₂ samples show the minor hysteresis loop within the 0 to 1 range, which is a characteristic indicator of a mesoporous material. According to the results of BET method, the values of BET specific surface area (S_{BET}) of 28.22, 37.94, 41.24, 85.88 and 52.29 m²/g were computed for the Co-doped AgFeO₂ sample with $x = 0.00, 0.05, 0.10, 0.15$ and 0.20 , respectively. By increasing the Co concentration from 0.00 to 0.15, the values of BET specific surface area show an upward trend, primarily because of a reduction in particles size. On the contrary, the sample containing Co at a concentration of 0.20 exhibits a reduction in specific surface area. This reduction might be attributed to the substantial aggregation of nanoparticles. As presented in Figure 4.26(a-e) (inset), the presence of the distribution of pore size spanning from 2 to 50 nm is also indicative of a characteristic trait commonly found in mesoporous materials. By using the BJH method, the samples with $x = 0.00, 0.05, 0.10, 0.15$ and 0.20 show the values of mean pore size (D_{avg}) of 18.95, 14.37, 12.90, 11.23 and 12.94 nm, respectively. The results of the pore volume (V_{BJH}), specific surface, and the distribution of pore size analysis are listed in Tables 4.5. According to these results, it reveals that the Co concentration affects the porosity properties of delafossite AgFeO₂ nanoparticles which might be resulted in their electrochemical performance.

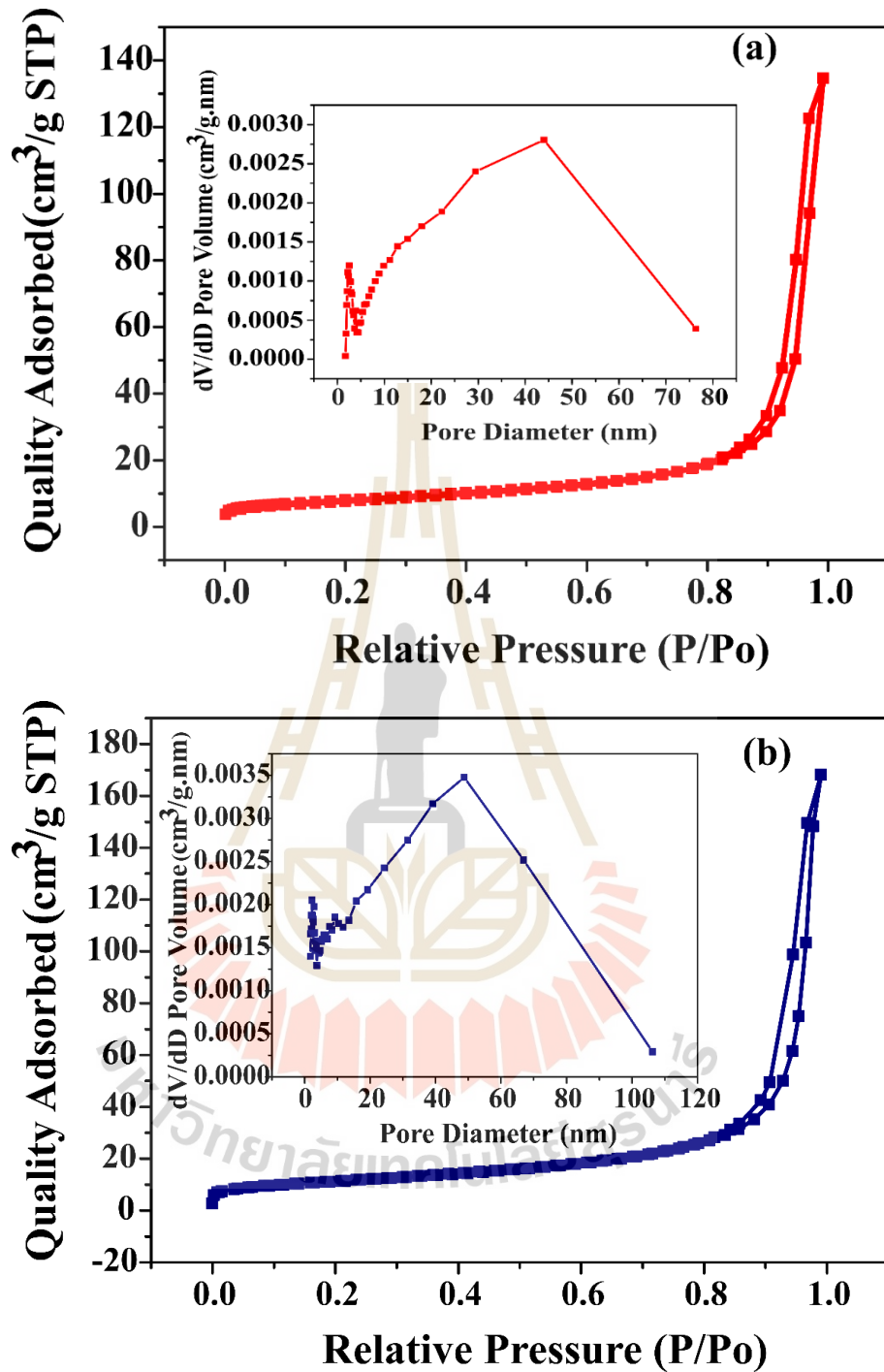


Figure 4.28 The pore size distribution (inset) and N_2 adsorption-desorption isotherms and of $AgFe_{1-x}Co_xO_2$ with (a) $x = 0.00$, (b) $x = 0.05$, (c) $x = 0.10$, (d) $x = 0.15$ and (e) $x = 0.20$.

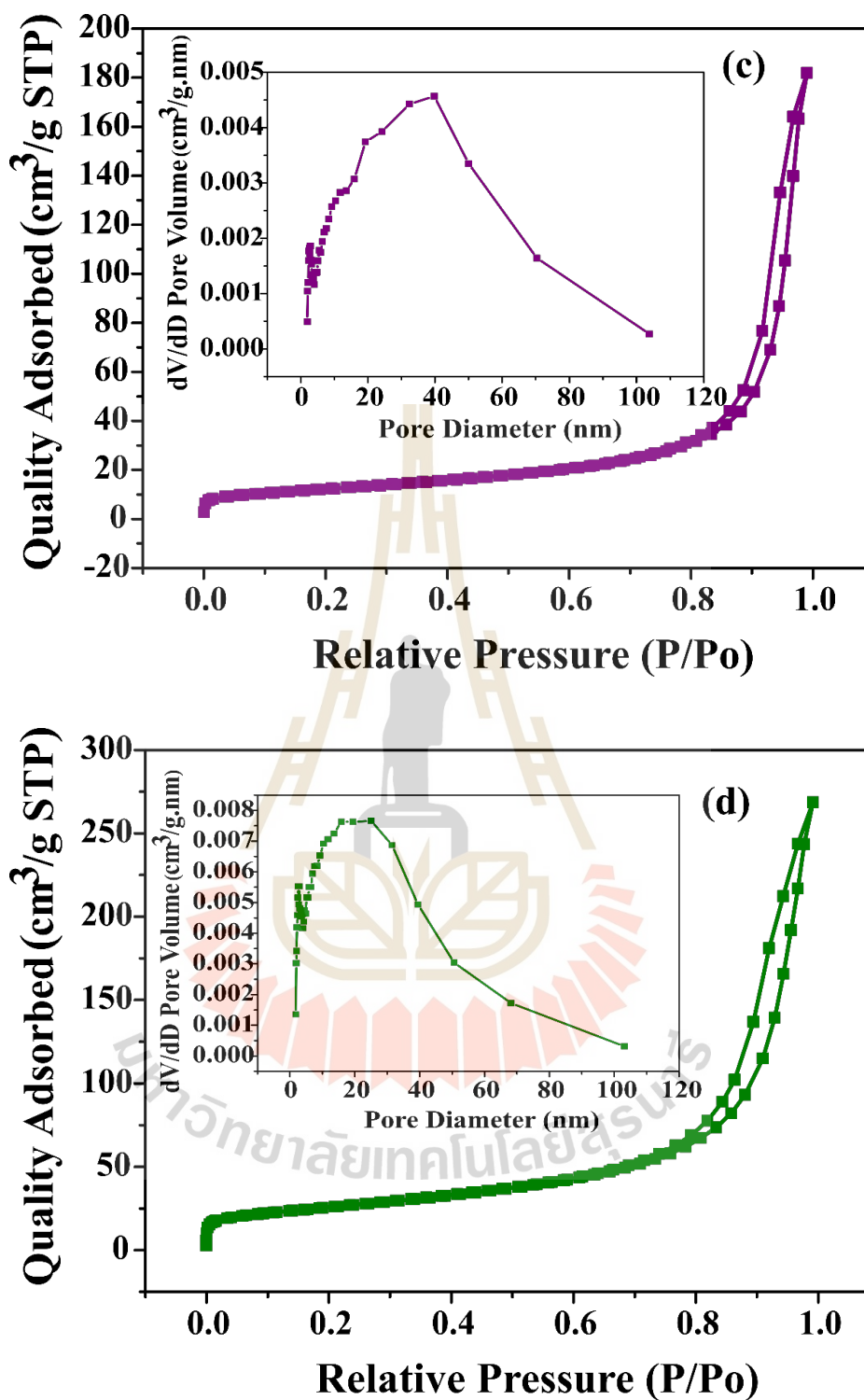


Figure 4.28 (Continued) The pore size distribution (inset) and N_2 adsorption-desorption isotherms and of $AgFe_{1-x}Co_xO_2$ with (a) $x = 0.00$, (b) $x = 0.05$, (c) $x = 0.10$, (d) $x = 0.15$ and (e) $x = 0.20$.

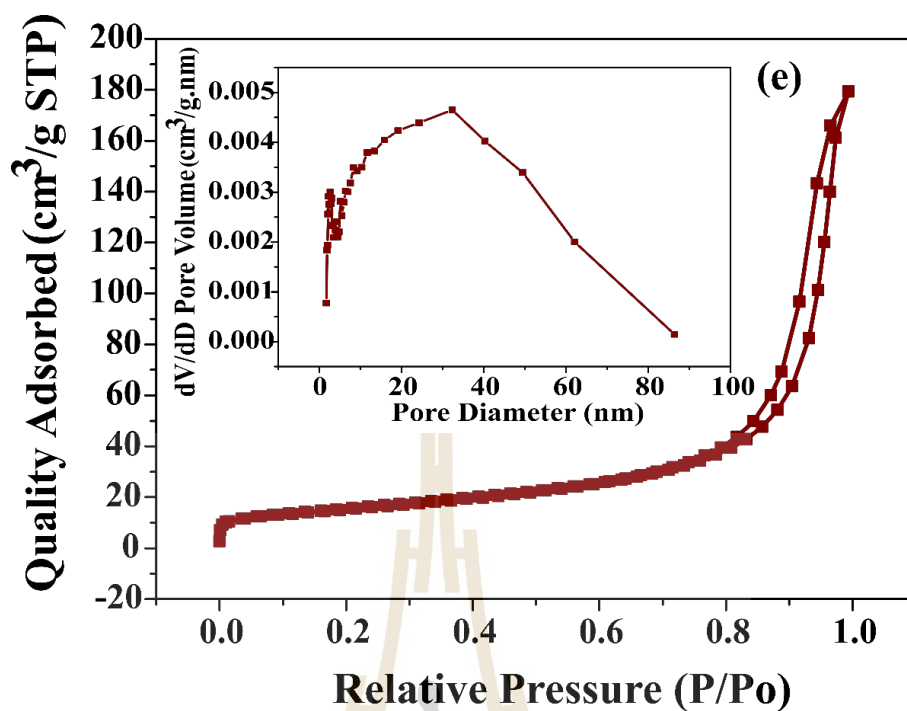


Figure 4.28 (Continued) The pore size distribution (inset) and N_2 adsorption-desorption isotherms and of $AgFe_{1-x}Co_xO_2$ with (a) $x = 0.00$, (b) $x = 0.05$, (c) $x = 0.10$, (d) $x = 0.15$ and (e) $x = 0.20$.

Table 4.6 The values of specific surface area, pore volume and pore size of the $AgFe_{1-x}Co_xO_2$

Condition	S_{BET} (m^2/g)	V_{BJH} (cm^3/g)	D_{avg} (nm)
$x = 0.00$	28.22	0.134	18.95
$x = 0.05$	37.94	0.170	14.37
$x = 0.10$	41.24	0.215	12.94
$x = 0.15$	85.88	0.344	11.23
$x = 0.20$	52.29	0.234	12.90

4.2.4 Electrochemical performance of Co-doped $AgFeO_2$ nanoparticles

4.2.4.1 Cyclic voltammetry performance

The electrochemical behavior and specific capacitance value of the Co-doped $AgFeO_2$ electrode were studied by the technique of CV. As displayed in Figure

4.29(a-e), the window of potential range between -1.16 V to 3.5 V was used in the CV performance of the $\text{AgFe}_{1-x}\text{Co}_x\text{O}_2$ electrode with the ranging from 2 mV/s to 100 mV/s various scan rates in 3M KOH electrolyte. The CV results of all the $\text{AgFe}_{1-x}\text{Co}_x\text{O}_2$ electrodes exhibit redox peaks, suggesting that the observed pseudocapacitor behavior is a result of faradaic redox reactions involving Ag/Ag^+ , $\text{Fe}^{2+}/\text{Fe}^{3+}$ and $\text{Co}^{2+}/\text{Co}^{3+}$, consistent with prior reports (Wongpratad et al., 2020; Pai et al., 2018; Tang et al., 2020). The equations below elucidate the reversible redox reaction involving the transformation between Ag and Ag^+ , Fe^{2+} and Fe^{3+} and Co^{2+} and Co^{3+} in oxidative processes:



or



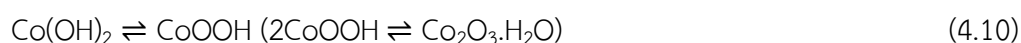
or



And



or



The position of the cathodic and anodic peaks of the curves of CV technique shifts with increasing the scan rate. This demonstrates good high-rate performance and excellent electrochemical reversibility of the material's electrode. The calculated values of specific capacitance of the $\text{AgFe}_{1-x}\text{Co}_x\text{O}_2$ sample are exhibited Figure 4.29(f) at the various scan rates ranging from 2 to 100 mV/s. The high values of specific capacitance of 358.32, 372.64, 386.80, 396.96 and 388.89 F/g were calculated for the $\text{AgFe}_{1-x}\text{Co}_x\text{O}_2$ with different concentration of $x = 0.00, 0.05, 0.10,$

0.15 and 0.20, respectively, at a low scan rate of 2 mV/s. As the scan rates is raised from 2 to 100 mV/s, the calculated specific capacitance values of all the samples declines. This decline occurs because at the higher scan rates, ion becomes restricted mainly to the electrode's surface, thereby dominating EDLCs characteristics over pseudocapacitive characteristics. The specific capacitance value shows an upward trend with various Co concentrations from 0.05 to 0.15, followed by a decline at $x = 0.20$. This pattern can be attributed to the increase in total pore volume and BET specific surface area in the samples from 0.05 to 0.15, resulting in a greater number of active sites conductive to faradaic redox reactions (Zhu et al., 2014; Padmanathan and Selladurai, 2014). However, this trend reverses for the Co content with $x = 0.20$ where both the BET specific surface area and pore volume decrease leading to a reduced number of the active sites for these reasons.

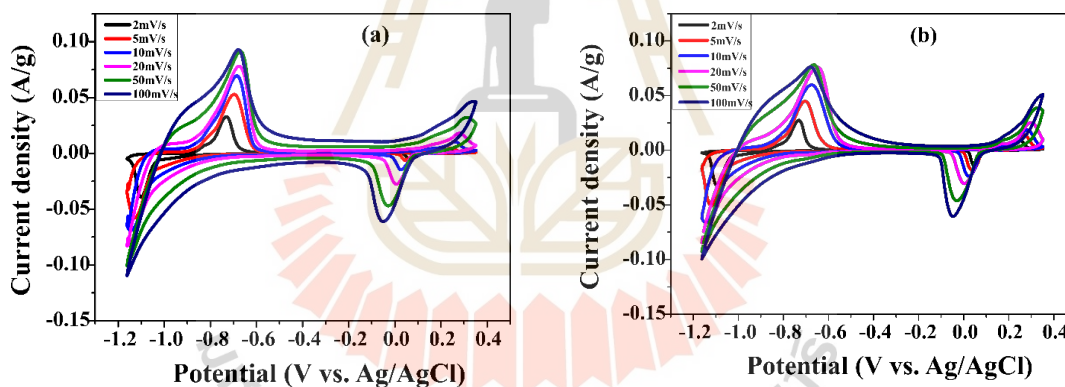


Figure 4.29 CV curves of Co-doped AgFeO_2 nanoparticles at different scan rates with (a) $x = 0.00$, (b) $x = 0.05$, (c) $x = 0.10$, (d) $x = 0.15$, (e) $x = 0.20$, and (f) The values of calculated specific capacitance.

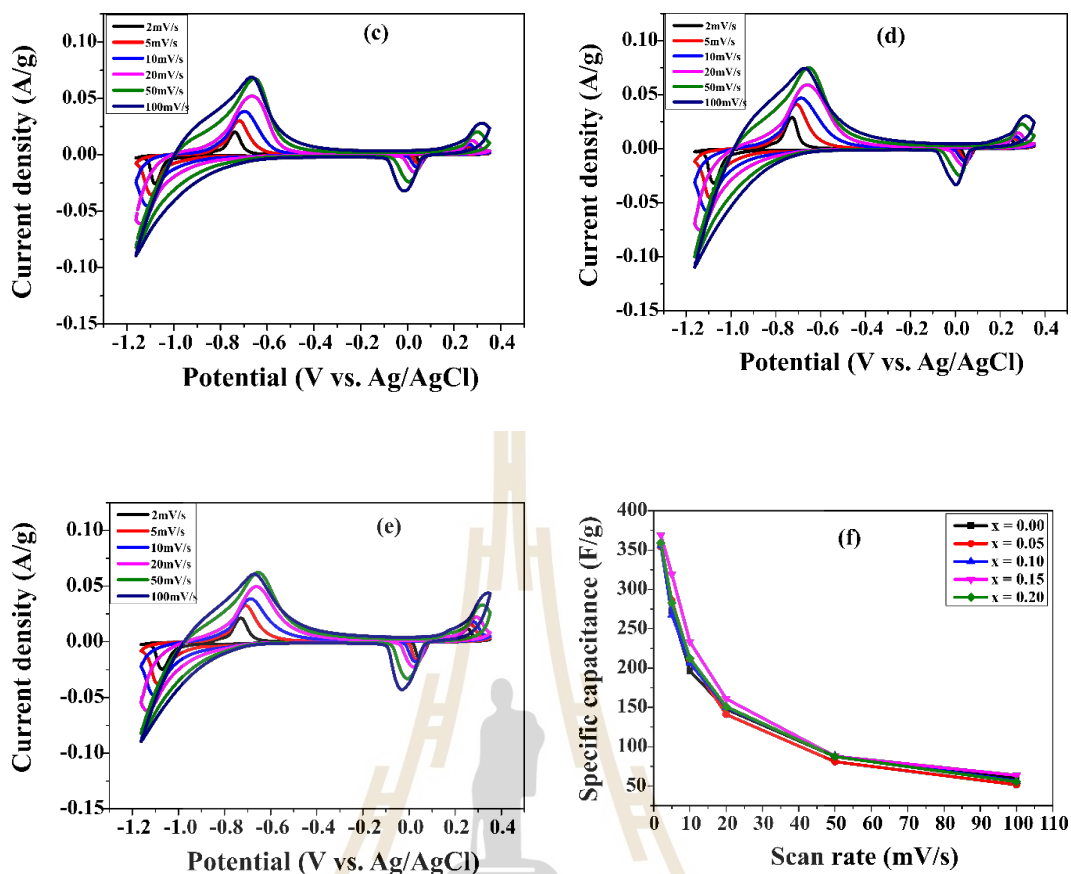


Figure 4.29 (Continued) CV curves of Co-doped AgFeO_2 nanoparticles at different scan rates with (a) $x = 0.00$, (b) $x = 0.05$, (c) $x = 0.10$, (d) $x = 0.15$, (e) $x = 0.20$, and (f) The values of calculated specific capacitance.

4.2.4.2 Galvanostatic charge discharge measurement

In Figure 4.30(a-e), it presents the results of galvanostatic charge-discharge (GCD) technique for the $\text{AgFe}_{1-x}\text{Co}_x\text{O}_2$ nanoparticles at the various current densities ranging from 1 to 20 A/g under the potential between 1.16 V to 3.5 V in a 3M KOH solution. The GCD curves for all the samples demonstrate a pseudocapacitive behavior, consistent with the observation from CV measurement. The GCD test discharge curves were employed to assess the specific capacitance values for the $\text{AgFe}_{1-x}\text{Co}_x\text{O}_2$ electrode. Figure 4.30(f) displays the computed specific capacitance values for all the synthesized samples. It is evident from the figure that as the current density rises, there is a corresponding decrease in the value of specific

capacitance. This phenomenon can be ascribed to an increase in the internal polarization and resistance of the $\text{AgFe}_{1-x}\text{Co}_x\text{O}_2$ samples. At a 1 A/g current density, the values of specific capacitance of 229.71, 230.89, 233.36, 284.04 and 233.11 F/g were discovered for the Co-doped AgFeO_2 with Co concentration of $x = 0.00, 0.05, 0.10, 0.15,$ and 0.20 respectively. Table 4.6 lists the specific capacitance at various current density. This trend aligns with the specific capacitance values calculated from the cyclic voltammetry measurement. Notably, the highest specific capacitance value of 284.04 F/g was observed for sample with $x = 0.15$ which featured the highest value of BET specific surface area resulting in the reach active sites for faradiac reversible redox reactions.

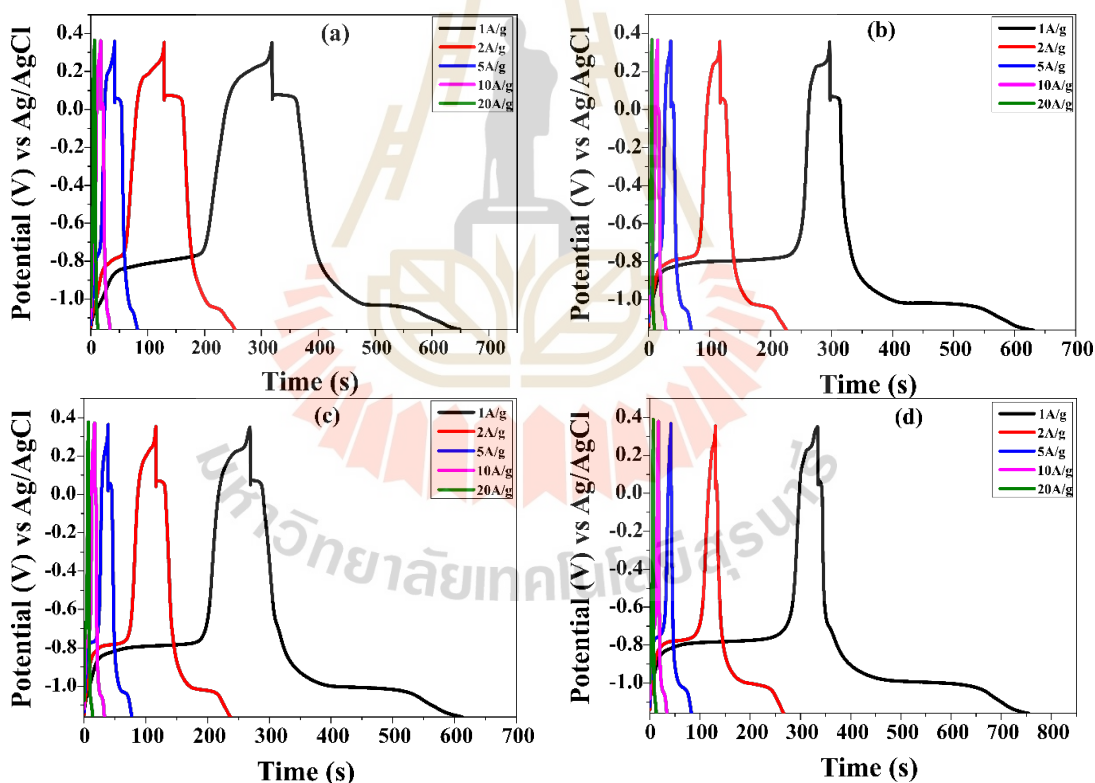


Figure 4.30 GCD plot of Co-doped AgFeO_2 nanoparticles with (a) $x = 0.00$, (b) $x = 0.05$, (c) $x = 0.10$, (d) $x = 0.15$, (e) $x = 0.20$, and (f) the specific capacitance values at various current densities.

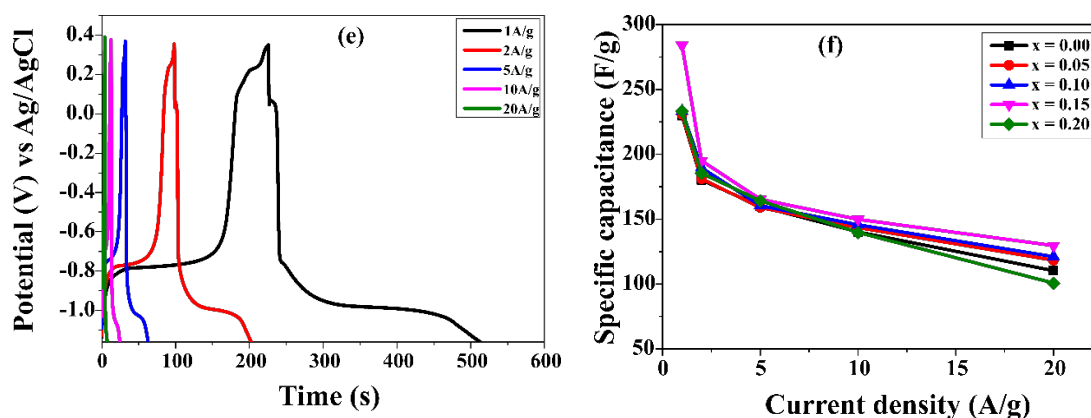


Figure 4.30 (Continued) GCD curves of Co-doped AgFeO₂ nanoparticles with (a) $x = 0.00$, (b) $x = 0.05$, (c) $x = 0.10$, (d) $x = 0.15$, (e) $x = 0.20$ and (f) the specific capacitance values at various current densities.

Table 4.7 List of the specific capacitance values of Co-doped AgFeO₂ nanoparticles where Co concentrations of $x = 0.00$, 0.05 , 0.10 , 0.15 and 0.20 calculated employing GCD technique.

Current density (A/g)	Specific capacitance at various Co concentrations (F/g)				
	$x = 0.00$	$x = 0.05$	$x = 0.10$	$x = 0.15$	$x = 0.20$
1	229.71	230.89	233.36	284.04	233.11
2	180.17	181.10	189.62	195.06	185.45
5	159.87	158.94	160.42	165.35	164.09
10	140.20	143.42	145.60	149.79	139.75
20	110.28	118.35	121.13	129.63	100.67

Furthermore, the durability of the Co-doped AgFeO₂ nanoparticles was conducted through a continuous 1000 cycles charge-discharge experiment which assessed at a 5 A/g current density. However, In Figure 4.31, the capacity retention of the AgFe_{1-x}Co_xO₂ electrode is presented after completing 1000 charge-discharge cycles. The results reveal that the AgFe_{1-x}Co_xO₂ samples with different concentration

of $x = 0.00, 0.10, 0.15$ and 0.20 display the retention of capacitance values of 82.99, 83.75, 83.85, 84.19 and 83.17%, respectively. This result indicates that the $\text{AgFe}_{0.85}\text{Co}_{0.15}\text{O}_2$ electrode exhibits superior capacitance and improved rate capability.

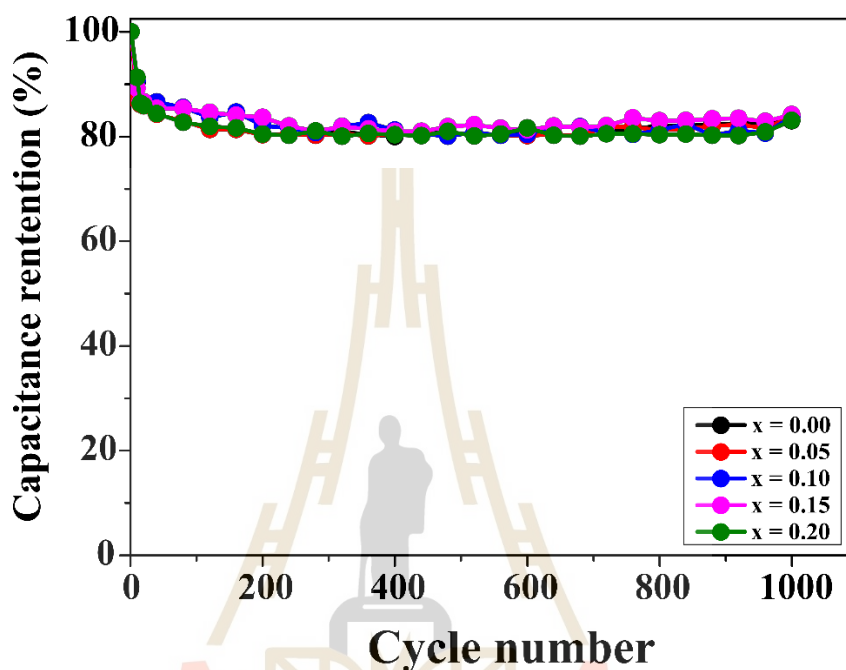


Figure 4.31 Capacitance retention (%) of $\text{AgFe}_{1-x}\text{Co}_x\text{O}_2$ electrodes with Co concentrations spanning from $x = 0.00$ to 0.20 .

4.2.4.3 Electrochemical impedance spectroscopy study

The study involved the electrical conducting property of the electrode, EIS experiment within a frequency rang spanning from 10 mHz to 1000 KHz, while maintaining a potential of 10 mV were studies. In the region of high-frequency, the EIS curve for all the Co-doped AgFeO_2 nanoparticles exhibit an incomplete semicircle pattern, as depicted in Figure 4.32. This pattern is indicative of resistance at the interface between the electrolyte and the oxide. Specifically, at high frequency, the point where the curve intersects the real axis (Z') correspond to the solution resistance (R_s) or equivalent resistance (R_{esr}). For the $\text{AgFe}_{1-x}\text{Co}_x\text{O}_2$ samples with

the contents of $x = 0.00, 0.05, 0.10, 0.15$ and 0.20 , respective solution resistance (R_s) values of $1.24, 1.21, 1.19, 1.15$ and 1.18Ω were obtained. Conversely, the charge transfer resistance (R_{ct}) is represented by the diameter of the semicircle. Additionally, the stopping line in the low frequency range suggests the presence of Warburg impedance (W), indicating the diffusion of electrolyte ions within the electrode material. Based on the Nyquist plots, it was observed that all the Co-doped AgFeO_2 samples show the low charge transfer resistance (R_{ct}) value, as evidenced by the small semicircles in the middle-frequency range. Notably, the sample with $x = 0.15$ displayed the lowest solution resistance (R_s) value. which suggests that $\text{AgFe}_{0.85}\text{Co}_{0.15}\text{O}_2$ nanoparticles have potential utility as electrode material in energy storage device.

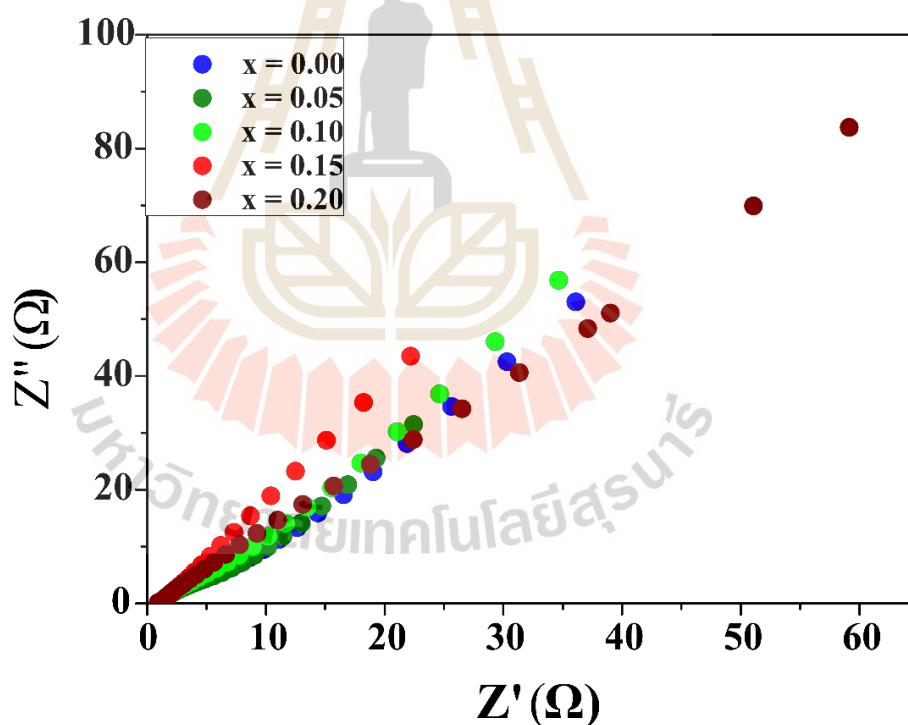


Figure 4.32 EIS curves of Co-doped AgFeO_2 nanoparticles with different Co contents.

4.2.4.4 Specific energy and specific power study

Energy storage device performance is commonly evaluated using the Ragone plot, which visually represents the relationship between specific energy and specific power. This approach is widely accepted for gauging their efficiency. Across various current densities ranging from 1 to 20 A/g, it is evident that specific energies seem to increase with raising the Ni concentrations from 0.00 to 0.15. As demonstrated in Figure 4.33, the specific energies and specific power values of Co-doped AgFeO_2 nanoparticles obtained were as follows: at $x = 0.00$, 72.74 Wh/Kg and 797.46 W/Kg; at $x = 0.05$, 73.12 Wh/Kg and 787.52 W/Kg; at $x = 0.10$, 73.90 Wh/Kg and 769.57 W/Kg; at $x = 0.15$, 89.95 Wh/Kg and 769.47 W/Kg; and at $x = 0.20$, 73.82 Wh/Kg and 785.93 W/Kg, all at 1 A/g current density.

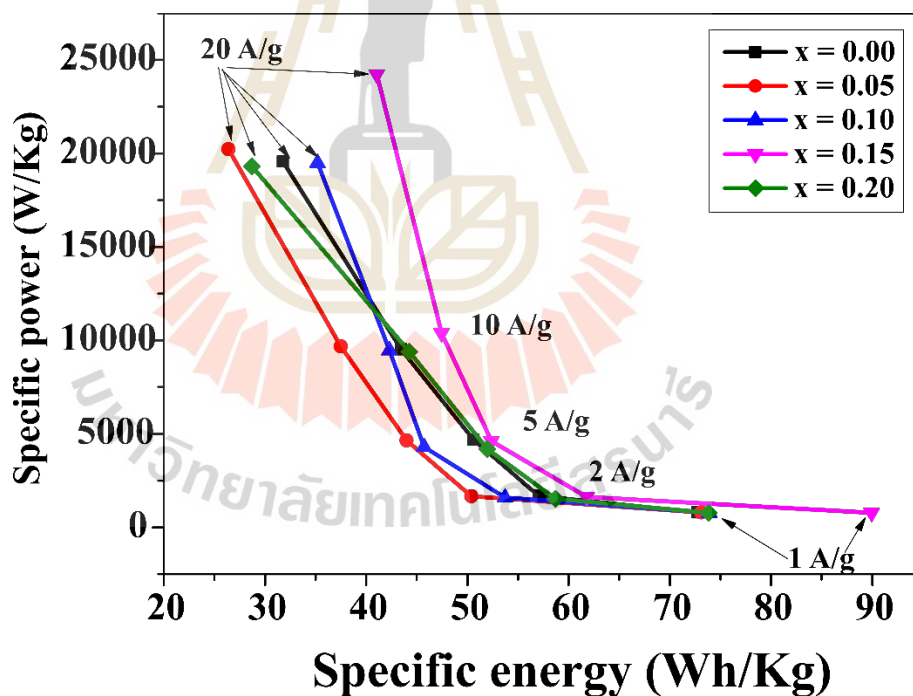


Figure 4.33 Specific energies and corresponding specific power of Co-doped AgFeO_2 nanoparticles at current densities of 1, 2, 5, 10 and 20 A/g.

4.3 Ni-doped AgFeO₂ nanoparticles

4.3.1 Structure and morphologies analysis of the Ni-doped AgFeO₂ nanoparticles by XRD, TEM and SEM

X-ray diffraction (XRD) patterns of the AgFe_{1-x}Ni_xO₂ nanoparticles with $x = 0.00, 0.05, 0.10, 0.15$ and 0.20 are illustrated in Figure 4.34. After comparing the acquired pattern with the reference standard in the database for both hexagonal polytype 2H (PDF2 No: 00-029-1141) and the rhombohedral 3R (PDF2 No: 00-018-1175), it was verified that a mixture of both phases has been successfully achieved. The successful replacement of Fe ions with Ni ions in the delafossite structure is affirmed by the absence of NiO oxide. However, since we utilize Nickel (II) nitrate as the raw material in the synthesis process, we hypothesize that, in our specific situation, trivalent Fe ions were substituted by divalent Ni ions.

Moreover, the structures and morphologies of the Ni-doped AgFeO₂ with different concentrations of Ni were examined by TEM and FESEM. Figure 4.35(a-e) displays field-emission scanning electron microscopy (FESEM) images of all the Ni-doped AgFeO₂ nanoparticles which shows the agglomeration between the nanoparticles with flower-like microarchitecture. These images illustrate that the synthesized AgFe_{1-x}Ni_xO₂ samples with $x = 0.00, 0.05, 0.10, 0.15$ and 0.20 exhibit the mean size of particle values of 45, 28, 23, 20 and 27 nm, respectively. Observing the trend, it becomes apparent that as the concentration of Ni doping increases, the average particle size notably diminishes. Figure 4.36(a-o) presents the images of TEM with the associating selected area electron diffraction and HRTEM images of Ni-doped AgFeO₂ samples. TEM bright field images demonstrate the average particle size in nanometer range. However, the selected area electron diffraction patterns show ring with spotty, which strongly indicate the nature of polycrystalline of delafossite AgFeO₂ sample. This observation is associated with XRD results. Additionally, HRTEM images attributes to the d-spacing values of 0.229, 0.227, 0.225, 0.216 and 0.219 nm for AgFe_{1-x}Ni_xO₂ samples with various Ni content of $x = 0.00, 0.05, 0.10, 0.15$ and 0.20 , respectively.

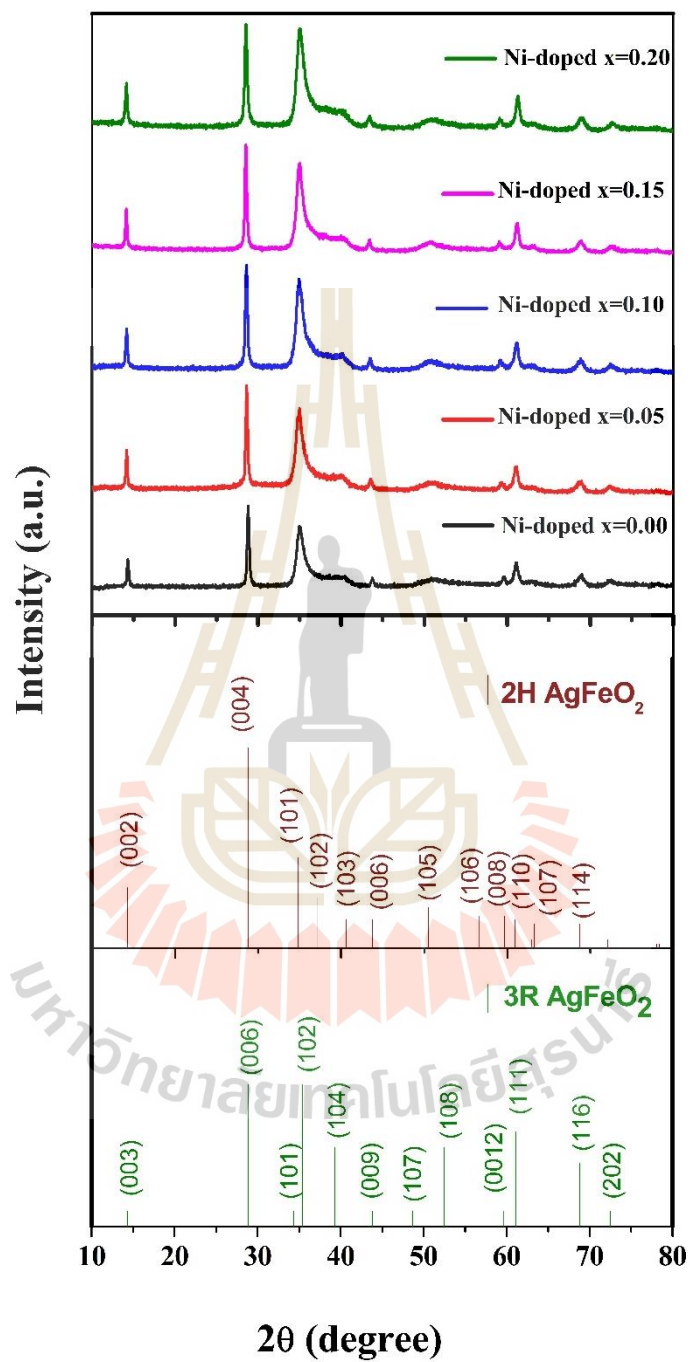


Figure 4.34 XRD patterns of $\text{AgFe}_{1-x}\text{Ni}_x\text{O}_2$ nanostructures with various Ni concentrations.

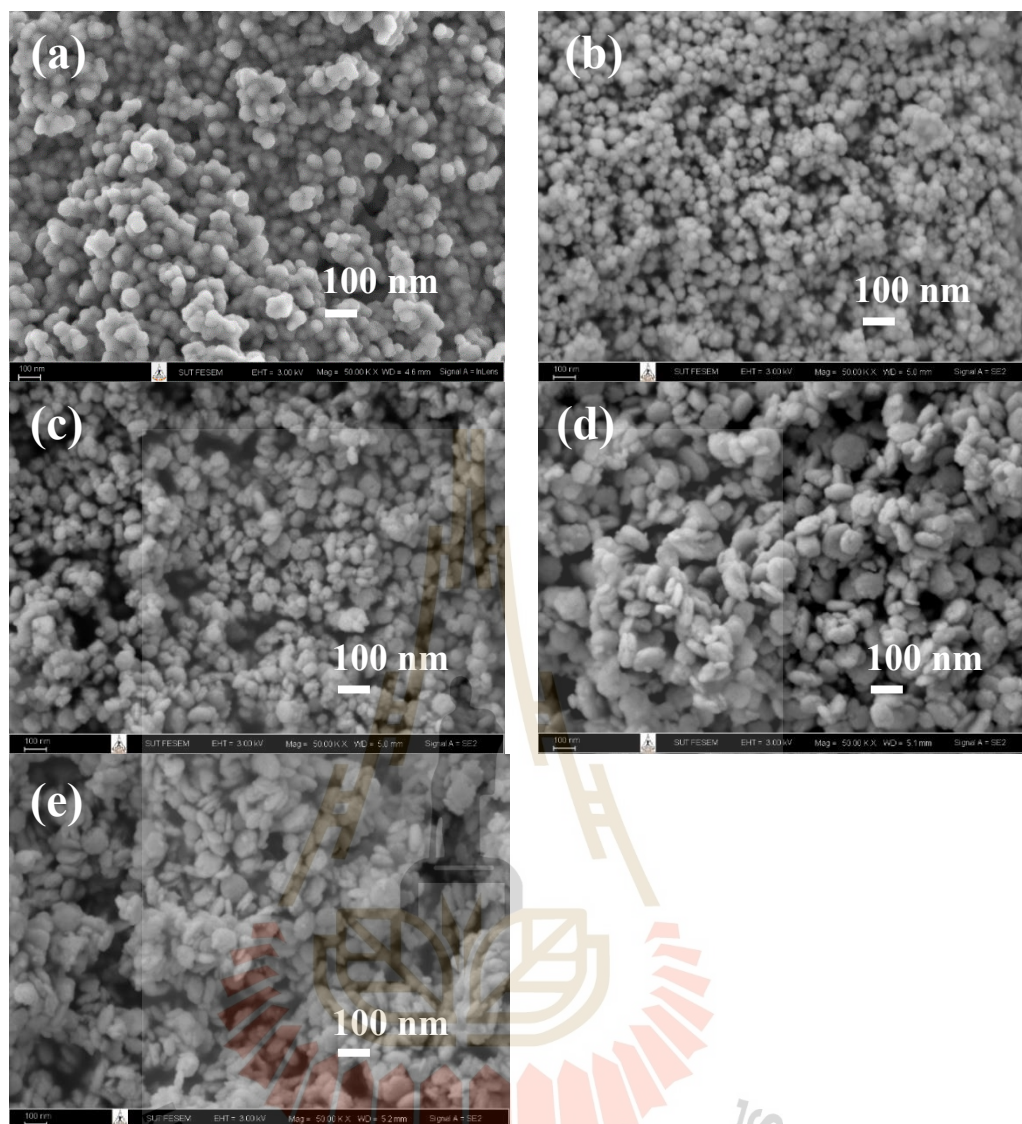


Figure 4.35 The images of FESEM of $\text{AgFe}_{1-x}\text{Ni}_x\text{O}_2$ samples: (a) $x = 0.00$, (b) $x = 0.05$, (c) $x = 0.10$, (d) $x = 0.15$ and (e) $x = 0.20$.

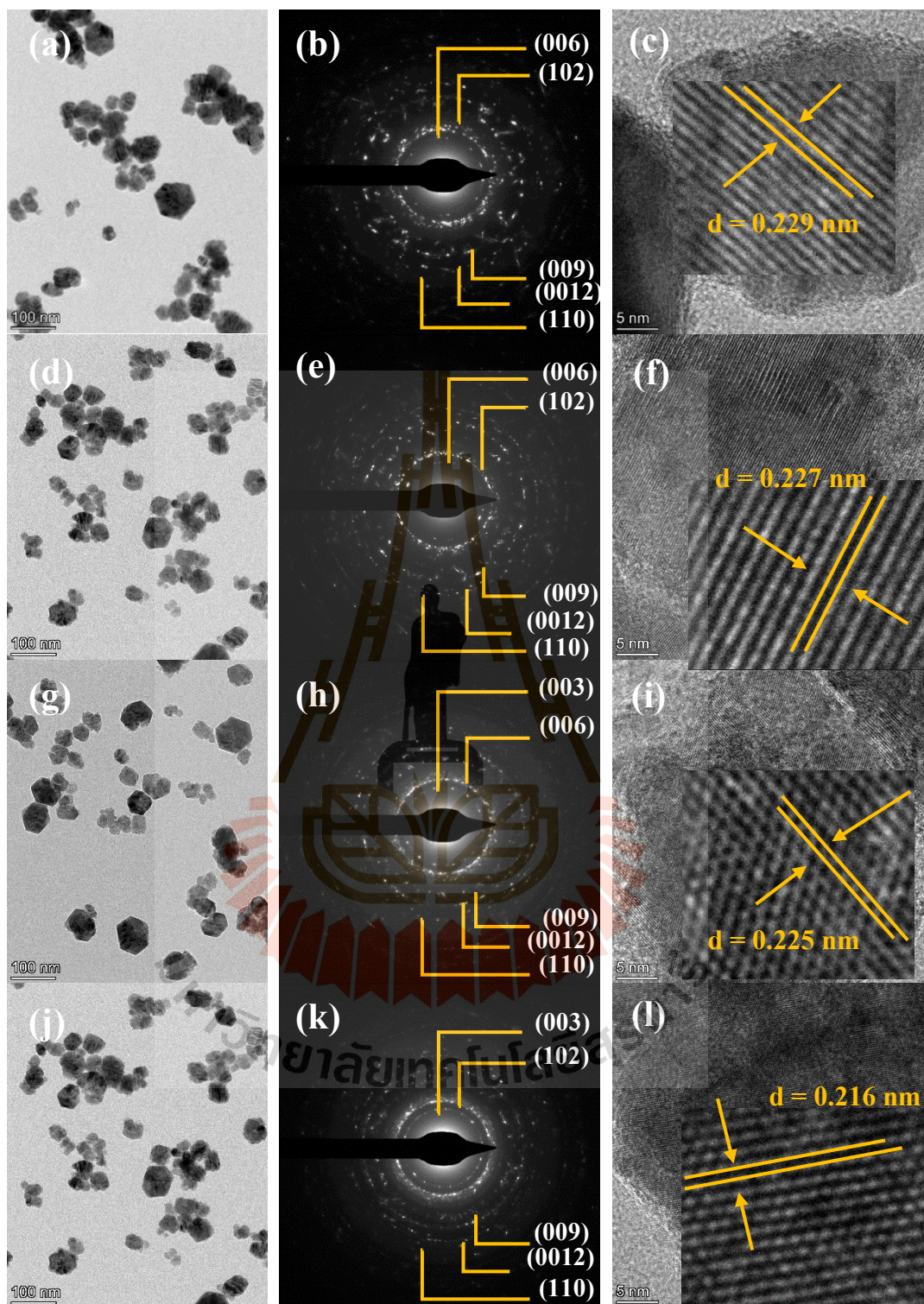


Figure 4.36 TEM images and associating SAED of $\text{AgFe}_{1-x}\text{Ni}_x\text{O}_2$ nanoparticle: (a,b,c)

$x = 0.00$, (d,e,f) $x = 0.05$, (g,h,i) $x = 0.10$, (j,k,l) $x = 0.15$ and (m,n,o) $x = 0.20$.

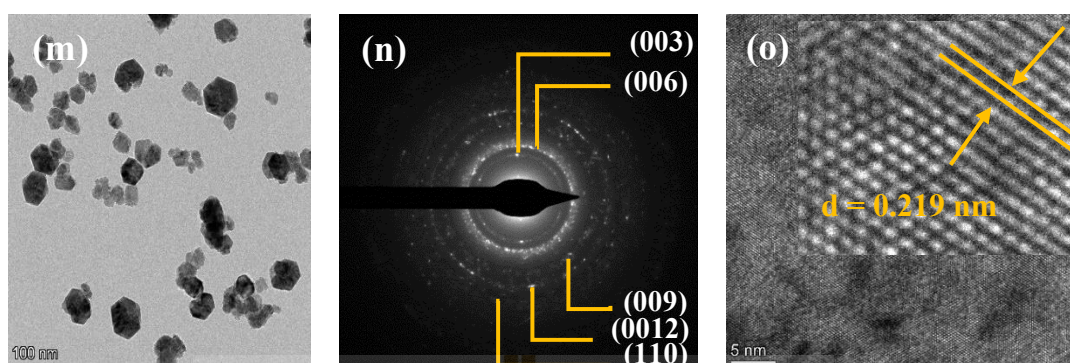


Figure 4.36 (Continued) TEM images and associating SAED of $\text{AgFe}_{1-x}\text{Ni}_x\text{O}_2$ nanoparticle: (a,b,c) $x = 0.00$, (d,e,f) $x = 0.05$, (g,h,i) $x = 0.10$, (j,k,l) $x = 0.15$ and (m,n,o) $x = 0.20$.

4.3.2 Oxidation state and surface chemical composition study of Ni-doped AgFeO_2 nanoparticles by XAS and XPS

The Ag, Fe, and Ni oxidation states in the $\text{AgFe}_{1-x}\text{Ni}_x\text{O}_2$ with various concentration of Ni were computed by the technique of X-ray absorption near edge structure (XANES). To accomplish this, XANES spectra obtained from reference samples including Ag foil (Ag^0), Ag_2O (Ag^+), AgO (Ag^{2+}), Fe foil (Fe^0), FeO (Fe^{2+}), Fe_2O_3 (Fe^{3+}), Ni foil and NiO (Ni^{2+}) were employed for the analysis of the $\text{AgFe}_{1-x}\text{Ni}_x\text{O}_2$ nanoparticles with $x = 0.00, 0.05, 0.10, 0.15$ and 0.20 . Essentially, the oxidation states of Ag, Fe and Ni can be identified by their observing shift of the edge position. The spectra of normalized XANES and the associating first derivative at the Ag L3-edge, Ni K-edge and Fe K-edge are presented in figure 4.37(b), 4.38(a,b) and 4.39(a,b), respectively. For the normalized XANES plot at the Ag L3-edge of the Ni-doped AgFeO_2 samples, it was observed that their edge position fell similarly to the standard samples of Ag_2O (Ag^+). This findings indicate that in the Ni-doped AgFeO_2 samples, silver (Ag) exists with an +1. However, the normalized XANES spectra with the corresponding first derivative at Fe K-edge reveals that the edge position closely resembled that of the reference sample Fe_2O_3 (Fe^{3+}), certifying that the iron ions oxidation state in the Ni-doped AgFeO_2 nanoparticles is +3. When examining at Ni K-

edge XANES spectra of all the prepared $\text{AgFe}_{1-x}\text{Ni}_x\text{O}_2$, the normalized spectra showed edge position shift to higher energy than the reference sample NiO (Ni^{2+}), suggesting that the Ni ions oxidation state in the Ni-doped AgFeO_2 nanoparticles is more than +2. A summary of the oxidation numbers of Ag, Fe and Ni, along with their respective energy edge position can be found in Table 4.7.

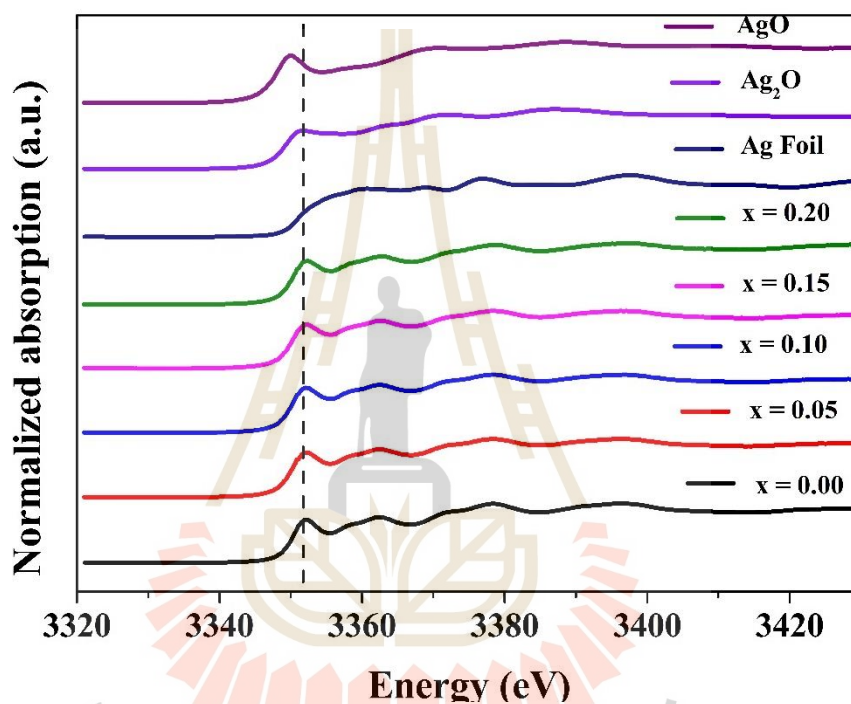


Figure 4.37 Normalized XANES spectra at Ag L3-edge of Ni-doped AgFeO_2 nanoparticles with different Ni concentrations.

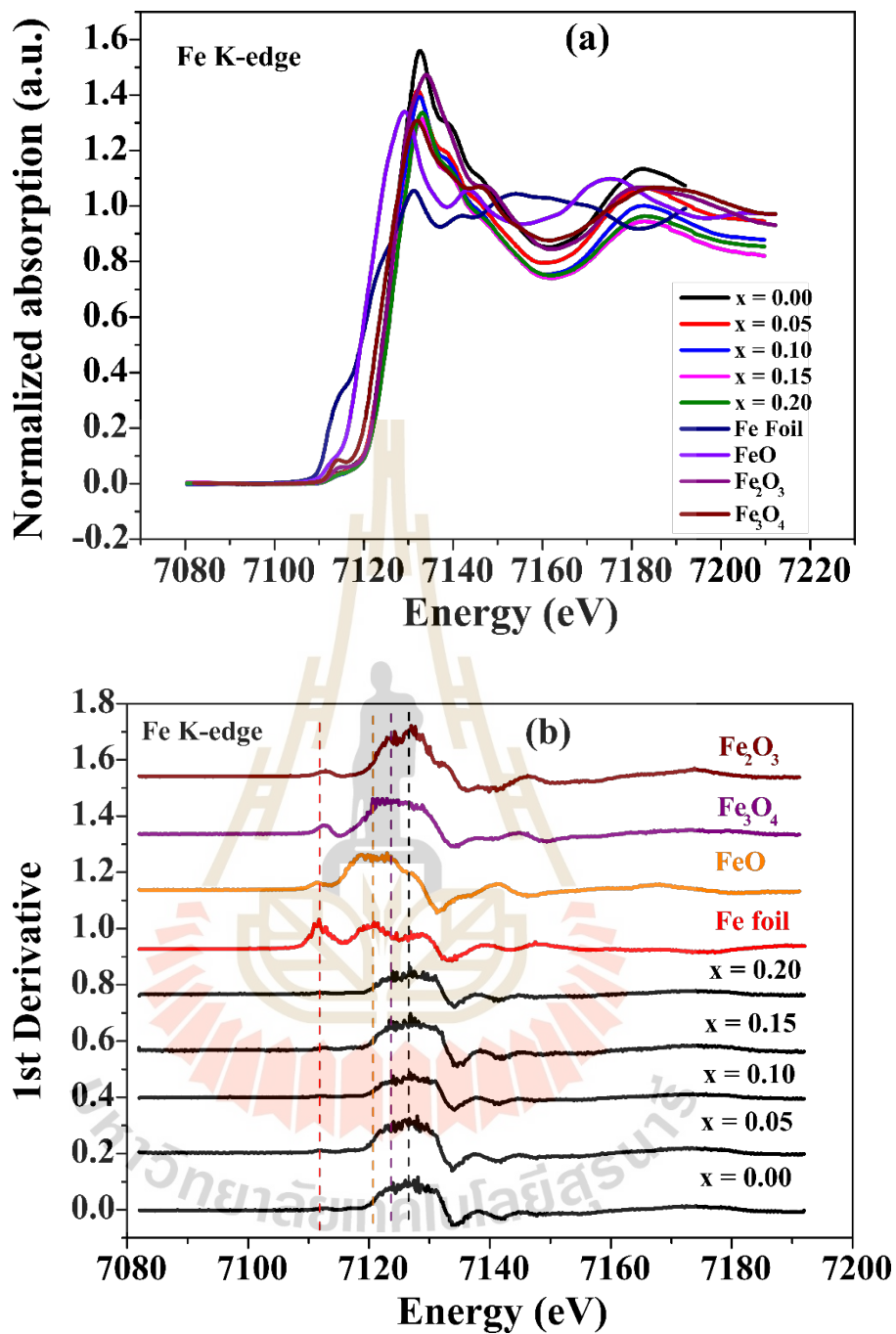


Figure 4.38 (a) Normalized XANES and (b) the associated first derivative plot at Fe K-edge of Ni-doped AgFeO₂ nanoparticles with different Ni concentrations.

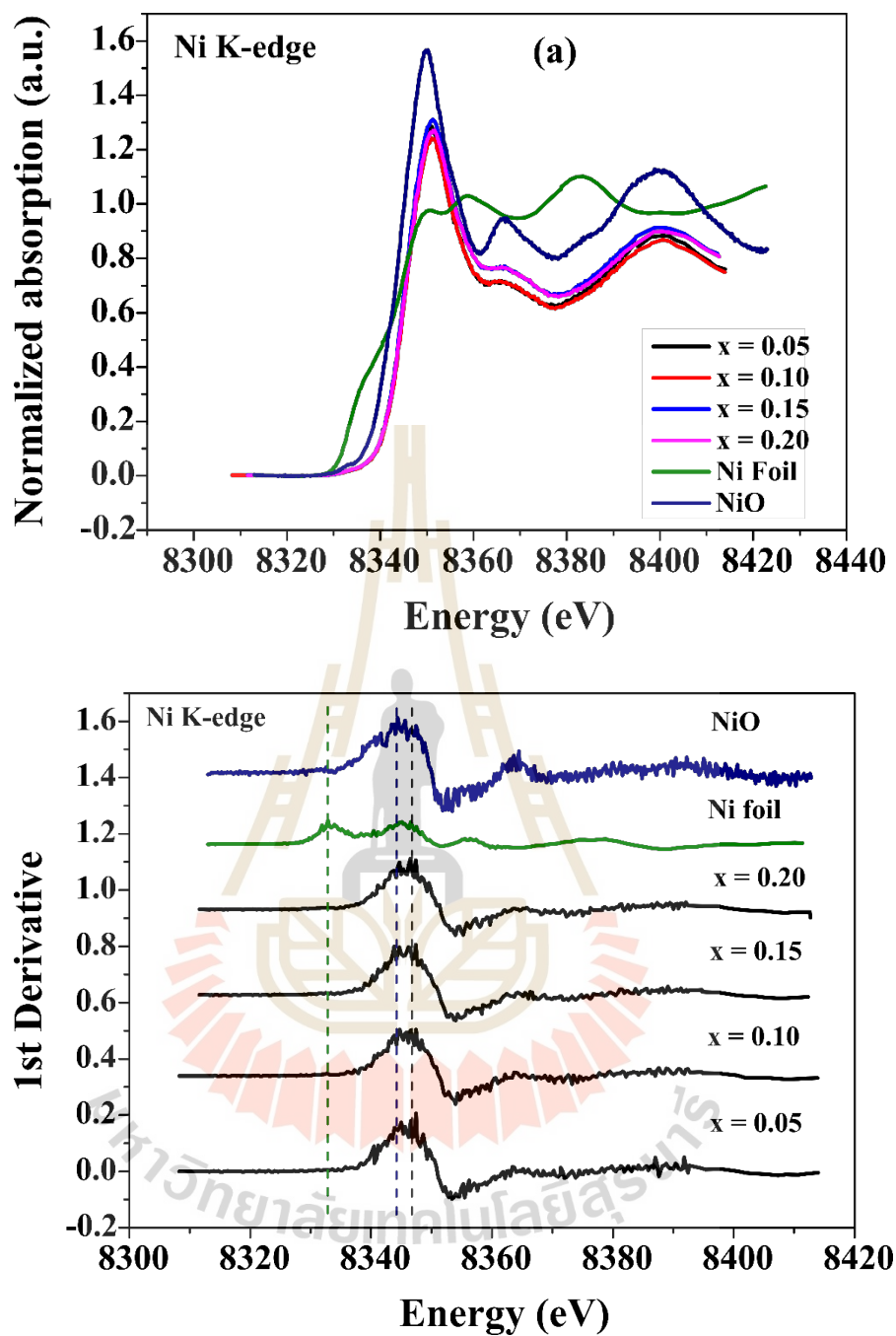


Figure 4.39 (a) Normalized XANES spectrum and (b) the first derivative plot at Ni K-edge of Ni-doped AgFeO_2 nanoparticles with different Ni concentrations.

Table 4.8 Energy edge position and corresponding valence states of the reference standard and Ni-doped AgFeO₂.

Samples	Edge elements	Edge energy (E) (eV)	Oxidation states
Ag foil	Ag	3351.30	+0
Ag ₂ O	Ag	3349.39	+1
AgO	Ag	3348.11	+2
Fe foil	Fe	7111.65	+0
FeO	Fe	7119.89	+2
Fe ₃ O ₄	Fe	7123.23	+2, +3
Fe ₂ O ₃	Fe	7126.76	+3
Ni foil	Ni	8332.64	+0
NiO	Ni	8344.42	+2
x = 0.00	Ag	3350.45	+1
	Fe	7126.57	+3
x = 0.05	Ag	3350.02	+1
	Fe	7126.60	+3
	Ni	8347.36	>+2
x = 0.10	Ag	3350.48	+1
	Fe	7127.18	+3
	Ni	8346.97	>+2
x = 0.15	Ag	3350.27	+1
	Fe	7126.40	+3
	Ni	8347.40	>+2
x = 0.20	Ag	3350.49	+1
	Fe	7126.50	+3
	Ni	8347.09	>+2

Furthermore, the chemical composition and the oxidation states of the AgFe_{1-x}Ni_xO₂ nanoparticles were conducted by the technique of XPS. To fit the Ag 3d, Fe 2p, Ni 2p and O 1s spectra of all the Ni-doped AgFeO₂ nanoparticles, we used

Gaussian fitting technique. For the Ag 3d core level for all Ni-doped AgFeO₂ samples, the binding energies were observed at ~ 367.45 eV and ~ 372.88 eV for Ag 3d_{5/2} and Ag 3d_{3/2}, respectively, indicating the presence of Ag⁺¹ (Mao et al., 2016; Zhou et al., 2011), as shown in Figure 4.40. These results reveal that Ag ion in the AgFe_{1-x}Ni_xO₂ nanoparticles with x = 0.00, 0.05, 0.10, 0.15 and 0.20 comprises the oxidation states of Ag⁺. Regarding the XPS spectrum of Fe 2p in all the Ni-doped AgFeO₂ samples, the binding energies of ~ 711.36 eV and ~ 724.74 eV were detected for the Fe 2p_{3/2} and Fe 2p_{1/2}, respectively, with two satellite peaks (Denoted as “Sat.”), as illustrated in Figure 4.41, which refer to the presence of Fe³⁺ (Ahmed et al., 2020; Yamashita and Hayes, 2008; Mills and Sullivan, 1983; Hawn and DeKoven, 1987; Muhler, Schlögl, and Ertl, 1992). Figure 4.42 presents the XPS spectra of Ni 2p. The two main peaks at ~ 857.15 eV and ~ 874.26 eV binding energies were found for the Ni 2p_{3/2} and Ni 2p_{1/2}, respectively, and two satellite peaks were identified. This exhibits the presence of Ni³⁺ (Cheng et al., 2017) ions in all the AgFe_{1-x}Ni_xO₂ nanoparticles. For the O 1s XPS spectra of the synthesize sample, the main peak was observed at ~ 530.77 eV binding energy and the shoulder was detected at ~ 533 eV, which correspond to the lattice oxygen within the AgFe_{1-x}Ni_xO₂ structure and OH⁻ group, respectively (Figure 4.43) (Ahmed et al., 2020; Che et al., 2016).

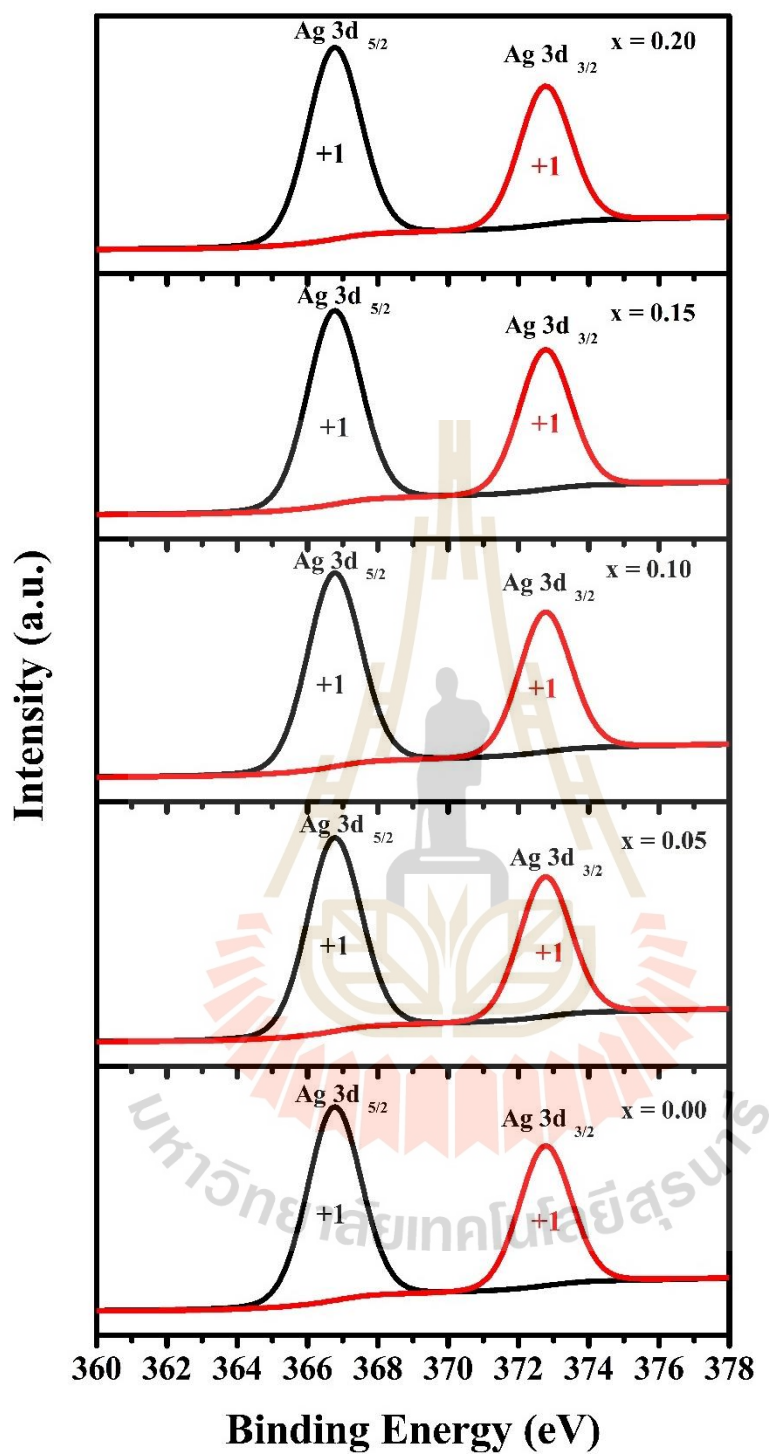


Figure 4.40 XPS spectra at Ag 3d of $\text{AgFe}_{1-x}\text{Ni}_x\text{O}_2$ nanoparticles.

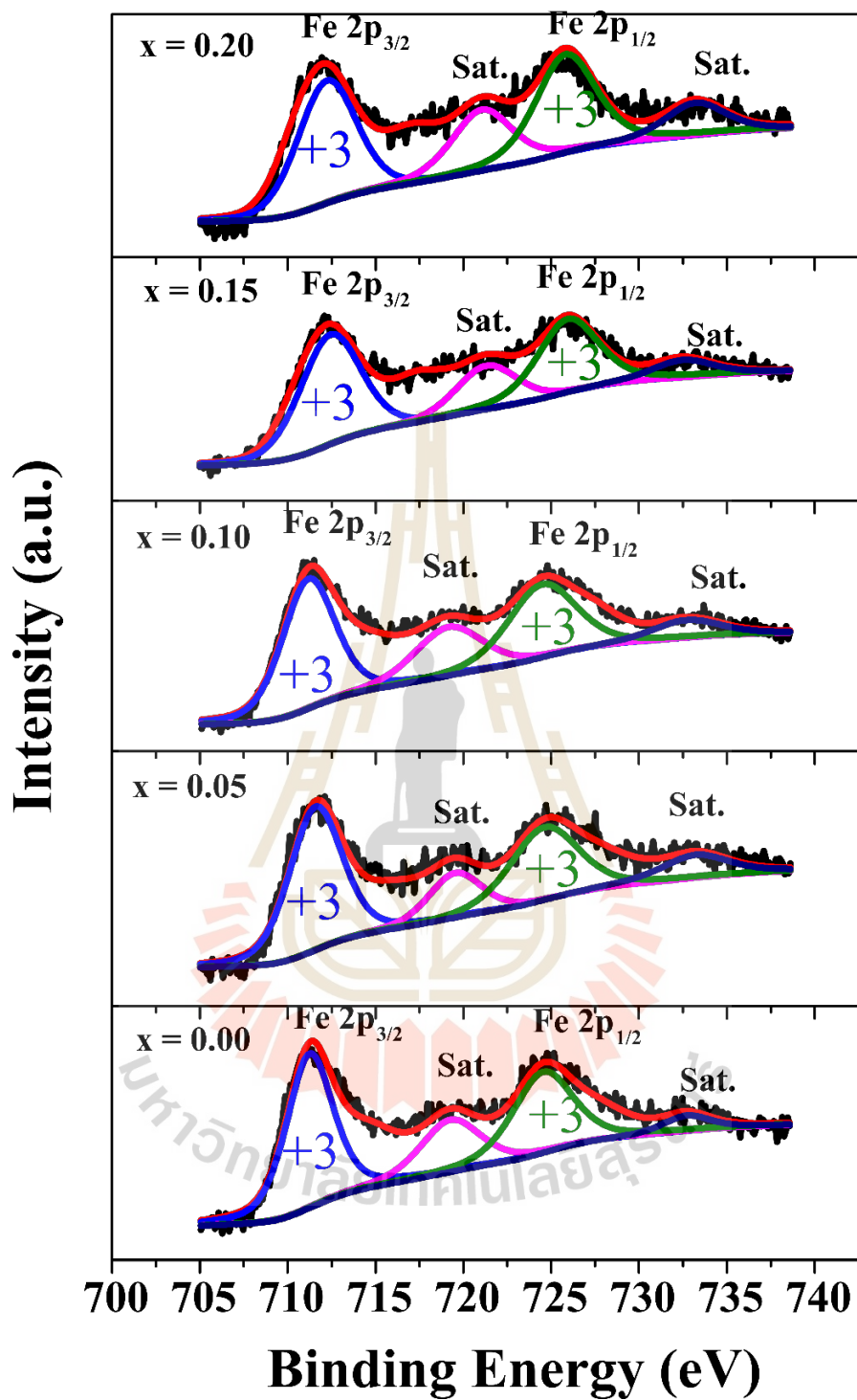


Figure 4.41 XPS spectrum at Fe 2p of $\text{AgFe}_{1-x}\text{Ni}_x\text{O}_2$ samples.

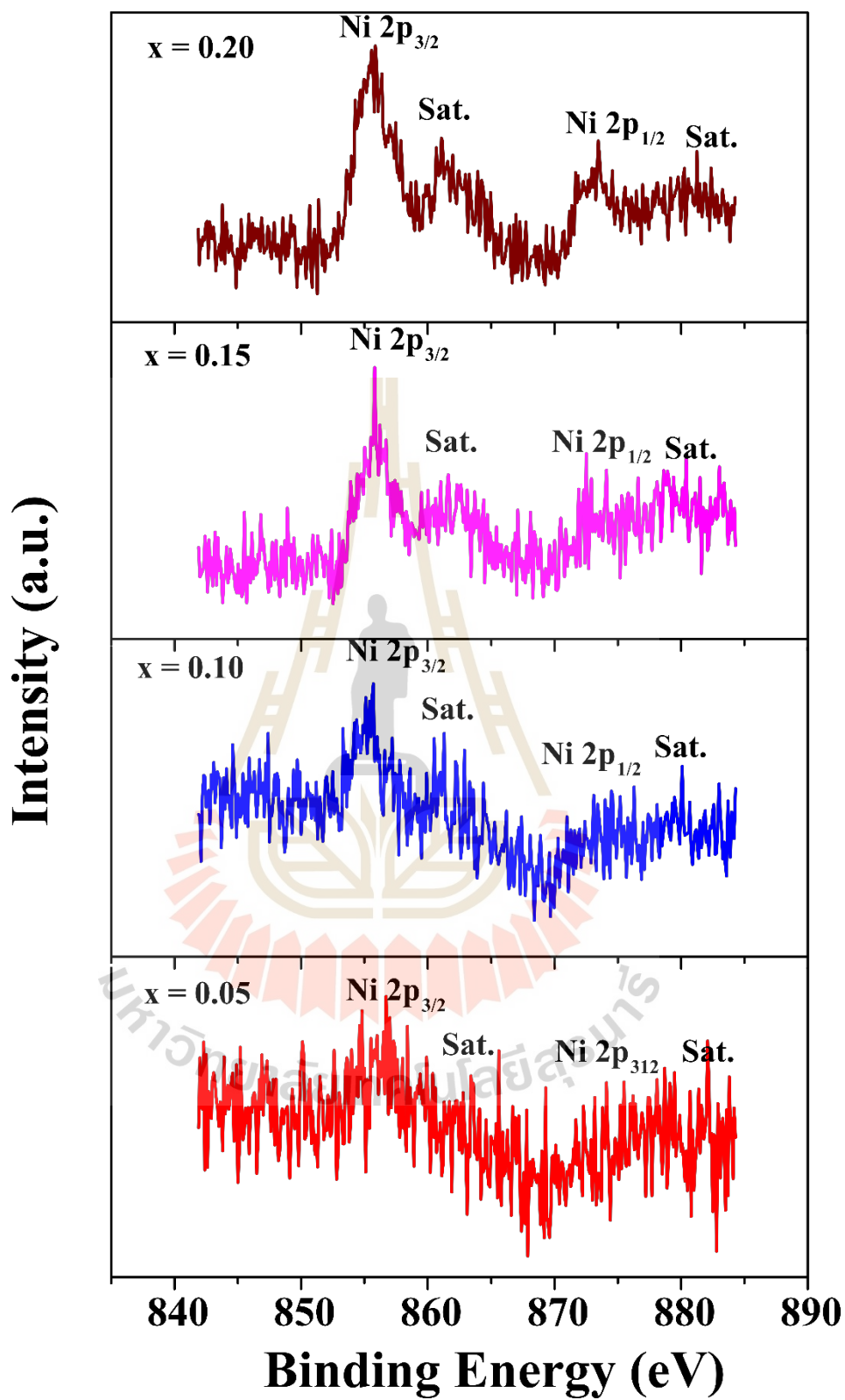


Figure 4.42 XPS spectrum at Ni 2p of $\text{AgFe}_{1-x}\text{Ni}_x\text{O}_2$ nanoparticles with x spanning from 0.00, to 0.20.

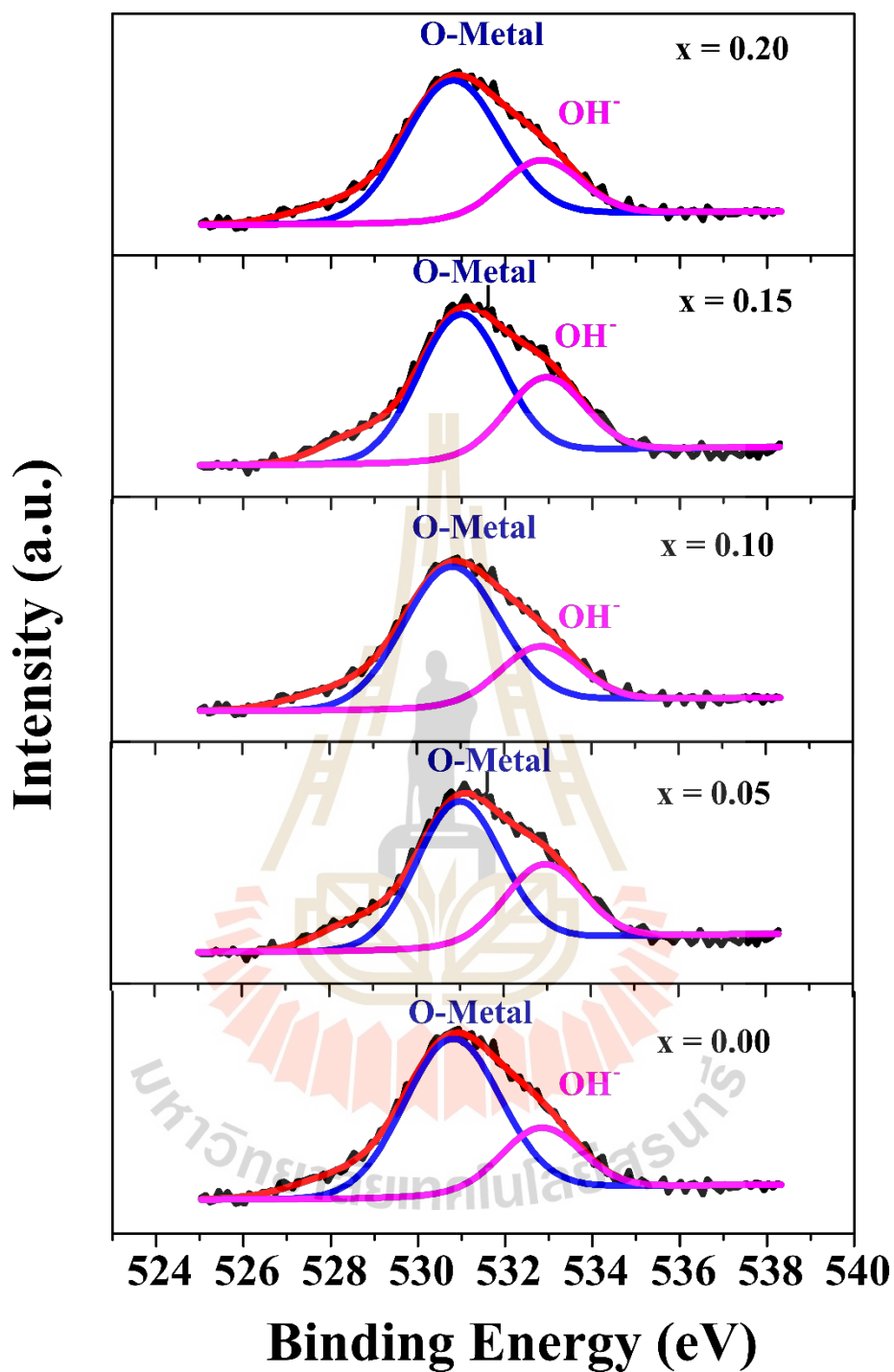


Figure 4.43 XPS spectrum at O 1s of $\text{AgFe}_{1-x}\text{Ni}_x\text{O}_2$ nanoparticles with different concentrations.

4.3.3 Surface area, pore volume and distribution of pore size study of Ni-doped AgFeO_2 nanoparticles by BJH and BET methods

In addition, Figure 4.44(a-e) displays the plot N_2 adsorption/desorption isotherm of $\text{AgFe}_{1-x}\text{Ni}_x\text{O}_2$ with a small hysteresis loop in the 0 to 1 range which suggests that all the samples are in the type of mesoporous structure. However, the pore size distribution of the $\text{AgFe}_{1-x}\text{Ni}_x\text{O}_2$ with $x = 0.00, 0.05, 0.10, 0.15$ and 0.20 are in the 2 to 50 nm range, as depicted in Figure 4.44(a-e) (inset), providing the mesoporous feature for all the samples. Based on the results obtained from the BET method, the BET specific surface area (S_{BET}) values of 28.22, 28.95, 30.99, 40.90 and 32.74 m^2/g were found for delafossite $\text{AgFe}_{1-x}\text{Ni}_x\text{O}_2$ nanoparticles with Ni concentrations of $x = 0.00, 0.05, 0.10, 0.15$ and 0.20 , respectively. It could be indicated that when increasing the Ni amount from $x = 0.00$ to $x = 0.15$, resulting in a noticeable increase in BET specific surface area values. This rise can be primarily attributed to the decrease in particle size. Conversely, when the Ni concentration reaches $x = 0.20$, there is a decrease in BET specific surface area. This decline is likely due to the significant aggregation of nanoparticles in the samples. Using the BJH method, the sample with different Ni amount of $x = 0.00, 0.05, 0.10, 0.15$ and 0.20 exhibit pore volume (V_{BJH}) values of 0.134, 0.141, 0.146, 0.177 and 0.148 cm^3/g , respectively. Table 4.6 provides a comprehensive overview of the BET specific surface area, pore volume and average pore size distribution (D_{avg}). These results highlight that variations in the concentration of Ni have a discernible impact on the value of BET specific surface area, pore size and pore volume distribution of the synthesized AgFeO_2 nanoparticles, which in turn could influence their electrochemical properties.

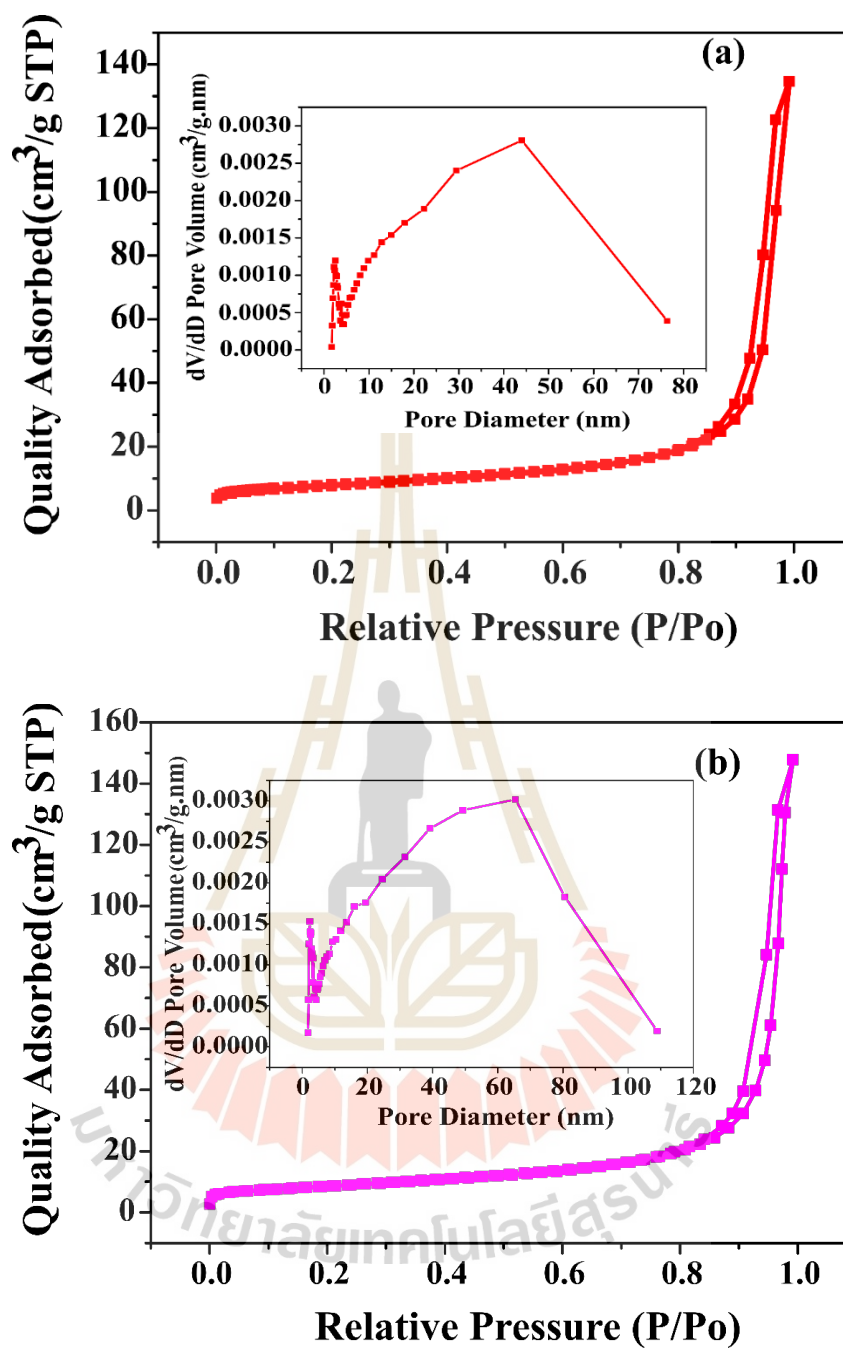


Figure 4.44 The pore size distribution (inset) and N₂ adsorption-desorption isotherms of AgFe_{1-x}Ni_xO₂ samples with (a) $x = 0.00$, (b) $x = 0.05$, (c) $x = 0.10$, (d) $x = 0.15$, and (e) $x = 0.20$.

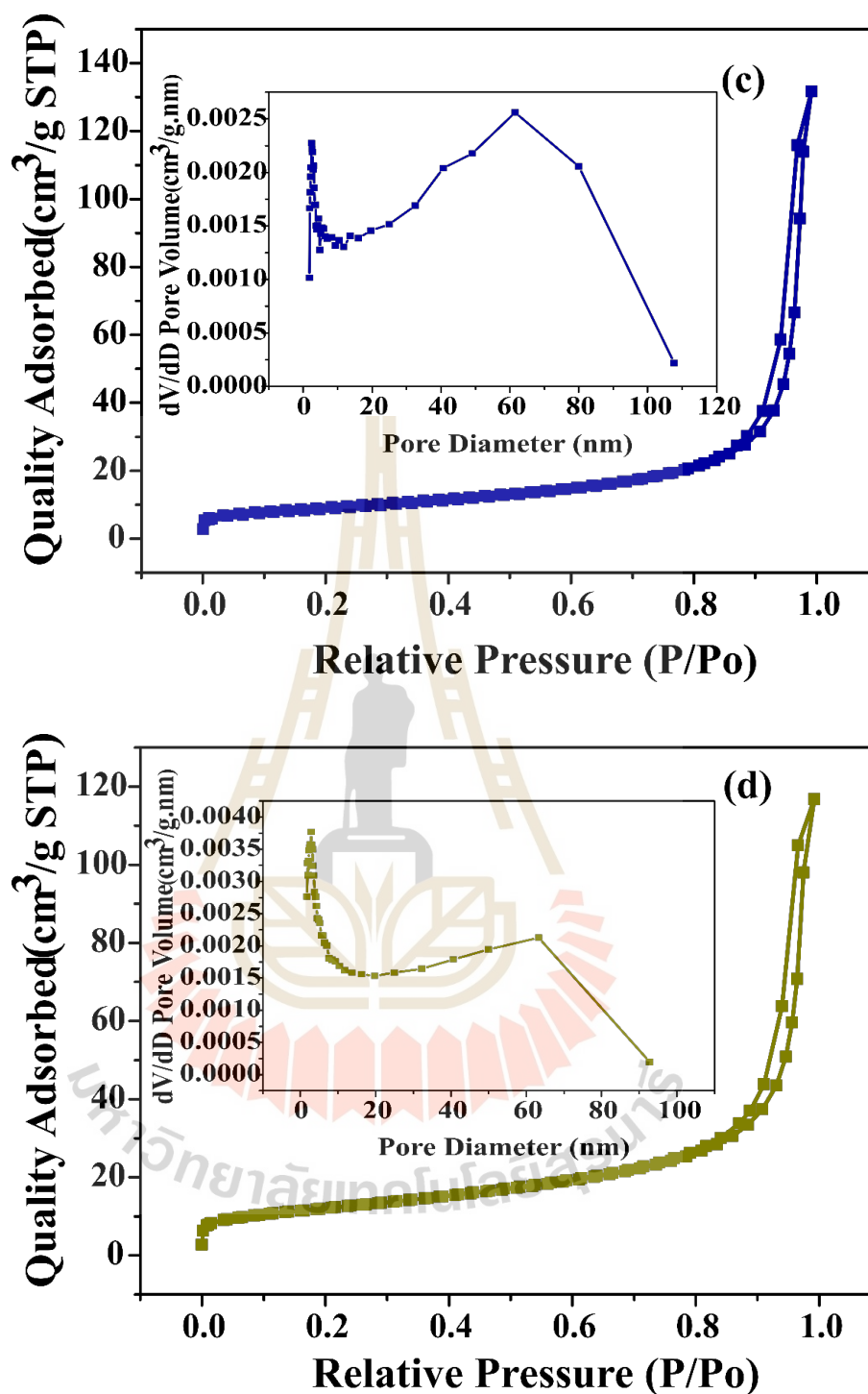


Figure 4.44 (Continued) The pore size distribution (inset) and N_2 adsorption-desorption isotherms of $AgFe_{1-x}Ni_xO_2$ samples with (a) $x = 0.00$, (b) $x = 0.05$, (c) $x = 0.10$, (d) $x = 0.15$, and (e) $x = 0.20$.

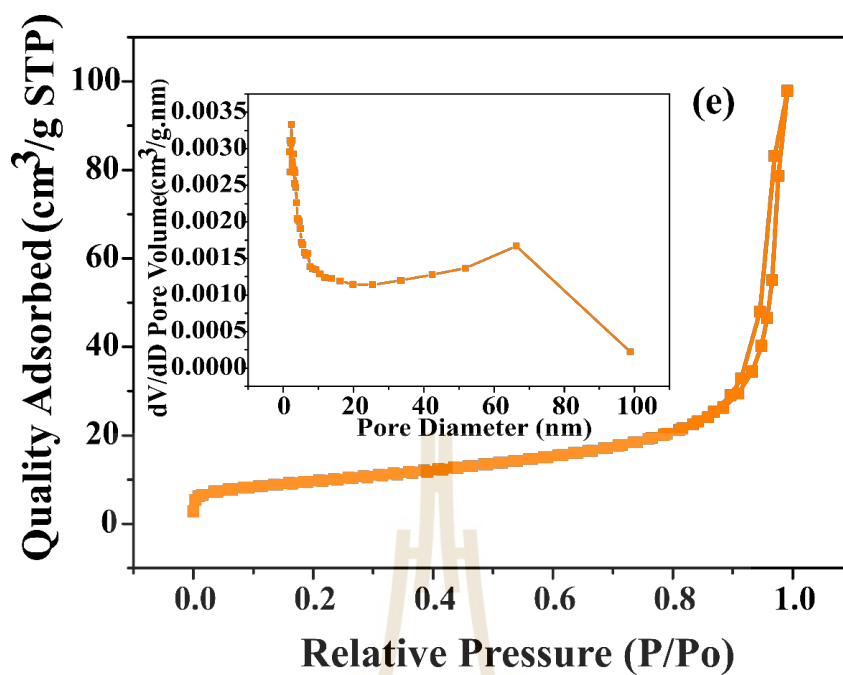


Figure 4.44 (Continued) The pore size distribution (inset) and N_2 adsorption-desorption isotherms of $AgFe_{1-x}Ni_xO_2$ samples with (a) $x = 0.00$, (b) $x = 0.05$, (c) $x = 0.10$, (d) $x = 0.15$, and (e) $x = 0.20$.

Table 4.9 The values of average pore size, BET specific surface area, and pore volume for the $AgFe_{1-x}Ni_xO_2$ nanoparticles.

Condition	S_{BET} (m^2/g)	V_{BJH} (cm^3/g)	D_{avg} (nm)
$X = 0.00$	28.22	0.134	18.95
$X = 0.05$	28.95	0.141	11.92
$X = 0.10$	30.99	0.146	9.71
$X = 0.15$	40.90	0.177	7.79
$X = 0.20$	32.74	0.148	8.16

4.3.4 Electrochemical performance of Ni-doped AgFeO₂ nanoparticles

4.3.4.1 Cyclic voltammetry performance

Electrochemical performance and specific capacitance of delafossite AgFe_{1-x}Ni_xO₂ with x = 0.00, 0.05, 0.10, 0.15 and 0.20 were investigated using cyclic voltammetry (CV) measurement, which carry on a three-electrode system. In the CV process, the AgFe_{1-x}Ni_xO₂ electrodes were conducted in 3M KOH electrolyte with different scan rates spanning from 2 to and 100 mV/s, utilizing a window of potential range between 1.16 V to 3.5 V, as depicted in Figure 4.45(a-e). The CV curves peaks reduction/oxidation for all the Ni-doped AgFeO₂ samples indicate that the observed pseudocapacitor feature arises from the faradaic redox reactions involving Ag/Ag⁺, Fe²⁺/Fe³⁺ and Ni²⁺/Ni³⁺ (Wongpratad et al., 2020; Pai et al., 2018; Stern and Hu, 2014). The reversible redox process involves the conversion between Ag and Ag⁺, Fe²⁺ and Fe³⁺ and Ni²⁺ and Ni³⁺ during reduction-oxidation reactions can be clarified as follow:



or



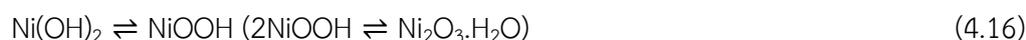
or



And



or



Based on the CV curves at the different scan rates spanning from 2 to 100 mV/s, the values of specific capacitance of the Ni-doped AgFeO₂ electrodes could be estimated by equation 3.17. At a low scan rate of 2 mV/s, the highest specific

capacitance values of 358.32, 372.64, 386.80, 396.66 and 388.89 F/g were evaluated for Ni-doped AgFeO_2 samples where Ni amount of $x = 0.00, 0.05, 0.10, 0.15$ and 0.20 , respectively, as shown in Figure 4.45f. The results show that the sample with $x = 0.15$ displays the highest specific capacitance value. This may owing to its highest BET specific surface area and pore volume distribution.

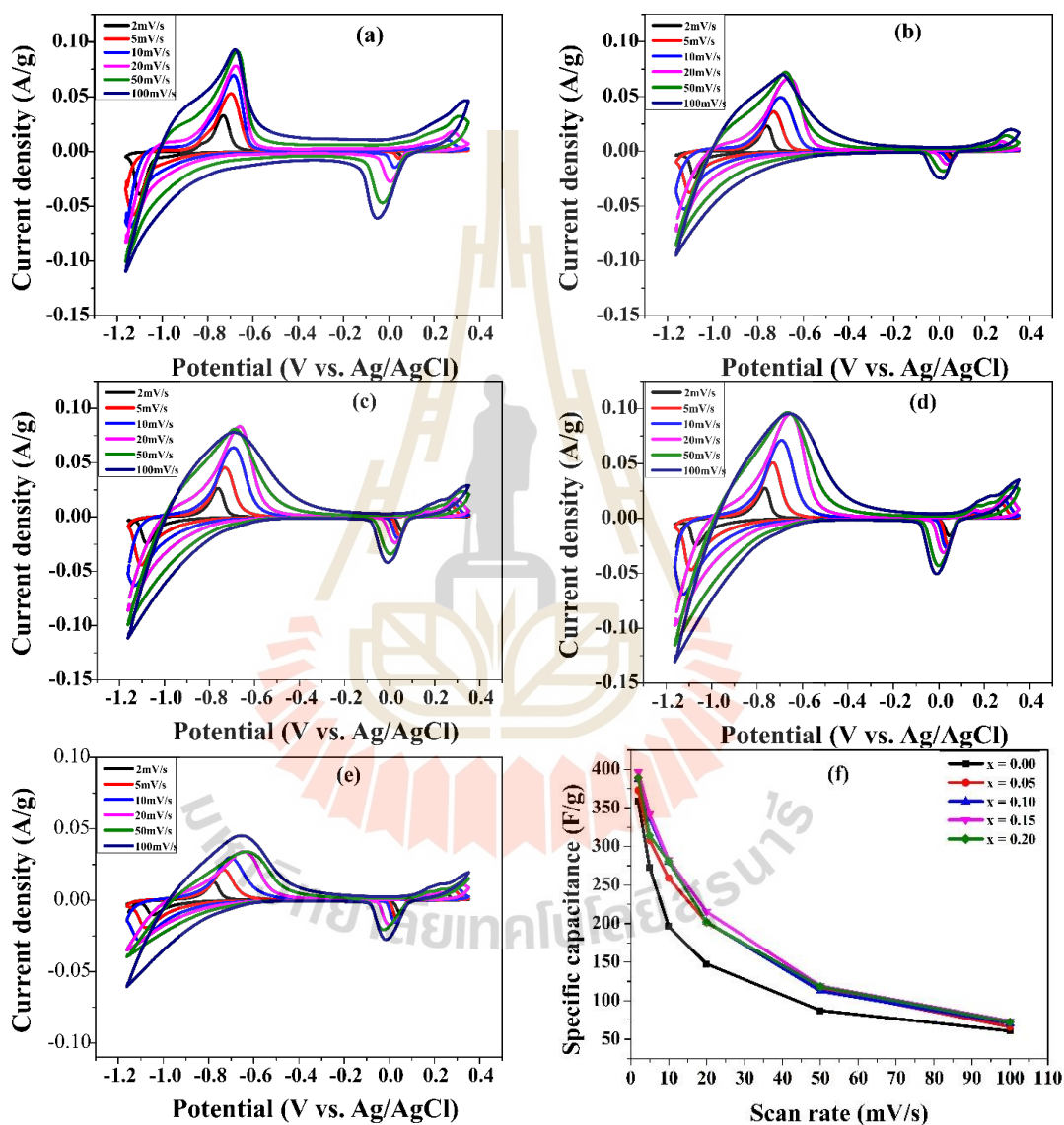


Figure 4.45 CV curves of $\text{AgFe}_{1-x}\text{Ni}_x\text{O}_2$ nanoparticles at different scan rates with (a) $x = 0.00$, (b) $x = 0.05$, (c) $x = 0.10$, (d) $x = 0.15$, (e) $x = 0.20$, and (f) the values of calculated specific capacitance.

4.3.4.2 Galvanostatic charge discharge measurement

Additionally, GCD measurement was applied to examine the electrochemical performance of all the Ni-doped AgFeO_2 electrodes which performs in 3M KOH solution with the spanning from 1 to 20 A/g current densities. The results of GCD testing of $\text{AgFe}_{1-x}\text{Ni}_x\text{O}_2$ where $x = 0.00, 0.05, 0.10, 0.15$ and 0.20 are illustrated in Figure 4.46(a-e), which implies that all the doping conditions were in the typical characteristic of pseudocapacitive. The specific capacitance values of all Ni-doped AgFeO_2 samples were computed using the discharge curves of GCD testing. The obtained specific capacitance values at various current densities of the electrode are shown in Figure 4.46(f). The figure makes it clear that when the current density increases, there is concurrent reduction in the specific capacitance value. This can be attributed to the rising internal polarization and resistance of the electrodes. At the low current density of 1 A/g, the specific capacitance values for $\text{AgFe}_{1-x}\text{Ni}_x\text{O}_2$ were determined as follows: 229.71 F/g for $x = 0.00$, 251.10 F/g for $x = 0.05$, 310.59 F/g for $x = 0.10$, 339.08 F/g for $x = 0.15$ and 324.07 F/g for $x = 0.20$. Remarkably, the $\text{AgFe}_{1-x}\text{Ni}_x\text{O}_2$ with doping condition of 0.15 exhibited the highest value of specific capacitance reaching 339.08 F/g. This result can be attributed to its superior value of BET specific surface area, which provides greater sites of active for faradaic reversible reduction/oxidation reactions. Moreover, the stability of cycling of the $\text{AgFe}_{1-x}\text{Ni}_x\text{O}_2$ was carried out by a continuous charging-discharging experiment comprising 1000 cycles, conducted at a 5 A/g current density. After 1000 charge/discharge cycles, the capacitance retention values of 82.99, 82.15, 85.54, 87.04, and 83.15% were obtained from $\text{AgFe}_{1-x}\text{Ni}_x\text{O}_2$ where $x = 0.00, 0.05, 0.10, 0.15$ and 0.20 respectively, as seen in Figure 4.47. It could reveal that the Ni concentration of $x = 0.15$ displays superior capacitance and long-life cycling stability. Table 4.9 represents the specific capacitance values of the Ni-doped AgFeO_2 electrodes.

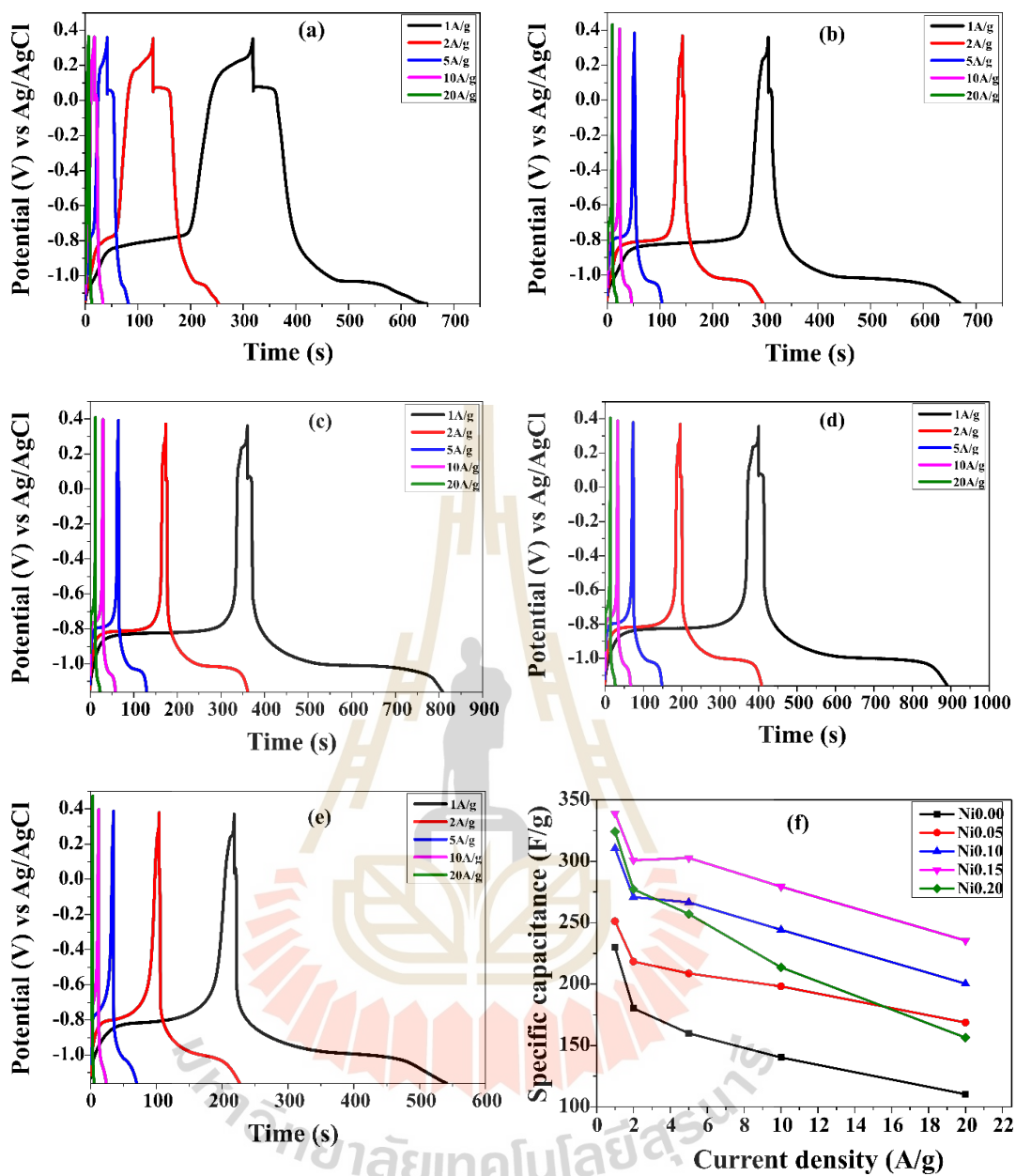


Figure 4.46 GCD plot of $\text{AgFe}_{1-x}\text{Ni}_x\text{O}_2$ nanoparticles with (a) $x = 0.00$, (b) $x = 0.05$, (c) $x = 0.10$, (d) $x = 0.15$, (e) $x = 0.20$, and (f) the values of specific capacitance at various current densities.

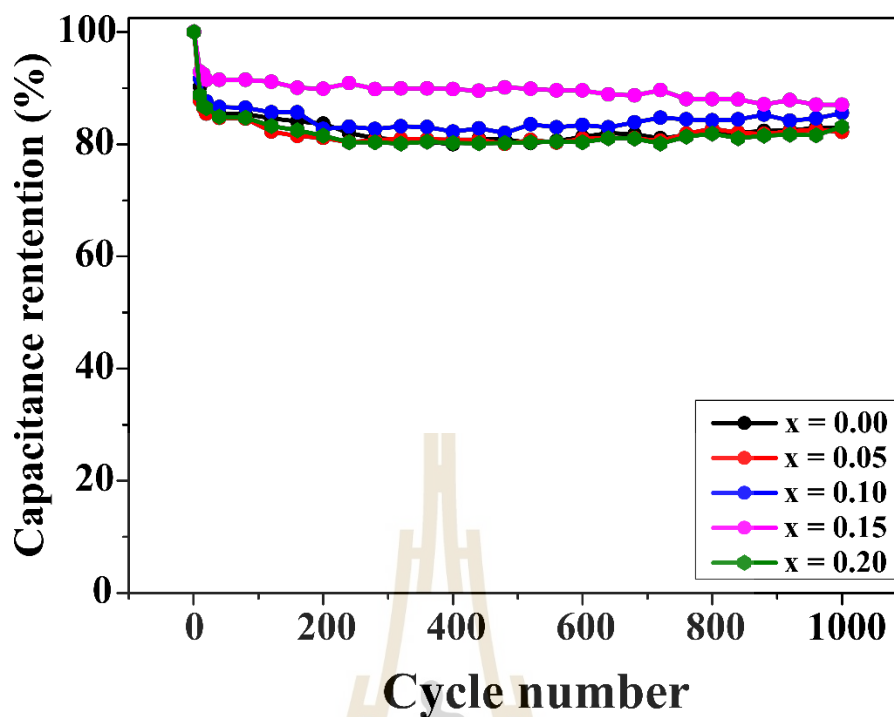


Figure 4.47 Capacitance retention (%) of $\text{AgFe}_{1-x}\text{Ni}_x\text{O}_2$.

Table 4.10 List of the specific capacitance values of $\text{AgFe}_{1-x}\text{Ni}_x\text{O}_2$ calculated employing GCD technique.

Current density (A/g)	Specific capacitance at various Ni concentrations (F/g)				
	x = 0.00	x = 0.05	x = 0.10	x = 0.15	x = 0.20
1	229.71	251.10	310.59	339.08	324.07
2	180.17	218.28	270.77	302.80	277.20
5	159.87	208.62	266.64	300.80	257.01
10	140.20	198.08	244.15	279.27	213.54
20	110.28	168.62	200.26	235.40	156.29

4.3.4.3 Electrochemical impedance spectroscopy analysis

EIS study was presented by Nyquist plots, as shown in Figure 4.48. The EIS curves for all the $\text{AgFe}_{1-x}\text{Ni}_x\text{O}_2$ electrodes where $x = 0.00, 0.05, 0.10, 0.15$ and 0.20 exhibit the incomplete semicircle pattern in the high-frequency region. The point where the curve intersects the real axis (Z') presents the equivalent series resistance (R_{esr}) or the solution resistance (R_s). The solution resistance (R_s) yielded values of 1.24, 1.17, 1.15, 1.07, and 1.16 Ω were observed for with $\text{AgFe}_{1-x}\text{Ni}_x\text{O}_2$ different Ni doping of $x = 0.00, 0.05, 0.10, 0.15$ and 0.20 , respectively. The diameter of the circle was used to determine the charge transfer resistance (R_{ct}). Furthermore, the presence of Warburg impedance (W) was illustrated by the descending line observed in the region of low-frequency, which signifies the ions diffusion between electrode material and electrolyte. According to the small semicircle in the middle-frequency region, It was found that all the electrodes exhibit low charge transfer resistance (R_{ct}). Interesting, $\text{AgFe}_{1-x}\text{Ni}_x\text{O}_2$ with Ni concentration of 0.15 displays the lowest solution resistance (R_s) value. This reveals that $\text{AgFe}_{0.85}\text{Ni}_{0.15}\text{O}_2$ samples could be considered as electrode material for energy storage technology.

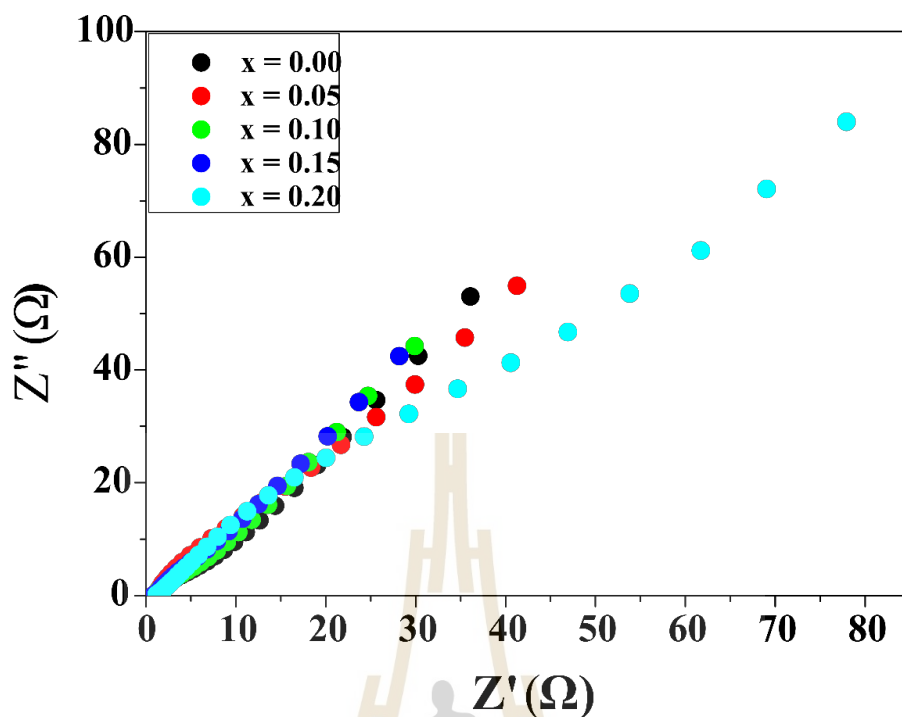


Figure 4.48 Nyquist plot of $\text{AgFe}_{1-x}\text{Ni}_x\text{O}_2$ electrodes.

4.3.4.4 Specific energy and specific power study

To evaluate the energy storage performance, the Ragone plot was used, which represents between specific energy and specific power relationship. Figure 4.49 displays the Ragone plots of all the Ni-doped AgFeO_2 samples at different current densities of 1, 2, 5, 10 and 20 A/g. At a 1 A/g current density, It was found that $\text{AgFe}_{1-x}\text{Ni}_x\text{O}_2$ nanoparticles where $x = 0.00, 0.05, 0.10, 0.15$ and 0.20 exhibit the specific energies and specific power values of 72.74 Wh/Kg and 797.46 W/Kg, 79.52 Wh/Kg and 786.79 W/Kg, 98.35 Wh/Kg and 789.59 W/Kg, 109.28 Wh/Kg and 800.51 W/Kg and 102.62 Wh/Kg and 783.18 W/Kg, respectively, which reveal that $\text{AgFe}_{1-x}\text{Ni}_x\text{O}_2$ with Ni amount of 0.15 shows the superior values of specific energy and specific power.

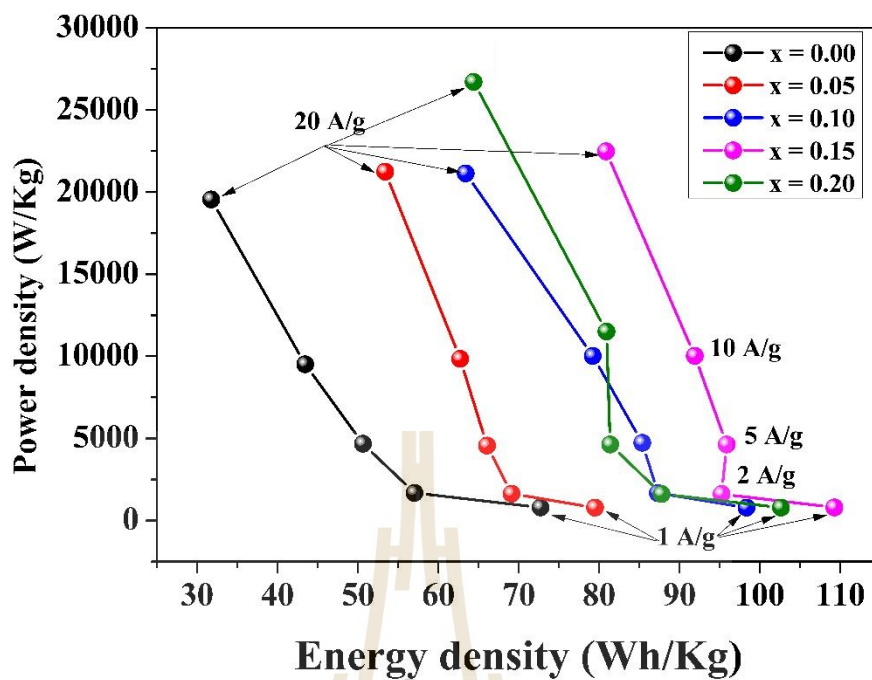


Figure 4.49 Specific energies and corresponding specific power of Ni-doped AgFeO₂ electrodes at current densities of 1, 2, 5, 10 and 20 A/g.

CHAPTER V

CONCLUSIONS AND SUGGESTIONS

In this research, pure AgFeO_2 and $\text{AgFe}_{1-x}\text{M}_x\text{O}_2$ ($\text{M} = \text{Co}$ and Ni) nanostructures where $x = 0.00, 0.05, 0.10, 0.15$ and 0.20 were successfully synthesized by a simple co-precipitation method. The structure and morphology of the prepared samples were determined by XRD, TEM and SEM. The elemental composition and oxidation state were studied by XAS and XPS. The porosity properties were calculated by BET and BJH methods, utilizing gas absorption technique. The electrochemical performance was examined using techniques of CV, GCD and EIS. All the experimental results can be concluded as follow:

5.1 Effect of different calcination temperatures on structure and electrochemical performance of AgFeO_2 nanoparticles

Delafossite AgFeO_2 nanostructures with mixing phases of the rhombohedral 3R- AgFeO_2 (JCPDS No: 00-029-1141) and hexagonal polytype 2H- AgFeO_2 (JCPDS No: 00-018-1175) was successfully prepared using a simple co-precipitation route. It was evident that the particle size of AgFeO_2 nanoparticles increased with increasing the calcination temperature. However, the sample calcined at 100°C showed the highest percentage of 2H phase of 70.06% and smallest particles size of 45 nm, resulting in the largest specific surface area of $28.22 \text{ m}^2/\text{g}$. For electrochemical performance, it was found that all the AgFeO_2 electrodes exhibited the characteristic feature of pseudocapacitive behavior with clarification redox peaks at the low current density of 1 A/g , AgFeO_2 nanoparticles calcined at 100°C provided good electrochemical properties, suggesting a high specific capacitance of 229.71 F/g with associating specific energy of 72.74 Wh/Kg and specific power of 797.46 W/Kg and superior cyclic stability of 82.99% after 1000 charge/discharge cycles. These are due to its highest 2H

phase amount and specific surface area. The high amount of 2H phase provides greater inter layer gap, which improved K^+ ion accessibility into the electrodes' internal structure. Moreover, the large specific surface area can make the high active site, which results in excellent ion diffusion between the electrolyte and electrode material and multiple reduction/oxidation reaction, providing high specific capacitance. This was evident that the various calcination temperatures affected on the structures (particle size, specific surface area, pore volume and pore size distributions), phase transformation between 2H and 3R and electrochemical performance of delafossite $AgFeO_2$ nanostructures.

5.2 effect of Co and Ni-doped $AgFeO_2$ on structure and electrochemical performance

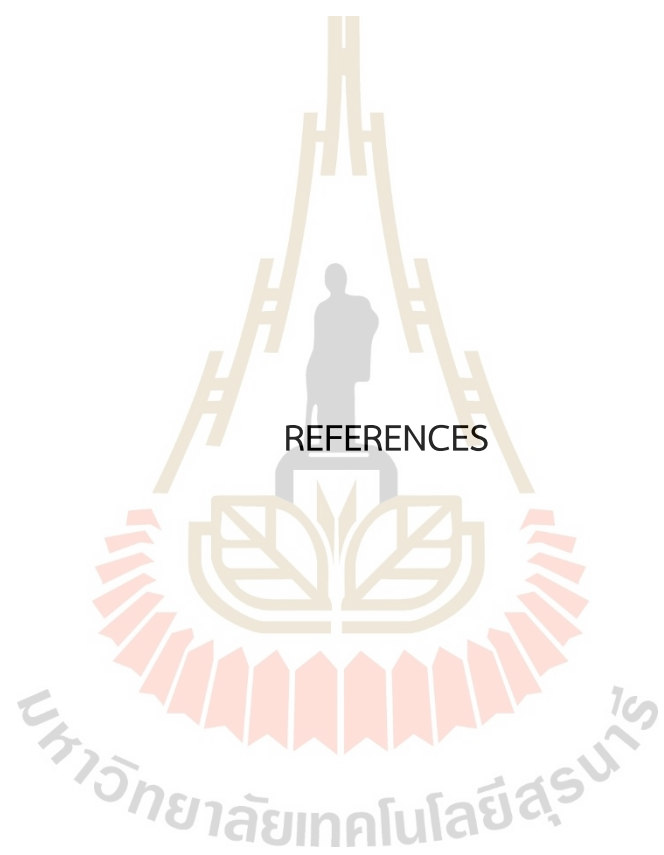
A simple co-precipitation method was successfully employed to synthesize Co and Ni-doped $AgFeO_2$ nanostructures with 3R and 2H phases. In case of Co-doped $AgFeO_2$ nanoparticles, even though there are additional peaks illustrated in the XRD spectra of the doped samples, which could be referred to metallic silver there are no indications of impurity phases like metallic cobalt, CoO , Fe_2O_3 , or $CoFe_2O_4$ spinel. These impurity phases typically form under condition similar to the synthesis of $AgFeO_2$. The absence of cobalt-related phases suggests that cobalt ions might substitute iron ions within the delafossite crystal structure. Nonetheless, the presence of metallic silver comes as a surprising observation when considering the assumption that Co^{3+} would replace Fe^{3+} ions during substitution. For Ni-doped $AgFeO_2$ nanoparticles, the successful replacement of Fe ions with Ni ions in the delafossite structure is affirmed by the absence of NiO . However, since cobalt (II) nitrate and nickel (II) nitrate were utilized as the starting material in the synthesis process, proposes that in this specific case, divalent cobalt and nickel ions could substitute trivalent iron ions. According to the findings from experiments, the doping of Co and Ni significantly influence both the structure and particle size. The observed trend is that as the Co and Ni contents in the $AgFeO_2$ nanoparticles increases from 0.00 to 0.15, there is a noticeable increase in the specific surface area. This can be attributed to the reduction in the size of particles. In contrast, the samples with Co

and Ni concentrations of 0.20 exhibit a reduction of specific surface area. This decrease might be attributed to the substantial nanoparticles accumulation in this particular sample. Generally, the BET specific surface area has an important impact on the electrochemical behavior of the materials. Based on the electrochemical properties study, it was revealed that the Co and Ni doping can improve electrochemical performance of AgFeO_2 nanostructures with increasing the specific capacitance, specific energy and cycling stability, which could bring to use as electrode material for supercapacitor and battery.

5.3 Suggestions

Based on our investigation into electrochemical properties of pure AgFeO_2 and $\text{AgFe}_{1-x}\text{M}_x\text{O}_2$ nanostructures, where M represents Co and Ni (with values of x ranging from 0.00 to 0.20), we propose the following avenues for future research to provide a more comprehensive elucidation of the finding:

- (i) Investigation of electrochemical properties in pure AgFeO_2 and $\text{AgFe}_{1-x}\text{M}_x\text{O}_2$ where M = Co and Ni (x = 0.00, 0.05, 0.10, 0.15 and 0.20) nanoparticles employing different substrate materials and different electrolytes with various concentrations to determine the optimal condition for creating supercapacitor electrode.
- (ii) Examining the local interatom distance through EXAFS is essential for gaining a more comprehensive understanding of structure change impacted on electrochemical properties of AgFeO_2 -based nanoparticles after the substitution of Co and Ni ions.
- (iii) The understanding of the mechanism of charge storage of these materials are currently lacking and not fully comprehensive. Thus, it is crucial to employ in-situ XAS to confirm alterations in valence state during the process of charging-discharging.



REFERENCES

REFERENCES

- Adongo, J. (2019). Modification of Surfaces with Carboxymethylthio and Piperazinyl Chelating Ligands for Heavy Metal Trapping Applications.
- ALothman, Zeid A. (2012). A review: fundamental aspects of silicate mesoporous materials, *Materials*, 5, 2874-902.
- Anderson, K., Benjamin, P., John, D., Shu-En, L., and Xiang, M. (2017). A highly sensitive nonenzymatic glucose biosensor based on the regulatory effect of glucose on electrochemical behaviors of colloidal silver nanoparticles on MoS₂, *Sensors*, 17, 1807.
- Abdah, M. A. A. M., Azman, N. H. N., Kulandaivalu, S., and Sulaiman, Y. (2020). Review of the use of transition-metal-oxide and conducting polymer-based fibres for high-performance supercapacitors. *Materials & Design*, 186, 108199.
- Abdelhamid, H. N., Talib, A., and Wu, H.-F. (2015). Correction: Facile synthesis of water soluble silver ferrite (AgFeO₂) nanoparticles and their biological application as antibacterial agents. *RSC Advances*, 5(50), 39952-39953.
- Ahmed, J., Alhokbany, N., Husain, A., Ahmad, T., Khan, M. A. M., and Alshehri, S. M. (2020). Synthesis, characterization, and significant photochemical performances of delafossite AgFeO₂ nanoparticles. *Journal of Sol-Gel Science and Technology*, 94(2), 493-503.
- An, K. H., Kim, W. S., Park, Y. S., Choi, Y. C., Lee, S. M., Chung, D. C., and Lee, Y. H. (2001). Supercapacitors using single-walled carbon nanotube electrodes. *Advanced materials*, 13(7), 497-500.
- Baskaran, S. (2010). Structure and regulation of yeast glycogen synthase.

- Béguin, F., Presser, V., Balducci, A., and Frackowiak, E. (2014). Carbons and electrolytes for advanced supercapacitors. *Advanced materials*, 26(14), 2219-2251.
- Berastegui, P., Tai, C.-W., and Valvo, M. (2018). Electrochemical reactions of AgFeO₂ as negative electrode in Li- and Na-ion batteries. *Journal of Power Sources*, 401, 386-396.
- Britannica, E. (2008). Britannica concise encyclopedia (Encyclopaedia Britannica, Inc.).
- Brousse, T., Toupin, M., and Belanger, D. (2004). A hybrid activated carbon-manganese dioxide capacitor using a mild aqueous electrolyte. *Journal of The Electrochemical Society*, 151(4), A614.
- Che, H., Aifeng Liu, J. M., Chunxia, W., and Xiaoliang, Z. (2016). Template-free synthesis of novel flower-like MnCo₂O₄ hollow microspheres for application in supercapacitors, *Ceramics International*, 42, 2416-24.
- Chmiola, J., Yushin, G., Gogotsi, Y., Portet, C., Simon, P., and Taberna, P.-L. (2006). Anomalous increase in carbon capacitance at pore sizes less than 1 nanometer. *science*, 313(5794), 1760-1763.
- Conway, B. E. (2013). Electrochemical supercapacitors: scientific fundamentals and technological applications: *Springer Science & Business Media*.
- Farley, K. E., Marschilok, A. C., Takeuchi, E. S., and Takeuchi, K. J. (2011). Synthesis and Electrochemistry of Silver Ferrite. *Electrochemical and Solid-State Letters*, 15(2), A23-A27.
- Gao, Y., Chen, S., Cao, D., Wang, G., and Yin, J. (2010). Electrochemical capacitance of Co₃O₄ nanowire arrays supported on nickel foam. *Journal of Power Sources*, 195(6), 1757-1760.
- Gujar, T., Shinde, V., Lokhande, C., and Han, S.-H. (2006). Electrosynthesis of Bi₂O₃ thin films and their use in electrochemical supercapacitors. *Journal of Power Sources*, 161(2), 1479-1485.

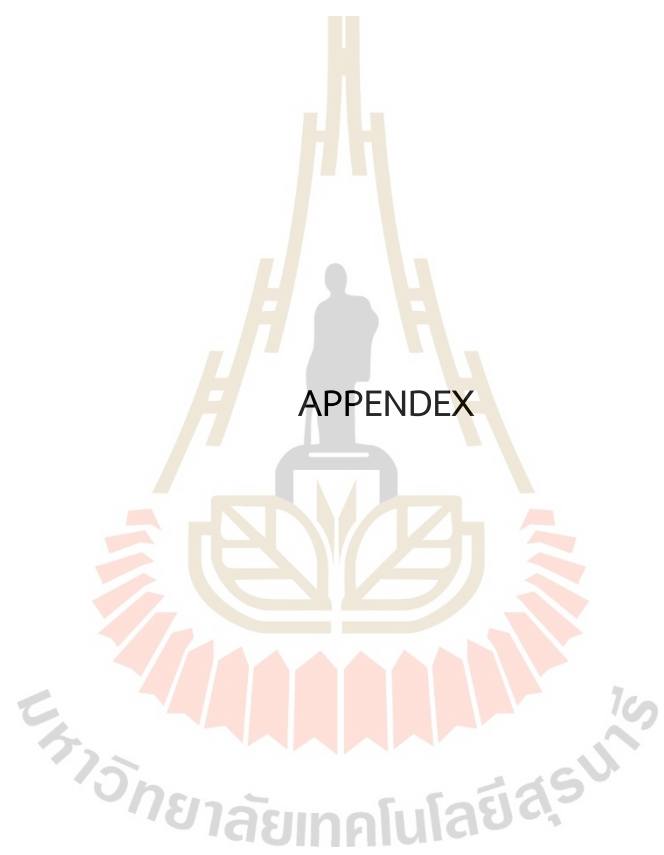
- Guo, F., Gupta, N., and Teng, X. (2018). Enhancing pseudocapacitive process for energy storage devices: analyzing the charge transport using electro-kinetic study and numerical modeling. *Supercapacitors: Theoretical and Practical Solutions*, 87.
- Hawn, D. D., and Benjamin M D. (1987). Deconvolution as a correction for photoelectron inelastic energy losses in the core level XPS spectra of iron oxides, *Surface and interface analysis*, 10, 63-74.
- Huang, J., Weixin, Q., Hongfang, M., Haitao, Z., and Weiyong, Y. (2017). Highly selective production of heavy hydrocarbons over cobalt-graphene-silica nanocomposite catalysts, *RSC advances*, 7, 33441-49.
- Hu, C.-C., and Chen, W.-C. (2004). Effects of substrates on the capacitive performance of $\text{RuO}_x \cdot n\text{H}_2\text{O}$ and activated carbon- RuO_x electrodes for supercapacitors. *Electrochimica Acta*, 49(21), 3469-3477.
- Jiang, Q. (2019). Engineering of pseudocapacitive materials and device architecture for on-chip energy storage.
- Kalawa, O., Kidkhunthod, P., Chanlek, N., Khajonrit, J., and Maensiri, S. (2019). Synthesis and electrochemical properties of polymer solution prepared MnCo_2O_4 nanoparticles. *Ionics*, 26(1), 457-469.
- Kalawa, O., Sichumsaeng, T., Kidkhunthod, P., Chanlek, N., and Maensiri, S. (2022). Ni-doped MnCo_2O_4 nanoparticles as electrode material for supercapacitors. *Journal of Materials Science: Materials in Electronics*, 33(8), 4869-4886.
- Kim, I.-H., and Kim, K.-B. (2006). Electrochemical characterization of hydrous ruthenium oxide thin-film electrodes for electrochemical capacitor applications. *Journal of The Electrochemical Society*, 153(2), A383.
- Lee, H. Y., and Goodenough, J. (1999). Ideal supercapacitor behavior of amorphous $\text{V}_2\text{O}_5 \cdot n\text{H}_2\text{O}$ in potassium chloride (KCl) aqueous solution. *Journal of Solid State Chemistry*, 148(1), 81-84.

- Mao, Y., Yuwen Y., Xianwei M., Changyi H., Chuan W., Jianwei W., and Hongwei Y. (2016). A Facile Approach to Prepare Novel Coral-like $\text{Ag}_3\text{C}_6\text{H}_5\text{O}_7$ Microstructures for Surface-enhanced Raman Scattering, *Chemistry Letters*, *45*, 232-34.
- Mills, P., and JL, S. (1983). A study of the core level electrons in iron and its three oxides by means of X-ray photoelectron spectroscopy, *Journal of Physics D: Applied Physics*, *16*, 723.
- Muhler, M., Robert S., and Gerhard, E. (1992). The nature of the iron oxide-based catalyst for dehydrogenation of ethylbenzene to styrene 2. Surface chemistry of the active phase, *Journal of Catalysis*, *138*, 413-44.
- Naveen, M. Halappa, N., Ganesh G., and Yoon-Bo, S. (2017). Applications of conducting polymer composites to electrochemical sensors: A review, *Applied materials today*, *9*, 419-33.
- Nam, K.-W., Yoon, W.-S., and Kim, K.-B. (2002). X-ray absorption spectroscopy studies of nickel oxide thin film electrodes for supercapacitors. *Electrochimica Acta*, *47*(19), 3201-3209.
- Nithya, V., Selvan, R. K., Kalpana, D., Vasylechko, L., and Sanjeeviraja, C. (2013). Synthesis of Bi_2WO_6 nanoparticles and its electrochemical properties in different electrolytes for pseudocapacitor electrodes. *Electrochimica Acta*, *109*, 720-731.
- Okashy, S., Noked, M., Zimrin, T., and Aurbach, D. (2013). The study of activated Carbon/CNT/ MoO_3 electrodes for aqueous pseudo-capacitors. *Journal of The Electrochemical Society*, *160*(9), A1489.
- Padmanathan, N., and S, S. (2014). Mesoporous MnCo_2O_4 spinel oxide nanostructure synthesized by solvothermal technique for supercapacitor, *Ionics*, *20*, 479-87.
- Pang, S. C., Anderson, M. A., and Chapman, T. W. (2000). Novel electrode materials for thin-film ultracapacitors: comparison of electrochemical properties of

- sol-gel-derived and electrodeposited manganese dioxide. *Journal of The Electrochemical Society*, 147(2), 444.
- Pai, R., Arvinder, S., Silas, S., and Vibha, K. (2018). In situ grown iron oxides on carbon nanofibers as freestanding anodes in aqueous supercapacitors, *Advanced Engineering Materials*, 20, 1701116.
- Peng, D., and Rick, T. (2015). EuPaGDT: a web tool tailored to design CRISPR guide RNAs for eukaryotic pathogens, *Microbial genomics*, 1.
- Prasad, K. R., Koga, K., and Miura, N. (2004). Electrochemical deposition of nanostructured indium oxide: high-performance electrode material for redox supercapacitors. *Chemistry of materials*, 16(10), 1845-1847.
- Prasad, K. R., and Miura, N. (2004). Electrochemical synthesis and characterization of nanostructured tin oxide for electrochemical redox supercapacitors. *Electrochemistry communications*, 6(8), 849-852.
- Qu, Q., Yang, S., and Feng, X. (2011). 2d sandwich-like sheets of iron oxide grown on graphene as high energy anode material for supercapacitors. *Advanced materials*, 23(46), 5574-5580.
- Sheets, W. C., Mugnier, E., Barnabé, A., Marks, T. J., and Poeppelmeier, K. R. (2006). Hydrothermal synthesis of delafossite-type oxides. *Chemistry of materials*, 18(1), 7-20.
- Siedliska, K., Pikula, T., Chocyk, D., and Jartych, E. (2017). Synthesis and characterization of AgFeO₂ delafossite with non-stoichiometric silver concentration. *Nukleonika*, 62.
- Singh, A. N., Mondal, R., Rath, C., and Singh, P. (2021). Electrochemical Performance of Delafossite, AgFeO₂: A Pseudo-Capacitive Electrode in Neutral Aqueous Na₂SO₄ Electrolyte. *Journal of The Electrochemical Society*, 168(12).

- Sohrabi, E., Ehsan R., Mohammad H., and Yousef S.-H. (2021). An integrated data analysis of mRNA, miRNA and signaling pathways in pancreatic cancer, *Biochemical Genetics*, 1-33.
- Stern, L.-A., and Xile, H. 2014. Enhanced oxygen evolution activity by NiO_x and Ni(OH)₂ nanoparticles, *Faraday discussions*, 176, 363-79.
- Tang, Y., Xuejin, L., Haiming, L., Dong, X., Wenlong, W., Chunyi, Z. and Hongfei, L. (2020). Stabilized Co³⁺/Co⁴⁺ Redox Pair in In Situ Produced CoSe₂-x-Derived Cobalt Oxides for Alkaline Zn Batteries with 10 000-Cycle Lifespan and 1.9-V Voltage Plateau, *Advanced Energy Materials*, 10, 2000892.
- Temiz, C., Fikret, Y., and UĞUR, K. (2022). Investigation of microstructures and mechanical properties of Sc doped Al-5Cu alloys, (Britannica 2008), *Journal of the Faculty of Engineering and Architecture of Gazi University*, 37.
- Van der Horst, C., Bongiwe, S., Emmanuel, I., and Vernon, S. (2015). Bismuth-silver bimetallic nanosensor application for the voltammetric analysis of dust and soil samples, *Journal of Electroanalytical Chemistry*, 752, 1-11.
- Wang, S.-Y., Ho, K.-C., Kuo, S.-L., and Wu, N.-L. (2005). Investigation on capacitance mechanisms of Fe₃O₄ electrochemical capacitors. *Journal of The Electrochemical Society*, 153(1), A75.
- Wang, Y., Shi, Z., Huang, Y., Ma, Y., Wang, C., Chen, M., and Chen, Y. (2009). Supercapacitor devices based on graphene materials. *The Journal of Physical Chemistry C*, 113(30), 13103-13107.
- Wongpratad, U., Pannawit, T., Jessada, K., Ekaphan, S., and Santi, M. (2020). Effects of nickel and magnesium on electrochemical performances of partial substitution in spinel ferrite, *Journal of Alloys and Compounds*, 831, 154718.
- Wu, M.-S., and Lee, R.-H. (2009). Electrochemical growth of iron oxide thin films with nanorods and nanosheets for capacitors. *Journal of The Electrochemical Society*, 156(9), A737.

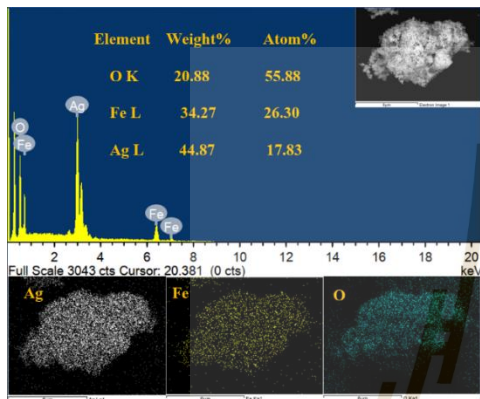
- Wu, X.-L., and Xu, A.-W. (2014). Carbonaceous hydrogels and aerogels for supercapacitors. *Journal of Materials Chemistry A*, 2(14), 4852-4864.
- Yamashita, T., and Peter H. (2008). Analysis of XPS spectra of Fe²⁺ and Fe³⁺ ions in oxide materials, *Applied Surface Science*, 254, 2441-49.
- Yang, X.-h., Wang, Y.-g., Xiong, H.-m., and Xia, Y.-y. (2007). Interfacial synthesis of porous MnO₂ and its application in electrochemical capacitor. *Electrochimica Acta*, 53(2), 752-757.
- Yu, A., Chabot, V., and Zhang, J. (2013). Electrochemical supercapacitors for energy storage and delivery: fundamentals and applications: *Taylor & Francis*.
- Yu, W.-J., Hou, P.-X., Zhang, L.-L., Li, F., Liu, C., and Cheng, H.-M. (2010). Preparation and electrochemical property of Fe₂O₃ nanoparticles-filled carbon nanotubes. *Chemical communications*, 46(45), 8576-8578.
- Zhao, J., Zhang, X., Liu, S., Zhang, W., and Liu, Z. (2013). Effect of Ni substitution on the crystal structure and magnetic properties of BiFeO₃. *Journal of Alloys and Compounds*, 557, 120-123.
- Zhi, M., Xiang, C., Li, J., Li, M., and Wu, N. (2013). Nanostructured carbon-metal oxide composite electrodes for supercapacitors: a review. *Nanoscale*, 5(1), 72-88.
- Zhou, B., Xu Z., Huijuan L., Jiuhui Q., and CP H. (2011). Synthesis of visible-light sensitive M-BiVO₄ (M= Ag, Co, and Ni) for the photocatalytic degradation of organic pollutants, *Separation and Purification Technology*, 77, 275-82.
- Zhu, J., Ping, X., Hailong, L., and Sónia, AC C. (2014). Graphitic carbon nitride: synthesis, properties, and applications in catalysis, *ACS applied materials & interfaces*, 6, 16449-65



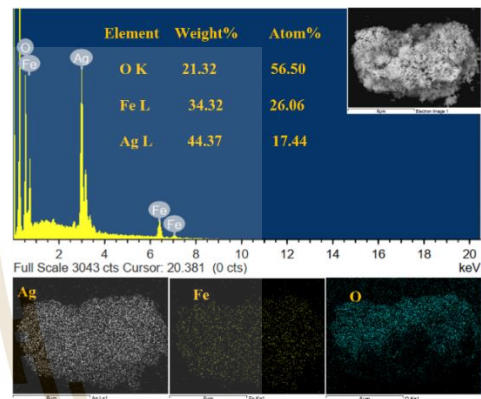
APPENDIX

APPENDIX

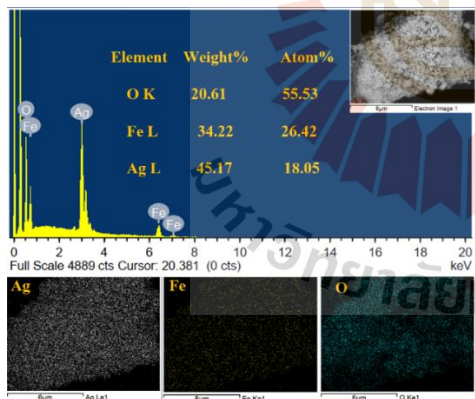
EDS MAPING ANANLYSIS OF EACH CONDITION



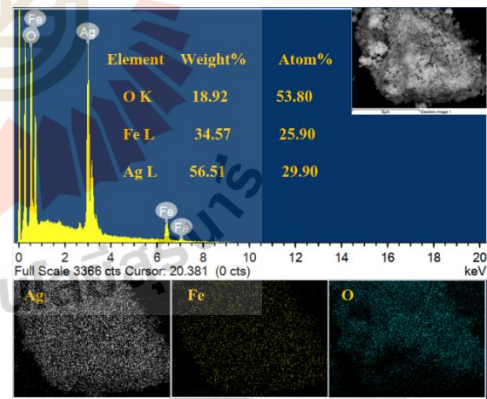
AgFeO₂ sample calcined at 100°C



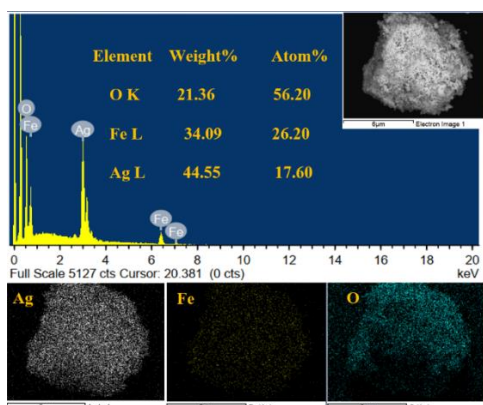
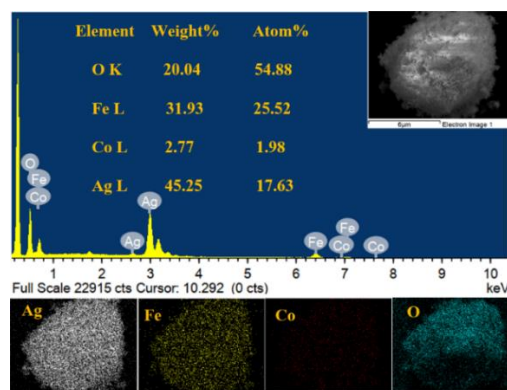
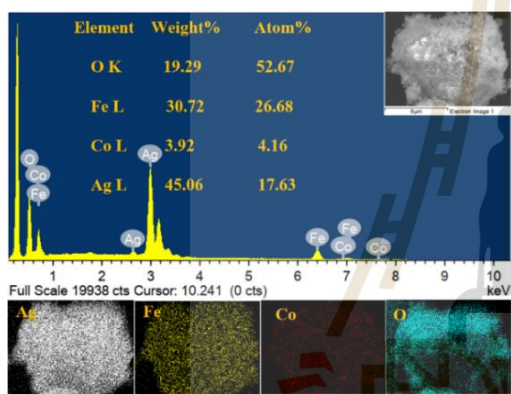
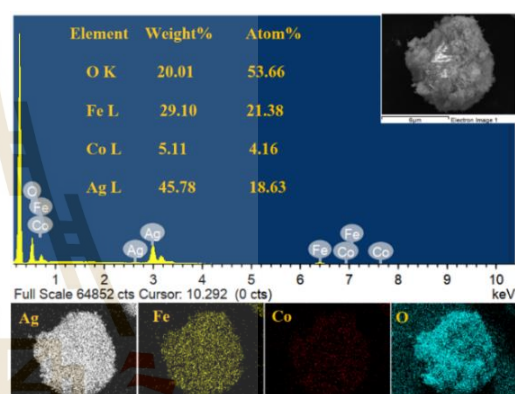
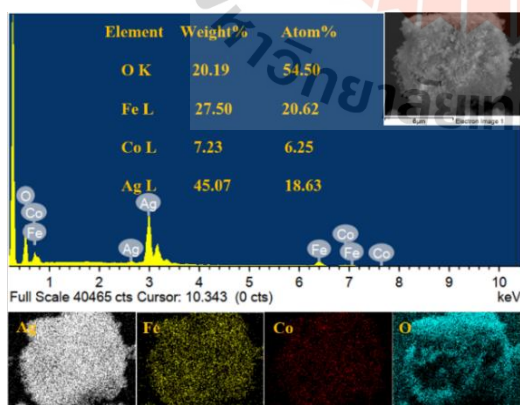
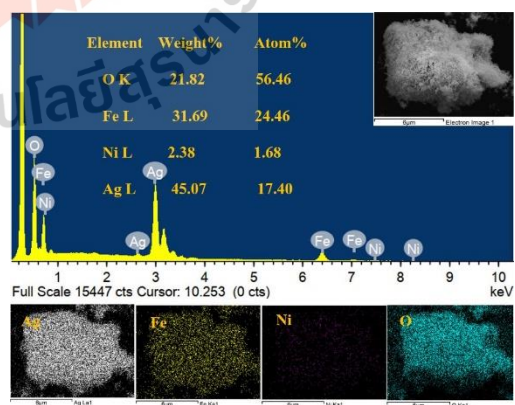
AgFeO₂ sample calcined at 200°C

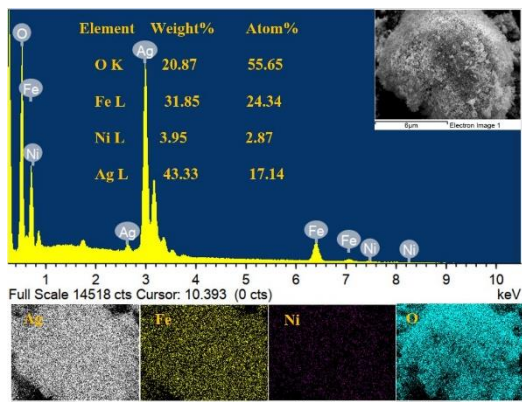


AgFeO₂ sample calcined at 300°C

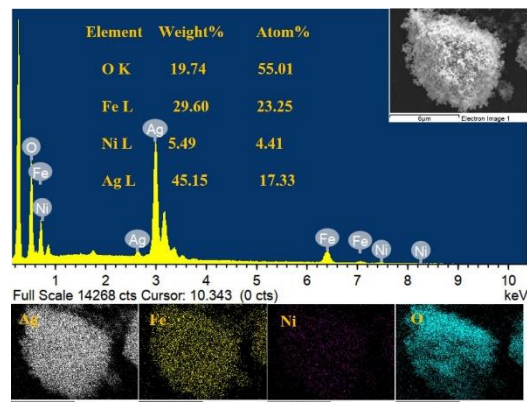


AgFeO₂ sample calcined at 400°C

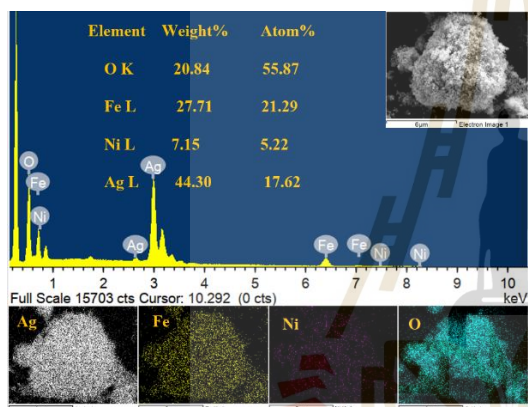
AgFeO₂ sample calcined at 500°CAgFe_{1-x}Co_xO₂ sample with x = 0.05AgFe_{1-x}Co_xO₂ sample with x = 0.10AgFe_{1-x}Co_xO₂ sample with x = 0.15AgFe_{1-x}Co_xO₂ sample with x = 0.20AgFe_{1-x}Ni_xO₂ sample with x = 0.05



$\text{AgFe}_{1-x}\text{Ni}_x\text{O}_2$ sample with $x = 0.10$



$\text{AgFe}_{1-x}\text{Ni}_x\text{O}_2$ sample with $x = 0.15$



$\text{AgFe}_{1-x}\text{Ni}_x\text{O}_2$ sample with $x = 0.20$

CURRICULUM VITAE

Name	Mr. Choulong Veann
Date of Birth	December 17, 1997
Place of Birth	KompongThom, Cambodia
Education	
2017-2021	B.Sc. (Applied Physics), Rajamangala University of Technology Isan, Nakhon Ratchasima, Thailand
2021-present	M.Sc. (Physics), Suranaree University of Technology, Nakhon Ratchasima, Thailand
Scholarship	One Research One Graduate (OROG)

